SENSITIVE AND HIGH-PRECISION ROVIBRATIONAL SPECTROSCOPY OF MOLECULAR IONS RELEVANT TO ASTRONOMICAL AND QUANTUM CHEMISTRY

BY

CHARLES RICHMOND MARKUS

DISSERTATION

Submitted in partial fulfillment of the requirements
for the degree of Doctor of Philosophy in Chemistry
in the Graduate College of the
University of Illinois at Urbana-Champaign, 2019

Urbana, Illinois

Doctoral Committee:

Professor Benjamin J. McCall, Chair
Professor J. Gary Eden
Professor Nick G. Glumac
Assistant Professor Joshua Vura-Weis

Abstract

High-precision spectroscopy of molecular ions has enabled new discoveries in astronomy and provided valuable benchmarks for *ab initio* calculations of molecular structure. Astronomers and theorists require accurate and precise laboratory measurements of rotational and rovibrational transition frequencies, which is particularly challenging for molecular ions. This is because ions are generated in small quantities within laboratory discharges, which are easily obscured by the far more abundant neutral molecules. This dissertation has investigated ways to improve highly sensitive and selective techniques in ion spectroscopy to precisely and accurately determine rovibrational transition frequencies of a number of astronomically and fundamentally important molecular ions.

The sub-Doppler technique Noise Immune Cavity Enhanced Optical Heterodyne Velocity Modulation Spectroscopy (NICE-OHVMS) combines the sensitivity of cavity-enhanced methods with the selectivity of velocity modulation. In this work, a NICE-OHVMS instrument which suffered from parasitic etalons and a sub-optimal mid-infrared (mid-IR) detector was significantly improved by developing methods for reducing the interference fringes and improving the detector performance. The changes enabled measurements which were previously unattainable.

Throughout this work, the NICE-OHVMS instrument was used to investigate three molecular ions: OH^+, H_3^+, and D_2H^+. All three ions are highly relevant to interstellar chemistry and were missing pure rotational transition frequencies that were within the coverage of current observatories. The new rovibrational data were used to predict accurate rotational transition frequencies for all three species, improving the chances of future astronomical detections. Additionally, H_3^+ is the simplest polyatomic molecule, making H_3^+ and D_2H^+ important benchmarks for *ab initio* calculations. By performing an extensive survey of fundamental, hot, and overtone band transitions, highly accurate absolute energy levels of H_3^+ were calculated for the first time.

The final investigation utilized action spectroscopy to study $CH_2NH_2^+$, another astronomically important molecule which lacked any rotationally resolved spectroscopic data. This was performed using the action spectroscopy technique Laser-Induced Inhibition of Complex Growth (LIICG), where vibrational excitation prevented helium from attaching to the ions which were collisionally cooled to cryogenic temperatures ($\sim$ 10 K) in multipole ion trap. Measurements of rovibrational transitions were used to predict pure rotational transition frequencies, which were then measured with the first demonstration of millimeter-wave / mid-infrared double resonance using LIICG.

To Mom, Dad, Jayme, and Victor

Acknowledgments

This work would not have been possible without the help, support, and inspiration from family, friends, colleagues, and mentors. First, I would like to thank my advisor, Professor Benjamin McCall. He was always available to lend his knowledge and guidance throughout my degree. He encouraged me to apply for competitive fellowships, attend conferences around the world, mentor undergraduates, and trusted me to pursue my research as I saw fit.

I would also like to thank my dissertation committee, Professors Gary Eden, Joshua Vura-Weis, and Nick Glumac, for their mentorship and support. Professor Eden was always generous with his extensive knowledge of plasma electronics, which helped me through a number of challenges. I would like to thank Professor Vura-Weis for being a resource for career advice and for inviting me to join in his group meeting discussions.

I would like to thank Professor Stephan Schlemmer and Dr. Oskar Asvany for inviting me to come and work with their ion trap experiments in Cologne, Germany. This incredible opportunity gave me access to new experimental techniques and proved to be a fruitful and educational exchange. Professor Schlemmer's enthusiasm for tackling challenging scientific problems was a great inspiration when I needed it most in the final months of my PhD.

I also thank my labmates, James Hodges and Adam Perry, who brought me into their experiment and taught "Charlie Elbows" how to align a cavity, work with an optical frequency comb, and write acquisition software. Even when I was a relatively new graduate student, they still supported me and my own research endeavors by willingly staying late to help run the instrument. I would also like to thank the rest of the graduate students in the McCall group, and I will look back fondly at the times spent at the restaurant Cravings and the White Horse Inn.

I have had the opportunity and privilege to mentor a number of undergraduate students. I would like to thank Thomas Persinger for enthusiastically pursuing a double resonance side project, Thomas Dieter who helped develop an undergraduate project investigating methane, and Philip Kocheril who stepped up to every challenge I gave him, including writing his own peer reviewed publication.

I would like my classmates, who kept me sane with Journal Club, game nights, and movie nights. In particular, Sage Dunham and Amit Patel have consistently been there as friends since our graduate school visit. Without them, graduate school would have certainly been a lonelier experience.

I want to thank my closest friends and family who are not part of the academic community–even when I missed

weddings, family reunions, birthdays, and many more events due to conferences and deadlines, they were always supportive.

Last, I would like the NASA Earth and Space Science Fellowship, which provided financial support for three years. This gave me the freedom to attend conferences and work with collaborators, which greatly enriched my graduate school experience.

Table of Contents

List of Tables

List of Figures

List of Abbreviations

ISM	Interstellar medium
VMS	Velocity Modulation Spectroscopy
CE-VMS	Cavity-Enhanced Velocity Modulation Spectroscopy
NICE-OHMS	Noise-Immune Cavity-Enhanced Optical Heterodyne Molecular Spectroscopy
NICE-OHVMS	Noise Immune Cavity Enhanced Optical Heterodyne Velocity Modulation Spectroscopy Modulation Spectroscopy.
FM	Frequency modulation.
OFC	Optical Frequency Comb
EOM	Electro-optic modulator
AOM	Acousto-optic modulator
OPO	Optical Parametric Oscillator
LIICG	Laser-induced inhibition of complex growth

Chapter 1

Introduction

Molecular ions play an important role in the dynamics and chemistry of low temperature plasmas, which include environments as diverse as interstellar molecular clouds [1, 2], planetary ionospheres [3], and laboratory discharges [4]. In the interstellar medium (ISM), reactions between ions and neutrals are able to overcome the cold and diffuse conditions to drive exotic and rich chemistry which is not found on Earth. Infrared and radio observatories are able to observe and identify molecules through their rotational and rovibrational transitions, which requires precise and accurate laboratory data. Molecular ions are also important to quantum chemistry. Many fundamental chemical systems are molecular ions, and their rovibrational energy levels can be used to probe physical phenomena such as the breakdown of the Born–Oppenheimer approximation [5] or the electron-electric dipole moment [6]. Theorists require highly accurate laboratory measurements to act as benchmarks as their methods become competitive with past experimental values.

Progress in determining accurate rovibrational transition frequencies of molecular ions has lagged behind that of neutral molecules, due to the challenges associated with measuring the spectra of gas phase ions. Laboratory discharges can only produce ions in relatively dilute quantities, and in many cases they can be obscured by the much more abundant neutral molecules. Therefore, milestones in molecular ion spectroscopy have come as new methods have overcome these challenges.

1.1 Astrochemistry

Astrochemistry began in the late 1930s, when a few unidentified sharp electronic transitions were observed by spectrographs at Mount Wilson observatory [7], which were later assigned to be the diatomic molecules CH, CN, and CH^+ [8, 9, 10] . This proved that molecules could persist in the harsh environment of interstellar space, despite the presence of destructive ultraviolet (UV) light. Detections of additional molecules would not occur for nearly three decades, when the development of radio astronomy and microwave spectroscopy allowed for molecules to be detected by their rotational emission at sub-mm and radio frequencies [11]. If a molecule possesses a permanent dipole moment, it will have rotational transitions which will absorb and emit electromagnetic radiation at specific frequencies

as determined by its structure. Since 1970, a steady progression of ∼4 molecules per year have been discovered in circumstellar and interstellar space, with nearly 200 molecules detected in total [12].

Early on, it was evident that molecules were valuable as probes of their local environment—the relative populations of a molecule's rotational states provided information on the local radiation field and collisional environment, and their Doppler profiles allowed for measuring the dynamics of molecular clouds [13]. However, their lacked any rigorous gas-phase chemical model that could explain their abundances, and astronomers were left with the unsatisfying explanation that they form on the surface of dust grains. It was not until 1973 when two seminal papers proposed that bimolecular reactions between ions and neutrals could explain the high abundances that were observed [14, 15]. Classically, a reaction between an ion and a polarizable molecule will occur at the Langevin capture rate constant [16],

$$k_L = 2\pi e \sqrt{\frac{\alpha}{\mu}} \tag{1.1}$$

where α is the dipole polarizability of the neutral partner and μ is their reduced mass. This temperature-independent expression leads to reaction rates of $\sim 10^{-9}$ cm^3 s^{-1}, which is several orders of magnitude faster than reactions between neutral molecules at low temperatures and fast enough to be relevant under interstellar conditions on cosmic timescales.

Hydrogen is the most abundant element in the universe, and it should come at no surprise that it plays a central role in the chemistry of interstellar space. In a dense molecular cloud, it takes on average ∼3 billion years for a hydrogen molecule to be ionized to H_2^+ by a cosmic ray, but then it only takes a few months for it to react with H_2 to form H_3^+ [17]. Then, $H_3{}^+$ can initiate chains of ion-neutral reactions, one of which leads to the formation of water in dense molecular clouds [18]:

$$H_3{}^+ + O \rightarrow OH^+ + H_2 \tag{1.2}$$

$$OH^+ + H_2 \rightarrow H_2O^+ + H \tag{1.3}$$

$$H_2O^+ + H_2 \rightarrow H_3O^+ + H \tag{1.4}$$

$$H_3O^+ + e^- \rightarrow H_2O + H; \quad H_3O^+ + e^- \rightarrow OH + H \tag{1.5}$$

By considering the competing processes, the relative abundances of H_nO^+ species or the abundance $H_3{}^+$ can provide further information about their local environments, such as the cosmic ray ionization rate, molecular hydrogen fraction, and density of free electrons [19, 20]. In general, molecular ions drive the chemistry of the interstellar medium (ISM), and are valuable probes of local environments. Therefore they are particularly valuable targets for astronomers.

Identifying a molecule in the interstellar medium by its rotational transitions requires highly accurate rest frequencies, which should come from laboratory measurements. A "firm" detection towards an object within a crowded spectra, such as the one shown in Fig. 1.1 towards the Orion KL nebula [21], requires the rest frequencies to be

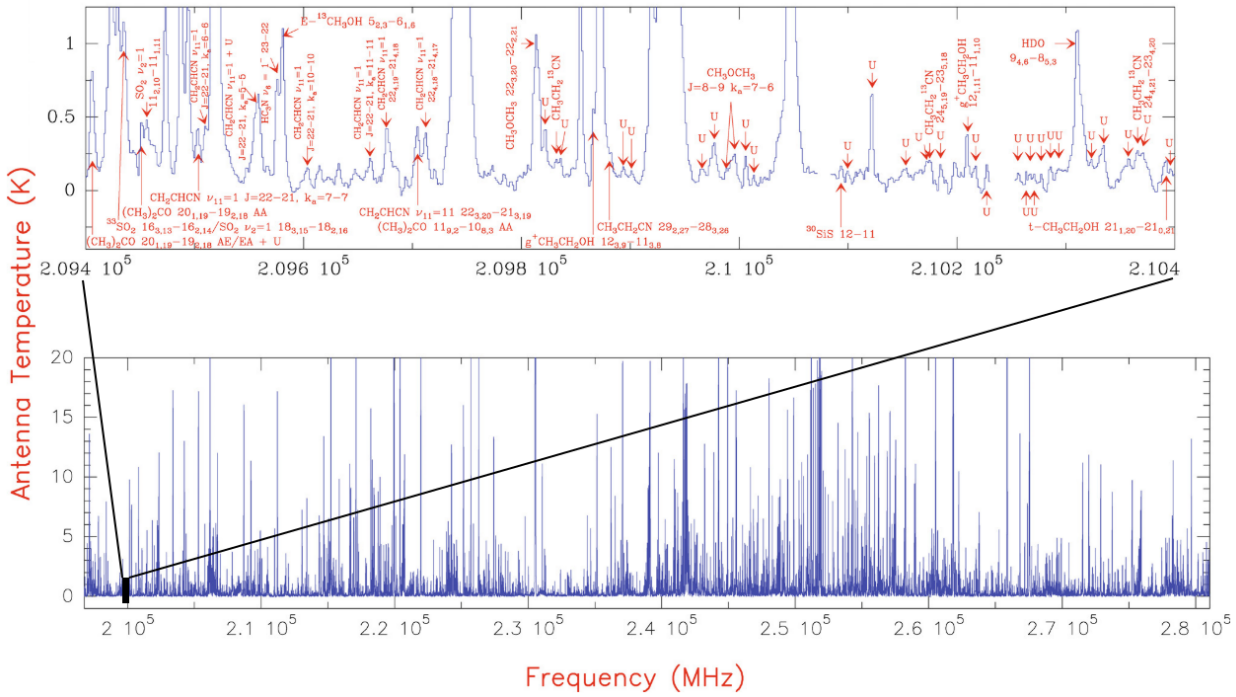

Figure 1.1: A spectral line survey towards the Orion KL nebula obtained by the 30 m IRAM radio telescope [21]. The bottom trace shows the region from 200–280 GHz, and the top trace shows the spectral density over the small section from 209.4–210.4 GHz. Unassigned transitions are marked with "U". Note that antenna temperature (K) is a unit of power per unit frequency.

known to within 1 part in 10^7 (20 kHz at 200 GHz) [22]. In colder environments with less crowded spectra, knowing a transition frequency to within $\sim$ 1 MHz is often sufficient for a detection. There are still many important molecular ions which lack accurate rotational data, and one of the main objectives of this work was to determine the rotational transition frequencies of astrochemically relevant ions that are within the coverage of current observatories. This was accomplished for OH^+, D_2H^+, $H_3{}^+$, and $CH_2NH_2{}^+$ which is described in Chapters 3, 4, 5, and 6.

1.2 Quantum chemistry

Quantum chemistry seeks to understand the structure and dynamics of molecules through quantum mechanics. The highly successful Born–Oppenheimer (BO) approximation laid the foundation for this work, which makes the assumption that the fast moving electrons can be treated as if the slow moving nuclei were fixed in space [23]. This "clamped nuclei" approximation has successfully married quantum mechanics and chemistry, allowing for quantitative understanding of important concepts such as potential energy surfaces (PES's), transition state theory, and molecular orbital theory [24]. High resolution spectroscopy is capable of measuring the differences between rovibrational energy levels, which are directly linked to a molecule's PES. Therefore, spectroscopy has been a useful tool for assessing the quality

of PES's.

Calculating rovibrational transitions to within "spectroscopic accuracy" (< 1 cm^{-1}) is only possible for a handful of fundamental systems, which have to take into account the breakdown of the BO approximation [25]. The largest deviation is often due to the BO approximation treating the nuclei as having infinite mass when determining the PES. To a first-order approximation, a correction surface can be calculated which treats the nuclei as having finite mass while maintaining separation of nuclear and electronic time scales [26]. These are diagonal corrections to the adiabatic BO PES, and therefore the effect is called "adiabatic" coupling. The off-diagonal coupling is referred to as "non-adiabatic", which is much more challenging to account for computationally. This interaction between electronic and nuclear motion is responsible for conic intersections of electronic states in larger polyatomic molecules, which is behind many important processes in molecular electronics [27, 28]. Small molecules offer simpler systems to investigate nonadiabatic effects, which often manifest as an increase in the effective nuclear masses due to "electron dragging"[29].

In addition to coupling between electronic and nuclear motion, contributions from relativistic and quantum electrodynamic effects (QED) must be included. Both of these effects can be treated through non-relativistic QED [30] using perturbation theory with an expansion in terms of the fine-structure constant, α. Usually, only second order (α^2) relativistic corrections are included, which account for the velocity-dependence of the electron's mass, and treating the electron as a volume instead of a point charge [31]. QED corrections are on the order of α^3 and higher, which account for "radiative" effects, such as quantum vacuum fluctuations [32] .

Only a handful of molecules can have all of these effects computed *ab initio*, making these systems important benchmarks for new computational methods. When all of the post-BO effects are taken into account with higher order QED effects, as is the case for H_2^+ [33] and H_2 [34], calculations have achieved extraordinary agreement with experiment to within 10^{-5} and 2×10^{-4} cm^{-1} respectively. In the case of HeH^+, only QED effects at the α^3 order have been calculated, reaching agreement of 0.01 cm^{-1}[31]. For the simplest polyatomic molecule, $H_3{}^+$, it become much more difficult to handle corrections for nonadiabatic coupling directly through perturbation theory, and so far only approximate method have been used [29]. Purely *ab initio* methods achieve agreement on the order of 0.1 cm^{-1}(3 GHz) [35]. Strategies which include coordinate-dependent masses with a small amount of experimental input can reach agreement of 0.001 cm^{-1}[29], which is more accurate than most of the previously available experimental data [36]. Therefore, new accurate and precise spectroscopic measurements were needed to act as benchmarks to assess the behavior of current and future *ab initio* calculations of $H_3{}^+$, which was another objective of this work.

1.3 Spectroscopy of molecular ions

Determining rotational transitions and measuring relative energy levels within a vibrational state can be done directly using rotational spectroscopy if the molecule possesses a permanent dipole moment. However, for light molecules such as OH^+ and D_2H^+, the spacing between transitions becomes quite large. Sources for sub-mm and THz spectroscopy often have limited coverage, and measuring a complete spectrum could requires a number of configurations and a substantial amount of time. Additionally, the Doppler broadening is quite small (< 1 MHz), and scans must be taken with small step sizes to ensure a transition is not missed, making searches quite tedious. However, the small Doppler broadening does allow for extremely high precision and resolution. The search problem can be avoided by indirectly measuring the rotational structure using rovibrational spectroscopy in the mid-infrared (mid-IR), where tunable light sources and detectors with wide coverage are available.

Polyatomic molecules have $3N - 6$ degrees of vibrational freedom ($3N - 5$ for linear molecules), and if motion along a vibrational coordinate causes a change in the dipole moment it will be infrared active. Allowed transitions will follow the selection rules $\Delta v = \pm 1$ and $\Delta J = \pm 1$ and 0, where v and J are the vibrational and total angular momentum quantum numbers respectively. Therefore, when the absorption of a particular vibrational band is measured with high resolution, it will be composed of rotational structure. This structure contains information on the rotational energy levels of the two vibrational states, which can be used to predict rotational transitions and calculate relative energy levels, either directly through combination differences (CDs) or by fitting the transitions to an effective Hamiltonian. However, Doppler broadening becomes significant (< 300 MHz) at mid-IR frequencies, which limits the precision and resolution.

There are also a number of challenges associated with measuring absorption signals from molecular ions. Ions are generated in small abundances ($< 10^{10}$ cm^{-3}) in laboratory plasmas, and are far less abundant than neutral species. Therefore, the absorption signals are small and can easily be obscured by signals from neutral molecules. It is desirable to use methods which are highly sensitive and that are able to discriminate between signals from ionic and neutral species.

1.3.1 Velocity modulation spectroscopy

The workhorse for high resolution spectroscopy of molecular ions has been Velocity Modulation Spectroscopy (VMS), which is capable of selectively measuring signals from ions [37]. A typical VMS layout is shown in Fig. 1.2 a. When ions are generated in an AC discharge at audio frequencies, the average velocity of the ions will oscillate as they follow the cathode. This causes the Doppler profile of the ions to modulate at the frequency driving the plasma. A phase-sensitive detector can be used to recover the modulated signals from charged species while ignoring absorption

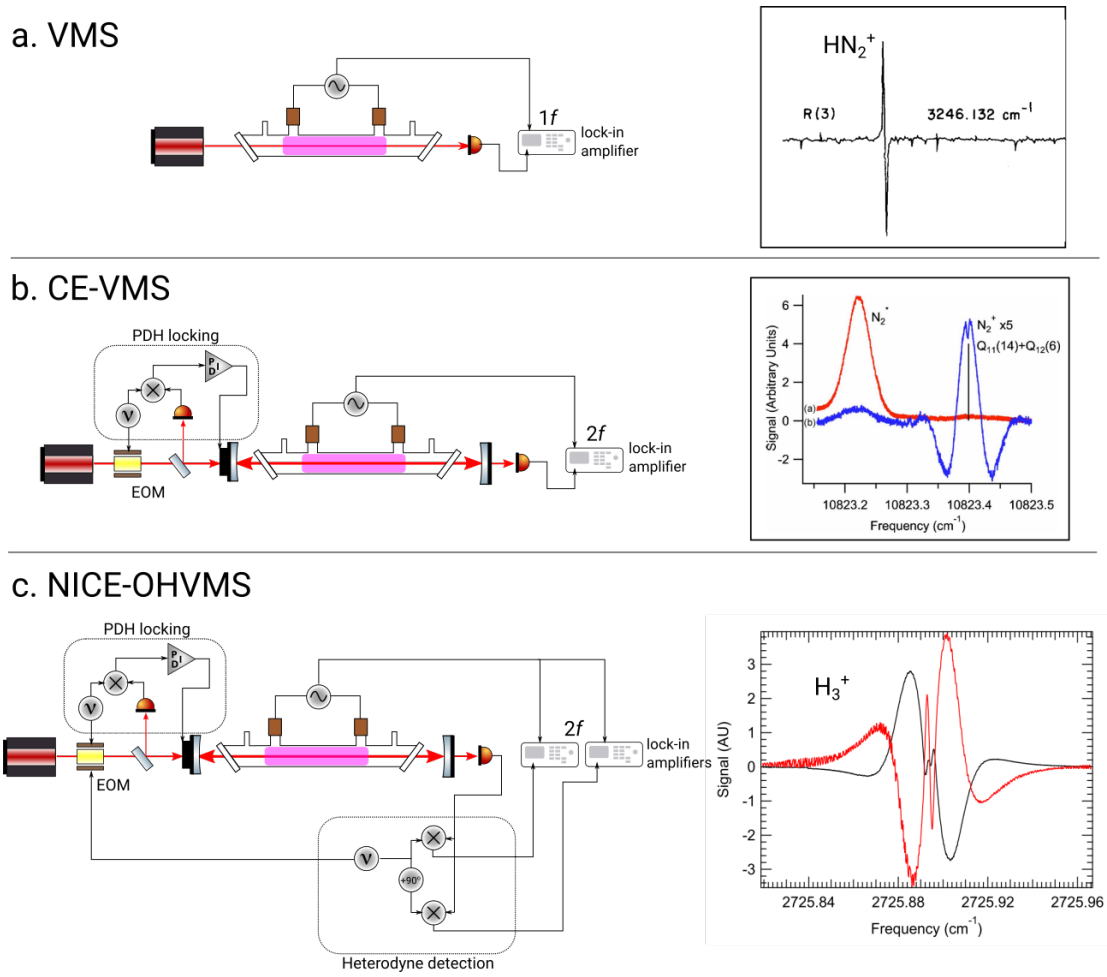

Figure 1.2: The progression of velocity modulation techniques, with their prototypical configuration and measurement from their first appearance in the literature. a. VMS: Velocity Modulation Spectroscopy [37], b. CE-VMS: Cavity-Enhanced Velocity Modulation Spectroscopy [38], c. NICE-OHVMS: Noise Immune Cavity Enhanced Optical Heterodyne Velocity Modulation Spectroscopy [39]. EOM: Electroptic Modulator, PDH: Pound-Drever-Hall.

from neutral species. This method has some limitations as far as performing precision measurements. The transitions are still Doppler broadened, and for light molecules such as H_3^+ this can lead to widths on the order of 350 MHz at room temperature. This makes determination of the rest frequencies to within microwave accuracy of ~1 MHz quite challenging.

1.3.2 Sub-Doppler spectroscopy

Broadening mechanisms for molecular absorption can either be homogeneous where the probability of absorption is the same for all molecules, such as the pressure and lifetime broadening, or inhomogeneous where the environment or conditions of a given molecule change the frequency at which it absorbs, such as Doppler broadening. The line shape will be a convolution of the two types of broadening, and the homogeneous broadening is usually much smaller if the

pressure is sufficiently low.

Lamb dip spectroscopy is able to overcome the inhomogeneous Doppler broadening by generating a sub-Doppler feature that is centered at the "rest frequency" (f_0) of a transition. Molecules traveling at velocity v will absorb light shifted by $f_0(v/c)$ from f_0, where c is the speed of light. If the laser has sufficient power, a significant population of molecules with velocity v will be shifted to the excited state. Since absorption is proportional to the difference in population of the two states, this will increase the transparency at this particular velocity component, which is known as "saturation". If the laser is reflected back through the sample, the reflected beam will be resonant with molecules traveling at velocity $-v$. When both beams are resonant with the same velocity component, which only occurs at the rest frequency for $v = 0$, each beam will probe the change caused by the other resulting in a Lamb dip which will be centered on f_0. This method drastically improves the resolution of infrared techniques, and allows for rest frequencies to be determined with much higher precision.

Cavity-Enhanced Velocity Modulation Spectroscopy

Sub-Doppler spectroscopy is more challenging for ions than it is for neutral molecules. Ions have much larger collisional cross sections, leading to increased pressure broadening and a larger homogeneous linewidth. Since collisions cause vibrational relaxation, it also increases the optical intensity required to saturate a transition. Placing the sample within an optical cavity helps overcome some of these issues. Symmetric cavities provide a significant power enhancement which improves saturation, and have counter propagating beams in order to generate Lamb dips. Additionally, the light will make multiple passes through the sample resulting in an increase in effective path length, and therefore sensitivity. However, there are still challenges when implementing this with a VMS experiment. Because the light is traveling in both directions, the shift caused by the ions traveling towards the cathode will be opposite for the counter propagating beams. The VMS signal can still be recovered with $2f$ detection. This scheme is called Cavity-Enhanced VMS (CE-VMS) [38], and a typical layout is shown in Fig. 1.2 b. This technique has been demonstrated to saturate transitions of molecular ions, however the ion-neutral discrimination is hindered since concentration modulation of neutral molecules also occurs in the $2f$ detection channel. Signals from ions and neutrals occur at different phases and have different spectral lineshapes. For example, Fig. 1.2 b. shows a scan which covers electronic transitions of N_2^* and N_2^+, where the red and blue traces represent two different detection angles. The VMS and concentration modulation signals can be isolated by setting the lock-in phase, and the transitions have significantly different lineshapes.

Noise Immune Cavity Enhanced Optical Heterodyne Velocity Modulation Spectroscopy

Although CE-VMS was capable of sub-Doppler spectroscopy, its sensitivity was limited. The technique requires locking the laser to the cavity, which is accomplished using a Pound-Drever-Hall (PDH) locking scheme [40] with

corrections sent to the laser frequency or to a piezoelectric transducer (PZT) to control the cavity length. Placing a discharge within the cavity generates a large amount of lock noise, which ultimately comes through as intensity noise

This led to the natural marriage of CE-VMS and Noise-Immune Cavity-Enhanced Optical Heterodyne Molecular Spectroscopy (NICE-OHMS) which significantly suppresses lock noise [41]. NICE-OHMS combines cavity enhancement with heterodyne detection, where the laser is phase modulated to generate sidebands which are separated from the carrier by the heterodyne modulation frequency, which is called a frequency modulation (FM) triplet. Each sideband generates a beat signal with the carrier at the heterodyne frequency, which does not result in an intensity modulation when the FM triplet is "balanced", *i.e.*, the sidebands have equal intensity. If one the sidebands is diminished due to a molecular absorption, the beat signal from the other sideband and the carrier will cause an intensity modulation at the heterodyne modulation frequency which can converted to direct current (DC) signal with a radio frequency (RF) mixer. Heterodyne detection is effective at reducing technical noise by encoding the signal in the RF, which is a relatively quiet region.

To perform heterodyne detection with cavity enhancement, the entire FM triplet must be coupled into the cavity by matching the modulation frequency to an integer multiple of the free spectral range (FSR) of the cavity. If the FM triplet comes slightly off resonance with cavity, each component of the FM triplet samples the same part of a longitudinal cavity modes, and there is no net signal. This provides "noise immunity" and greatly improves techniques which suffer from lock noise such as CE-VMS. The combined technique is known as Noise Immune Cavity Enhanced Optical Heterodyne Velocity Modulation Spectroscopy (NICE-OHVMS) [39]. A typical NICE-OHVMS layout and a scan of a transition in the ν_2 fundamental band of $H_3{}^+$ is shown in Fig. 1.2 c.

The improvement in sensitivity enabled measurements of H_3^+, HeH^+, and OH^+ [42, 43, 44, 45]. However, new issues appeared. Alignment to a symmetric cavity has the input beam directly normal to the surface of the first mirror, reflecting light back towards the source. This will inevitably lead to optical interference, known as parasitic etalons, caused by reflections between various optical elements in the path. Interference fringes can be clearly seen in the detection channel shown in red in Fig. 1.2 c. These are often the plague of sensitive spectroscopic methods, and can be difficult to remove. The sensitivity of the original configuration of NICE-OHVMS in the mid-infrared was limited by these interference fringes, which prevented measurements of transitions from rotational and vibrationally excited H_3^+, and from measuring ions where the chemistry was less favorable. Therefore, significant efforts were made to improve the sensitivity of NICE-OHVMS. This included exploring ways to reduce the parasitic etalons and alternative detection schemes, which is the focus of Chapter 2.

In this work, NICE-OHVMS was used to investigate the rovibrational spectra of light molecules relevant to astronomy and quantum chemistry, which included OH^+, D_2H^+, and $H_3{}^+$, which are described in Chapters 3, 4, and 5 respectively. Many of these measurements were made possible by the improvements described in Chapter 2.

1.3.3 Optical frequency comb assisted spectroscopy

Sub-Doppler spectroscopy allows for highly precise measurements, but the accuracy will still be limited by the frequency calibration. In the past, frequency calibration for mid-IR spectroscopy was accomplished using reference gases as a frequency standard and an etalon to provide an additional frequency ruler. With such efforts, the uncertainties were estimated to be on the order of 90–150 MHz. Since then, the relatively new technology of Optical Frequency Combs (OFCs) has caused a revolution in the metrology community [46]. OFCs are mode-locked lasers, where each pulse has a defined phase relationship with the previous pulse. In frequency space, this will appear as a series of delta functions, called "comb teeth", which are separated by the repetition rate of the laser and offset by the carrier-envelope offset (CEO). The offset and the repetition rate can be locked to an RF frequency standard, such as an atomic clock, and the frequency of each comb tooth can be determined with extraordinary accuracy.

An OFC can act as the ultimate frequency ruler. When a laser is colinearized with the comb, it will generate a beat note with the nearest comb tooth. With this information, and the knowledge of each comb tooth's exact position, an OFC can be used to determine the frequency of a CW laser with high precision and accuracy. Performing OFC assisted spectroscopy with an optical parametric oscillator (OPO) as the mid-IR source provided the frequency calibration for the NICE-OHVMS measurements.

1.3.4 Ion trap action spectroscopy

Another approach to ion spectroscopy is to perform action spectroscopy, where a change in the chemical system is measured as a function of frequency, as opposed to direct absorption experiments which measure the change in the intensity of light. Ions are particularly suited for this. They can be controlled using ion-optics, which allows for mass selecting a target ion and holding it within an ion trap for extended periods of time. The light can be sent through the trap, and any changes to the sample due to absorption can be observed by mass filtering the contents and counting the ions.

The "COLTRAP" instrument, built by Professor Schlemmer's group at the University of Cologne, was designed for performing action spectroscopy on ions cooled to cryogenic temperatures ($\sim$ 10 K) [47]. Reaching such a low kinetic temperature allows for Laser-Induced Inhibition of Cluster Growth (LIICG) spectroscopy. Helium has a binding energy of < 1 kJ mol^{-1} (≈ 83.6 cm^{-1}), and will bind to most ions through a ternary collision process at these temperatures. However, if an ion is vibrationally or rotationally excited, the helium will be less likely to become attached. Therefore, if the laser is on resonance with a rovibrational transition, the number of clusters formed will be reduced, as shown for $CH_2NH_2^+$ in Fig. 1.3. The low translational temperatures lead to narrow Doppler widths on the order of 50 MHz, which is sufficient for high precision measurements. Because LIICG measures the prevention of a cluster formation and not the dissociation of tagged ions, the transition frequencies are unperturbed by tagging.

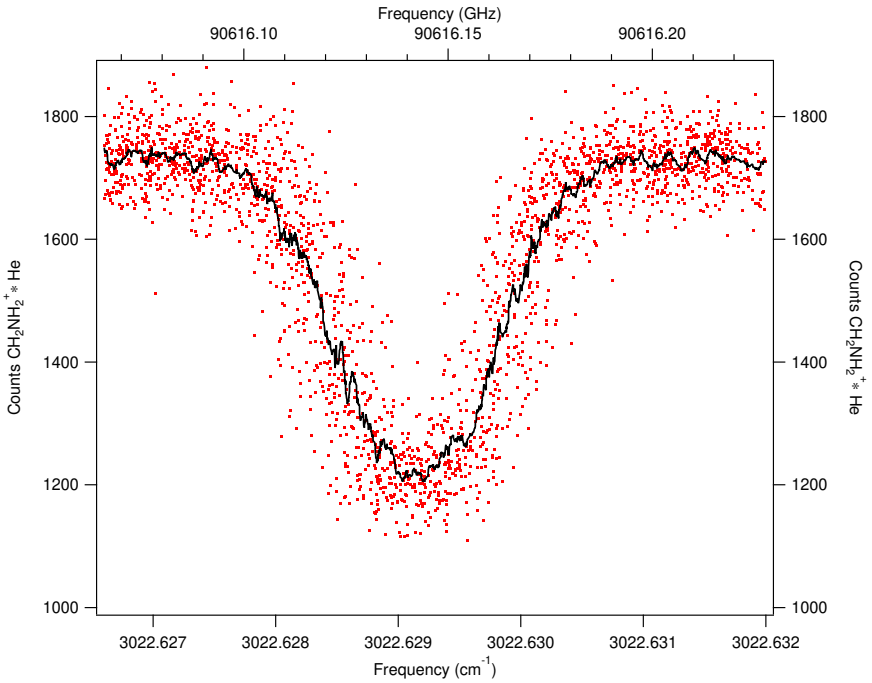

Figure 1.3: An example of an LIICG scan of a rovibrational transition in the ν_4 fundamental band of $CH_2NH_2^+$. The raw data points are shown in red, and the boxcar averaged scan is shown in black. The Doppler width of the transition is 43 MHz, which gives a kinetic temperature of 13 K.

LIICG is versatile, in that it is straight forward to employ different light sources. For example, sub-millimeter (sub-mm) sources can be used to cause rotational excitation, which does have a small effect on the helium attachment efficiency. A more powerful technique is to use a sub-mm and a mid-IR source simultaneously to perform double resonance. In this scheme, the upper state of the rotational transition is the initial state of a rovibrational transition. Then, the mid-IR light source is held at the rovibrational transition frequency while the sub-mm source is scanned. If the sub-mm is resonant with a transition, it will increase the number of ions that can absorb the mid-IR light causing an increase in signal, which had never been demonstrated with LIICG. The final investigation for this work was to implement double resonance with LIICG to measure rotational transitions of astronomicaly important ions.

The COLTRAP instrument is complementary with the NICE-OHVMS technique. Because the ions have much lower internal temperatures within the ion trap, transitions from heavier or fluxional ions are much stronger. However, NICE-OHVMS is better suited for measuring higher rotational and vibrational states of light molecules such as H_3^+ and OH^+. For this reason, COLTRAP was used to perform rovibrational and rotational measurements of $CH_2NH_2^+$, as described in Chapter 6.

Chapter 2

Improving cavity-enhanced spectroscopy of molecular ions in the mid-infrared

2.1 Introduction

Accurate and precise measurements of rovibrational transitions of molecular ions have led to discoveries of important processes in the interstellar medium and have provided valuable benchmarks for cutting-edge potential energy surfaces from *ab initio* theory [1, 48]. In the past five years, new laboratory techniques have been developed that can determine rovibrational transitions of molecular ions with sub-MHz precision [42, 49, 50]. One such technique is Noise Immune Cavity Enhanced Optical Heterodyne Velocity Modulation Spectroscopy (NICE-OHVMS), which combines the sensitivity of Noise-Immune Cavity-Enhanced Optical Heterodyne Molecular Spectroscopy (NICE-OHMS) [41] with the ion-neutral discrimination of velocity modulation spectroscopy (VMS) [37].

Instead of directly measuring absorption, NICE-OHMS measures the difference in absorption and dispersion at the different components of a frequency modulation (FM) triplet, which is composed of a central carrier and two sidebands spaced by the modulation frequency. If the modulation frequency is set to an integer multiple of a cavity's free spectral range (FSR), the entire triplet can be resonantly coupled into the cavity yielding a significant boost in signal. An additional benefit is the "noise immunity", which is the ability to reduce noise from a poor laser-to-cavity lock—if the laser is slightly off resonance, all three components of the FM triplet are affected identically By adding VMS detection, we can discriminate signals from ions and neutrals while gaining an additional layer of modulation. Within an AC discharge, ions will follow the electric field which results in an oscillating Doppler profile, and the modulated signal can be recovered by a lock-in amplifier.

With NICE-OHVMS, we have successfully measured a number of transitions of H_3^+, HeH^+, and OH^+ with the highest precision to date [42, 43, 44, 45]. However, insufficient signal-to-noise (S/N) of many transitions has limited the extent of these studies, and only the frequencies of the strongest transitions within the fundamental bands were determined with sub-MHz precision. could be observed at all, not just sub-MHz lines The insufficient S/N can be

This chapter is adapted with permission from C. R. Markus, A. J. Perry, J. N. Hodges, and Benjamin J. McCall, Optics Express **25**, 3709 (2017), Copyright 2017, The Optical Society.

attributed to the lack of sensitive detectors in the mid-infrared (mid-IR) and the presence of parasitic etalons.

Mid-IR transitions are far from the coverage of detectors with the best noise characteristics in the near-IR and visible. Although many overtone transitions are in the near-IR, corresponding transitions within fundamental bands in the mid-IR are at least an order of magnitude stronger. Up-conversion detection is capable of overcoming this limitation by enabling the measurement of mid-IR transitions with near-IR and visible detectors using difference or sum frequency generation (DFG or SFG). The mid-IR light is converted to wavelengths within the coverage of silicon detectors while maintaining the frequency and velocity modulation signals. Up-conversion has enabled mid-IR single-photon counting experiments, sensitive THz detection at room temperature, and has improved wireless communication with quantum cascade lasers [51, 52, 53]. In this work, up-conversion through DFG has been implemented into the NICE-OHVMS technique, which has enabled the use of a faster and more sensitive silicon detector. However, the benefits from up-conversion could not be realized until periodic signals from etalons were removed from the background.

Parasitic etalons have long plagued sensitive spectroscopic techniques. The interference from light reflecting between parallel surfaces can easily obscure weak signals. Other frequency modulation spectroscopy (FMS) techniques have fought this by separating optics at etalon-immune distances [54, 55]. The strength of the fringes from an etalon in an FMS experiment is different for absorption and dispersion and depends on the ratio between modulation frequency (ν_m) and the FSR of the etalon. Fringes appearing in dispersion and have a $\sin(2\pi\nu_m/\mathrm{FSR})$ dependence, whereas those in absorption take the form of $\sin^2(2\pi\nu_m/\mathrm{FSR})$ [54]. Etalon immune distances work by setting the modulation frequency to be an integer multiple of the FSR of the etalon, which removes the signal in absorption and dispersion. However, experimental constraints can necessitate low modulation frequencies making the etalon-immune distance impractically long. Another solution is to rapidly change the positions of the interference fringes and average them out [56]. In the past, this has been avoided by NICE-OHMS and other cavity enhanced techniques because it was thought that it could disrupt the lock to the cavity. We have found that a rapidly rotated CaF_2 window set in our optical path is capable of removing fringes from NICE-OHVMS scans without introducing other forms of noise. This has eliminated the signals from parasitic etalons in our instrument.

2.2 Experimental

A block diagram of the instrument is shown in Figure 2.1. The technique builds upon the NICE-OHVMS instrument which has been described in previous publications [39, 42]. In brief, 1064 nm light from a ytterbium-doped fiber laser is first sent to a fiber-coupled acousto-optic modulator (AOM) for frequency corrections and then phase modulated by a fiber-coupled electro-optic modulator (EOM) to produce two sets of sidebands for Pound-Drever-Hall (PDH)

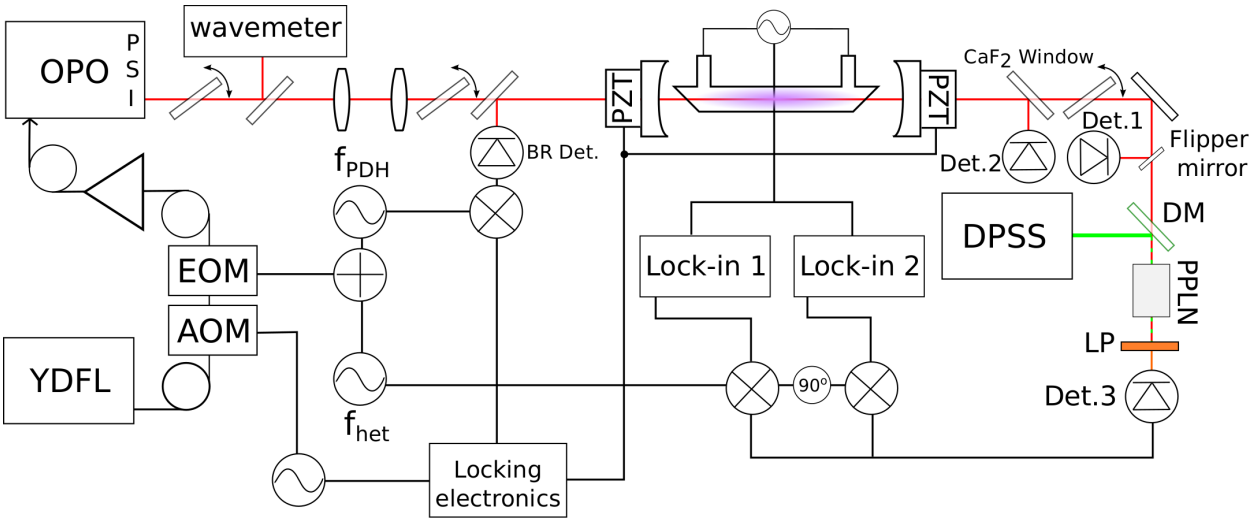

Figure 2.1: Experimental layout. YDFL: ytterbium doped fiber laser, AOM: acousto-optic modulator, EOM: electro-optic modulator, OPO: optical parametric oscillator, PZT: piezoelectric transducer, DPSS: diode-pumped solid-state laser, Det. 1: mid-IR transmission detector (Vigo PVM-10.6), BR Det.: back reflection detector (Boston Electronics Vigo PVI-4TE-6), Det. 2: mid-IR transmission detector (Boston Electronics Vigo PVI–4TE-6), Det. 3: silicon detector (Thorlabs DET025A), DM: dichroic mirror, and PPLN: periodically poled lithium niobate crystal.

locking [40] and heterodyne detection. The output from the EOM is amplified by an erbium doped fiber amplifier and fed into an optical parametric oscillator (OPO) which produces an idler (1 W, 3.2–3.9 μm) and a signal beam through parametric down-conversion. The idler beam is coupled into an external cavity (finesse 100) which contains a positive column discharge cell. The heterodyne frequency is set to an integer multiple of the FSR, allowing the sidebands and carrier to be resonant with the cavity. H_3^+ ions are produced by flowing 300 mTorr of hydrogen in a glow discharge cell while liquid nitrogen was flowed around the jacket surrounding the inner bore. The electrodes were driven sinusoidally at 40 kHz by a step-up transformer.

Light reflected off the cavity was picked off with a CaF_2 window and focused onto a thermoelectrically cooled fast mid-IR detector (Boston Electronics Vigo PVI-4TE-6) and used to produce the PDH error signal. This was sent to an analog lockbox which produces slow corrections (<100 Hz) which are sent to two piezoelectric transducers which control the cavity length. The fast corrections (100 Hz - 15 kHz) are sent to the AOM.

A fraction of the light transmitted from the cavity was picked off with a CaF_2 window and further attenuated with a wire-grid polarizer. The light was focused onto another thermoelectrically cooled fast mid-IR detector (Det. 2, Boston Electronics Vigo PVI-4TE-6), which has a 3 dB bandwidth (BW) of 600 MHz and a noise equivalent power (NEP) of 1.67×10^{-12} W Hz$^{-1/2}$. The light transmitted through the window was either sent to a slower mid-IR detector (Det. 1, Boston Electronics Vigo PVM-10.6) with a 3 dB BW of 160 MHz and NEP of 4.76×10^{-9} W Hz$^{-1/2}$, which was used in previous iteration of the instrument, or to the DFG optics. For DFG, the transmitted idler was colinearized with a high power (6.4 W) 532 nm beam from a diode-pumped solid-state laser (Coherent V10) using a dichroic mirror (ISP

Optics) and focused into a 4 cm MgO doped periodically poled lithium niobate (PPLN) crystal (MSFG612, Covesion Ltd). The optics before the dichroic mirror were designed to produce a confocal range (twice the Rayleigh range) equal to the length of the PPLN crystal. The PPLN crystal has poling periods from 10.4 - 11 μm and its temperature can be set from 30 - 200 °C, covering 3.2 - 3.9 μm. The up-converted light (616 - 638 nm) was selected with a long-pass filter and focused onto a fast silicon biased detector (Det. 3,Thorlabs DET025A) with a 3 dB BW of 2 GHz and NEP of 9.29 $\times 10^{-15}$ W Hz$^{-1/2}$.

Brewster-plate spoilers [56] were used to average out parasitic etalons in the system. This was accomplished by mounting CaF_2 windows onto galvanometers which were driven by a 35 Hz sawtooth wave for a full sweep of 1°. These were placed in front of the OPO, the mode-matching telescope, and the output mirror of the cavity.

For any given scan, the transmitted light was detected with Det. 1, 2, or 3. The output was first demodulated by a pair of electronic mixers referenced to the heterodyne frequency and set 90° out of phase with one another. The output from each mixer was sent to a two-channel lock-in amplifier that was referenced to twice the frequency driving the plasma to recover the velocity modulated signal [38]. All spectra were of the $R(1,0)$ transition of H_3^+ at 2725.8984 cm^{-1}. Scans were collected with the heterodyne modulation frequency set to 1, 3, and 5×FSR of the cavity (77, 231, and 385 MHz).

2.3 Results & discussion

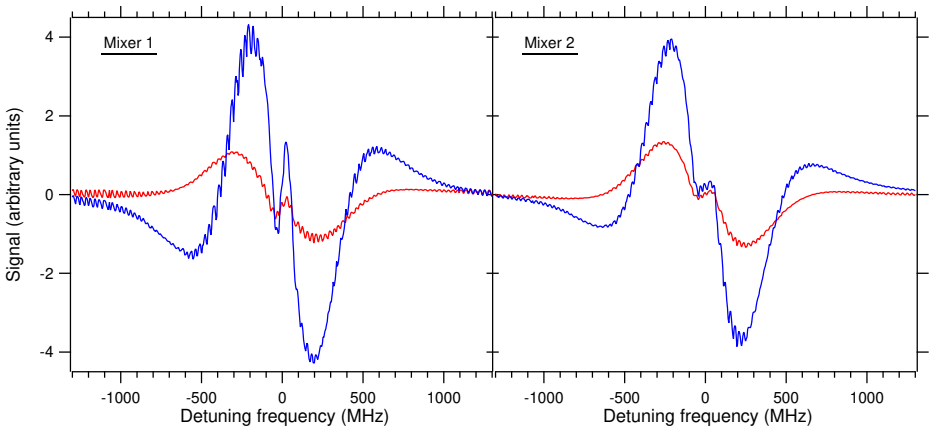

Figure 2.2: A NICE-OHVMS scan of the $R(1,0)$ transition of H_3^+, centered at 81720377 MHz (2725.8984 cm^{-1}) with the heterodyne frequency set to 1×FSR of the cavity (77.304 MHz). The red and blue traces represent the in-phase and quadrature components of the velocity modulation signal respectively. This scan was recorded with Det. 1.

An example of a NICE-OHVMS scan using the original detector (Det. 1) and without the Brewster-plate spoilers can be seen in Figure 2.2. The two layers of modulation produce the overall odd lineshape. The phase-modulated

light produces an FM triplet composed of a carrier and two sidebands separated by the modulation frequency. Each sideband produces a beat note with the carrier, which effectively cancel each other out when the triplet is balanced. If one or more components are on resonance with a transition, it disrupts the balance of the triplet and produces an intensity modulation of the light at the heterodyne frequency. The signal's strength and phase depend on the difference in absorption and dispersion of the sidebands and the carrier.

The second layer of modulation is velocity modulation. Within the discharge, the ions will follow the electric field causing their velocity distribution to oscillate at the frequency driving the plasma. In a single pass experiment, the signal from a charged carrier can be recovered with a lock-in amplifier referenced to the discharge frequency. In our case, the bidirectional nature of the cavity causes a simultaneous blue and red shift, and the signal is instead modulated at twice the driving frequency. The ions are also created and destroyed at twice the driving frequency, causing additional concentration modulation. Both the velocity and concentration modulation signals are recovered by the lock-in amplifiers. A more in depth description of cavity enhanced velocity modulation can be found in Siller *et. al* [38].

The sub-Doppler features at the center of the transition are the result of the high intracavity power and the bidirectional cavity. There are two counter propagating FM triplets, and each component can act as a pump/probe. When two counter propagating beams interact with the same velocity component, a Lamb dip can be formed that is much narrower than the overall profile. As the FM triplet is scanned over a transition, Lamb dips will occur at half-integer multiples of the heterodyne frequency centered around the rest frequency of the transition [57]. In Figure 2.2, the output from mixer 1 shows a central dispersion Lamb dip, while mixer 2 shows the first order absorption Lamb dips. A least-squares fitting routine can be used to determine the line centers with sub-MHz precision, as described in depth by Crabtree *et. al* [39].

2.3.1 Brewster-plate spoiler

Initially, our system had a number of etalons which spanned from 50 cm to 5 m in length, the effects of which can be seen in Figure 2.2 as fringing. For an etalon to be detectable, it must persist through demodulation at both the heterodyne frequency and twice the frequency driving the electrodes. An etalon can disrupt the balance of the FM triplet producing residual amplitude modulation (RAM), resulting in fringes spaced by the FSR in both absorption and dispersion [54]. While one might naively think that demodulating at the velocity modulation frequency would reject the RAM produced by an etalon, this is clearly not the case. A possible mechanism which would further affect the FM triplet at the velocity modulation frequency could be the changing index of refraction within the optical cavity. Because the refractive index will change with the concentration of ions and neutrals within the plasma, it will cycle twice every discharge period. This would cause the longitudinal modes of the cavity to modulate and, if the

PDH correction bandwidth is too slow, would introduce an intensity modulation at twice the driving frequency of the discharge. This would allow for the RAM of the etalon to pass through both layers of modulation.

Regardless of the mechanism, fringes from etalons do appear in the baseline of NICE-OHVMS scans and it should be possible to eliminate them with conventional methods. If the two surfaces of an unwanted etalon are separated such that ν_{het} = FSR the signal would go to zero since all three components of the FM triplet are affected equally. Previously, the modulation frequency in our experiment was limited to 77 MHz by the bandwidth of the detector making the required etalon immune distance 1.9 m, which would be impractical. The large detection bandwidth of Det. 2 and Det. 3 make it possible to increase the heterodyne frequency and reduce the etalon immune distance. Instead, a more flexible approach was taken.

Webster demonstrated that interference fringes could be averaged out by placing a Brewster-plate spoiler within the etalon [56]. A Brewster-plate spoiler is a window mounted at Brewster's angle on a galvanometer that is driven by a triangular wave, which rapidly changes the optical path length of the etalon. The change in optical path length (OPL) caused by placing a window within an etalon is shown in Figure 2.3. Rotating the window causes the frequency of individual fringes to shift rapidly. The change in path-length when the window is rotated from angle θ_{i1} to θ_{i2} was derived by Webster and is expressed by the following:

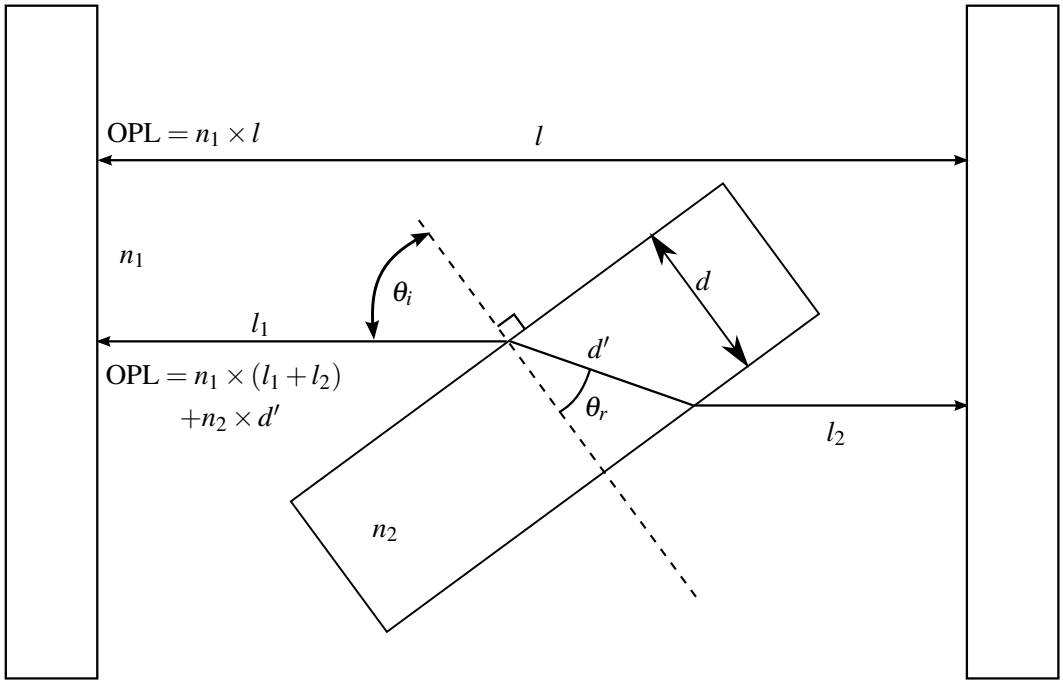

Figure 2.3: A depiction of the change in optical path length (OPL) to an etalon of length l when a window with a refractive index n_2, thickness d, and incident angle θ_i is placed between the reflective surfaces.

$$\Delta\text{OPL} = d_1'[\cos(\theta_{i1} - \theta_{r1}) + n_2] - d_2'[\cos(\theta_{i2} - \theta_{r2}) + n_2] \tag{2.1}$$

where ΔOPL is the change in the optical path length, θ_{i1} and θ_{i2} are the incident angles, θ_{r1} and θ_{r2} are the refracted angles, $d_i' = d/\cos(\theta_{ri})$ for the window's thickness d, and n_2 is the index of refraction of the plate. With a wavelength of 3.668 μm, a CaF_2 window with a thickness of 5 mm, a refractive index of 1.41, and the window placed at Brewster's angle (35.3°) for maximum transmission, a change of 1° leads to a change in optical path length of 60 μm. The shift in frequency which will occur from this is:

$$\Delta\nu = \frac{\nu\Delta L}{L} \tag{2.2}$$

The number of fringes for each sweep can be found by dividing by the etalon's FSR, yielding:

$$\frac{\Delta\nu}{\mathrm{FSR}} = \frac{2n\nu\Delta L}{c} \tag{2.3}$$

Therefore, a shift of 1° will average over 45 fringes in a single sweep and is independent of the etalon's length. We found that it took three total Brewster-plate spoilers to remove all observable etalon fringes; these were placed directly after the OPO, between the mode-matching telescope and the first cavity mirror, and in between the second cavity mirror and the detector. The effect can be seen in Figures 2.4 and 2.5. In Figure 2.5, the signal to noise increased from 125 to 2000 in the best channel.

An initial concern was the offset in the position of the laser beam that occurs as the angle of the window changes, which could disrupt the PDH lock to the cavity. However, despite two Brewster-plate spoilers being placed between the cavity and the OPO it did not introduce any significant noise to the scan.

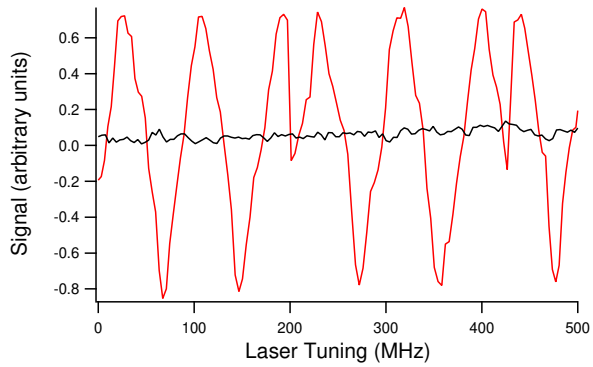

Figure 2.4: Comparison between the baseline when the galvanometer is on or off. The discontinuities in the fringe every ~200 MHz are caused when the cavity is relocked, which changes the optical path length of the cavity.

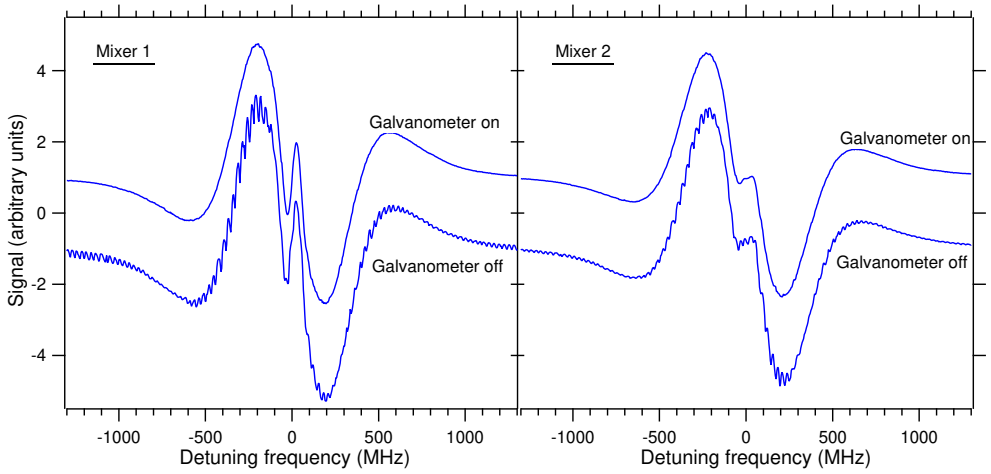

Figure 2.5: Comparison between two scans of the H_3^+ $R(1,0)$ transition with the galvanometer on (top) and galvanometer off (bottom). All traces are of the quadrature component of the lock-in amplifiers. Offsets were added for clarity.

2.3.2 Up-conversion detection

Difference frequency generation is a nonlinear process which takes two pump beams at frequencies ν_1 and ν_2 where $\nu_1 > \nu_2$, to produce a third ν_3 which follows the conservation of energy $\nu_1 - \nu_2 = \nu_3$. As a coherent process, the phase matching between the three beams is vital for effective conversion, *i.e.* $\Delta\boldsymbol{k} = \boldsymbol{k_1} - \boldsymbol{k_2} - \boldsymbol{k_3} = 0$, where $\boldsymbol{k_i}$ are the wave vectors. Angle phase matching in birefringent crystals was the original method for meeting this criterion. Modern optics make use of quasi-phase matching, where the crystals are grown to have the crystal orientation periodically changed over length Λ, which changes the phase matching requirement to $\Delta\boldsymbol{k} = \pi/\Lambda$. The intensity and interaction time determine the efficiency of the conversion. The Boyd-Kleinman focusing condition states that the maximum conversion efficiency occurs when the confocal length (twice the Rayleigh range) is equal to the length of the crystal [58]. With a 4 cm PPLN crystal, we generated 3 mW of 622 nm light from 70 mW of 3.667 μm light transmitted from the cavity and 6.4 W of 532 nm light. This equates to a conversion efficiency $\eta_{DFG} = 0.67\%/\mathrm{W}_{pump}$. The theoretical conversion efficiency was calculated with the SNLO software package [59] to be $1.2\%/\mathrm{W}_{pump}$. The discrepancy between the theoretical and measured efficiency is likley due to reflections off the PPLN input surface, absorption within PPLN, imperfect beam overlap, and a suboptimal confocal range.

The conversion efficiency was more than adequate when considering the sensitivity of the silicon detector. Up-conversion detection will ultimately sacrifice power for speed and sensitivity. Detector sensitivity is usually reported in noise equivalent power (NEP) in units of $\mathrm{W/Hz}^{1/2}$, which represents the amount of power required to produce a response with a S/N of 1 with a 1 Hz bandwidth. To compare all three detectors, it is important to consider how each is implemented into the NICE-OHMVS instrument, where the NEP should be converted to the noise equivalence of

Table 2.1: Technical specifications for the three detector used in this study, including the effective NEP. The noise equivalent power (NEP) for each detector is reported at 10.6 μm, 6 μm, and 730 nm for Det. 1, Det. 2, and Det. 3 respectively.

Detector	Coverage (μm)	NEP (W Hz$^{-1/2}$)	NEP$_{eff}$ (W Hz$^{-1/2}$)	3 dB BW (MHz)
Det. 1	2.5 – 11	4.76×10^{-9}	4.8×10^{-9}	160
Det. 2	2.8 – 6.5	1.67×10^{-12}	6.8 ×10^{-10}	700
Det. 3	0.35 – 1.1	9.29 × 10^{-15}	2.2 × 10^{-13}	2000

power transmitted from the cavity. For Det. 3, the losses due to up-conversion must be taken into account, and the effective NEP can calculated as shown in equation 2.4.

$$\text{NEP}_{eff} = \text{NEP}_{Det.3}/(\eta_{DFG} \times P_{pump}) \tag{2.4}$$

Here, NEP$_{eff}$ is the effective noise equivalent power of the detector, NEP$_{Det.3}$ is the noise equivalent power of Det. 3, and η_{DFG} is the efficiency of the DFG process in units of % converted/W$_{pump}$. For Det. 2, the losses from taking only a fraction of the light must be considered which is calculated by equation 2.5.

$$\text{NEP}_{eff} = \text{NEP}_{Det.2}/(P_{inc}/P_{tot}) \tag{2.5}$$

Here, NEP$_{Det.2}$ is the noise equivalent power of Det. 2, P_{inc} is the power incident on the detector, and P_{tot} is the total power transmitted from the cavity. This allows for a direct comparison between the sensitivity of the three detection schemes, as shown in Table 2.1. The comparison shows that, despite the suboptimal conversion efficiency, up-conversion should still have improved noise characteristics. Baseline measurements were collected for each detection scheme in 6 ms intervals over three minutes to determine the sensitivity and stability of each detector. Each channel was converted to units of cm^{-1} absorption and the Allan variance was calculated at binning sizes from 9 times the acquisition time (54 ms) to the total measurement time divided by 9 (20 s) to avoid artifacts that arise from using a small number of bins. The resulting Allan-Werle plots of the most sensitive channel from each detector are shown in Figure 2.6 [60].

The Allan deviation for all detectors scaled as $\tau^{-1/2}$, which is characteristic of white noise, up to the maximum integration time of 20 s. The Allan deviation for Det. 1, Det. 2, and Det. 3 with 2 s of averaging were 5.49×10^{-10} cm^{-1}, 1.5×10^{-10} cm^{-1}, and 1.7×10^{-11} cm^{-1} respectively. This has an equivalent detection bandwidth of 0.08 Hz, which gives a NEA of 2.0×10^{-9} cm^{-1} Hz$^{-1/2}$, 5.1 ×10^{-10} cm^{-1} Hz$^{-1/2}$, and 5.9×10^{-11} cm^{-1} Hz$^{-1/2}$ for Det. 1, Det. 2, and Det. 3 respectively. Therefore, up-conversion was found to be 33 times more sensitive than the original implementation with Det. 1, and is approximately an order of magnitude more sensitive than Det. 2. The improved sensitivity is reflected in the S/N enhancement of a scan of the R(1,0) transition of H_3^+. An example of a scan taken with up-conversion

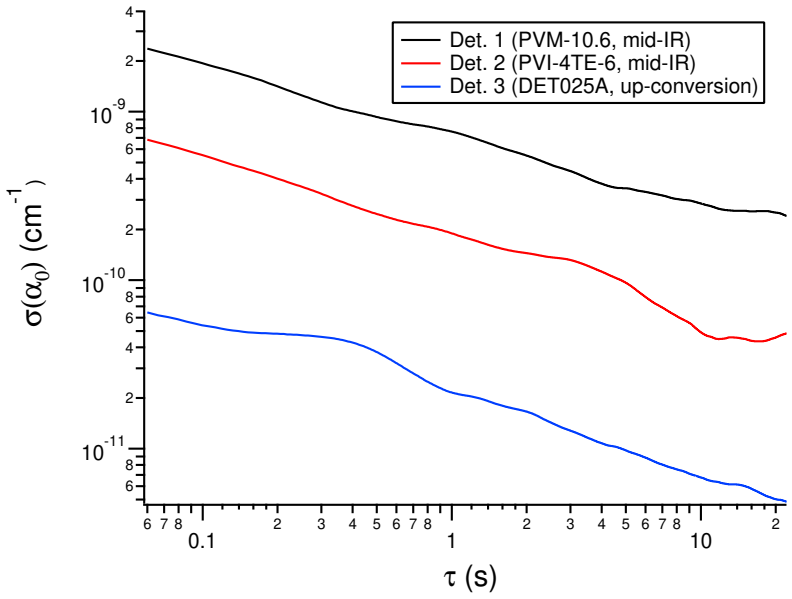

Figure 2.6: The Allan deviation of the equivalent absorption as a function of integration time τ. The measurement was taken over 180 s with the H_2 discharge on. The channels shown had the best noise characteristics for each detector.

detection using Det. 3 can be seen in Figure 2.7. The S/N was channel dependent, and ranged from 2600–14600. This is an improvement over best S/N taken with Det. 1 under the same conditions, which ranged from 1500 to 5700. Although this is a significant improvement over the previous iteration, it does not appear to directly scale with the NEA. When the baseline was closely inspected, weak fringes from an etalon still persist and are likely limiting the sensitivity when the frequency is scanned.

The increased bandwidth granted by Det. 2 and up-conversion with Det. 3 also allowed for optimization of the heterodyne modulation frequency. The strength of a NICE-OHMS signal depends on the difference in absorption or dispersion at the sideband and the carrier frequencies and the maximum signal occurs when the modulation frequency is near the full-width at half-maximum (FWHM). Due to limitations with the original detector (Det. 1), we were limited to a modulation frequency of 77 MHz, whereas Doppler broadened transitions of H_3^+ have widths of hundreds of MHz. Detector 2 and 3 have the necessary bandwidth to operate with optimized heterodyne frequencies near the FWHM.

A comparison between scans collected with a heterdoyne frequency of 1, 3, and 5×FSR of the cavity using Det. 2 can be seen in Figure 2.8. To compare the signal strength between scans at different detection angles, it is useful to compare the peak-to-peak signal strength summed in quadrature. The total signal was found to be optimized at 3×FSR of the cavity at 231 MHz, which was stronger by a factor of 3.6 in comparison to the 1×FSR scans. Scans with higher heterodyne frequencies were able to resolve the individual Lamb dips, which were found to have a width of approximately 70 MHz. This can be clearly seen in Figure 2.8 in the absorption channels where the Lamb dips

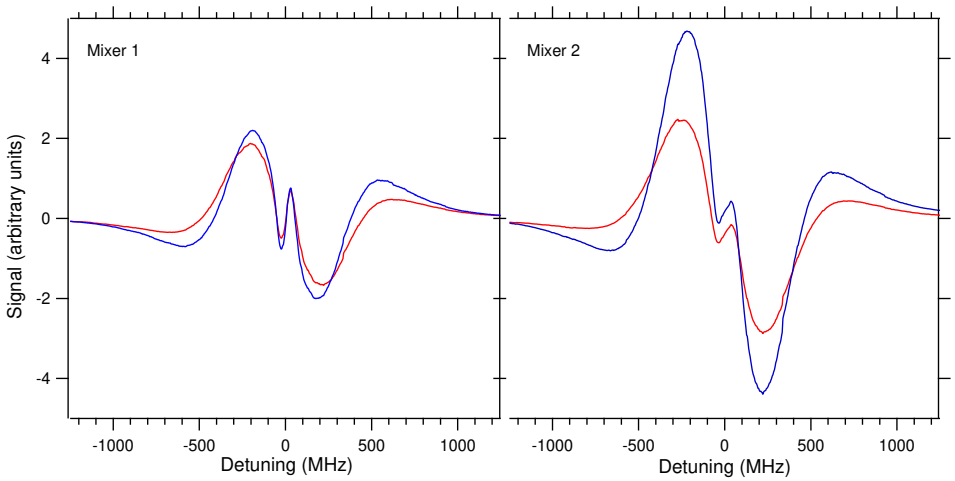

Figure 2.7: A NICE-OHVMS scan of the $R(1,0)$ transition of H_3^+ taken with up-conversion detection with Det. 3. The velocity modulation in-phase components are shown in red, and the quadrature component are shown in blue. The quadrature component of mixer 2 had a S/N of 14700.

overlap when the heterodyne frequency was 77 MHz and become resolved at 231 and 385 MHz. Unfortunately, the Lamb dips appeared to become smaller as the heterodyne frequency increased. which can be seen in Figure 2.8. A contributing factor is likely the width of the Lamb dips, which would produce an optimized signal at their FWHM near 70 MHz. Also, if the heterodyne was not perfectly matched to a multiple of the cavity's FSR, it would also result in a weaker Lamb dip. This could be avoided in the future experiments by locking the sidebands onto resonance with deVoe-Brewer locking [61].

Despite the smaller sub-Doppler features, resolving the individual Lamb dips opens doors to new experiments that were impossible with overlapping features. The narrower sub-Doppler feature could allow for resolving hyperfine structure. In a recent NICE-OHVMS study of OH^+, transitions with hyperfine components separated by ~120 MHz were treated as intensity-weighted averages [45]. A narrower central Lamb dip would enable resolved structure which would improve the predictions of the pure rotational spectra.

2.4 Conclusion

This work demonstrates that up-conversion detection and Brewster-plate spoilers are viable options for improving the sensitivity of the NICE-OHVMS technique in the mid-IR, and could be used in other NICE-OHMS instruments. When up-conversion was used with a Si biased detector, the NEA was improved by two orders of magnitude in comparison to the previous mid-IR detector. Additionally, to our knowledge this study is the first demonstration of a Brewster-plate spoiler in a cavity enhanced experiment, which effectively averaged out parasitic etalons in our measurements.

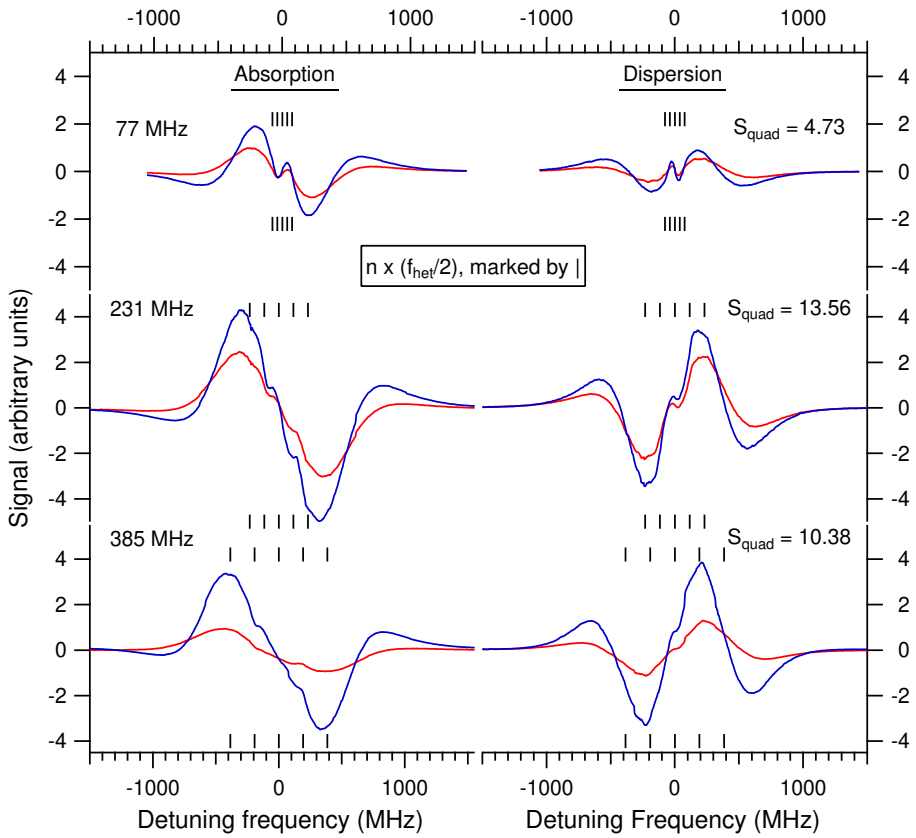

Figure 2.8: A comparison between scans taken with the heterodyne frequency set to 1, 3, and 5×FSR of the cavity with Det. 2. The in-phase component of velocity modulation is shown in red and the quadrature component in blue. The output of the mixers were set for absorption and dispersion shown on the left and right respectively. The vertical dashes are centered at the rest frequency and separated in half-integer multiples of the heterodyne frequency to indicate the expected Lamb dip frequencies. The peak-to-peak signal of all four channels summed in quadrature is denoted as S_{quad}.

Together, up-conversion detection and the Brewster-plate spoilers will enable precise measurements of transitions which were previously too weak to observe. and the Brewster-plate spoilers grant a significant improvement in S/N enabling future measurements of transitions with sub-MHz precision which were previously too weak to observe. We plan to use the improvements to complete the high-precision survey of H_3^+ transitions and explore new targets that were previously undetectable.

Chapter 3

Rovibrational spectroscopy of OH^+

3.1 Introduction

Molecular ions play a central role in the chemistry of the interstellar medium. Their reactivity with neutral species overshadows other chemical processes in the cold and diffuse environments of molecular clouds. One important example is OH^+, which is involved in a number of astrochemical processes. Its formation in diffuse clouds is initiated by cosmic ray ionization of atomic hydrogen into H^+, which can undergo an endothermic charge transfer with atomic oxygen to form O^+. Hydrogen abstraction with H_2 then leads to the subsequent formation of OH^+, H_2O^+, and H_3O^+. Dissociative recombination with electrons destroys all three of these species yielding neutral OH and H_2O along with other products. These competing processes allow for the relative abundances of OH^+, H_2O^+, and H_3O^+ to act as a probe of cosmic ray ionization rates and molecular hydrogen fractions in molecular clouds [18, 62, 63].

Due to interference of telluric water, observatories were only able to detect rotational transitions of H_3O^+ [64] until recently. The Heterodyne Instrument for the Far-Infrared (HIFI) aboard the orbiting telescope *Herschel* and high altitude ground based facilities enabled the first observations of H_2O^+ and OH^+ [65, 66]. The termination of *Herschel* has limited observations of OH^+ to high altitude observatories on the Atacama plateau and aboard aircraft such as the Stratospheric Observatory For Infrared Astronomy (SOFIA). Because of the low temperatures in translucent and diffuse molecular clouds, most of these measurements are of the ground state rotational transitions near 1 THz. There have also been observations of OH^+ by emission within our galaxy in photon-dominated regions (PDR) [67, 68, 69]. Highly rotationally excited transitions of OH^+ were detected with the moderate resolution Photodetector Array Camera and Spectrometer (PACS) onboard *Herschel* in absorption in the nearby galaxies Arp 220 and NGC 4418 by González-Alfonso *et al.* [70] and in emission in our galaxy by Aleman *et al.* [68].

The rotational structure of OH^+ arises from its $^3\Sigma^-$ ground electronic state. In this configuration, electron spin angular momentum **S** couples with the rotational angular momentum **N** as $\mathbf{J} = \mathbf{S} + \mathbf{N}$. A spin of $S = 1$ leads to the

This chapter is adapted with permission from Charles R. Markus, James N. Hodges, Adam J. Perry, G. Stephen Kocheril, Holger S. P. Müller, and Benjamin J. McCall, The Astrophysical Journal **817**, 138, (2016), Copyright 2016, The American Astronomical Society.

rotational levels splitting into fine structure triplets of $J = N + 1, N, N - 1$ with the exception of $N = 0$ where the only level is $J = 1$. The nuclear spin of $I = 1/2$ from the hydrogen nucleus splits each of these levels further into $F = J \pm 1/2$, where **F** is the total angular momentum. The strongest transitions follow the selection rule $\Delta F = \Delta J = \Delta N$. The only field free pure rotational measurements have been of the $N = 1 \leftarrow 0$ [71] and $N = 13 \leftarrow 12$ transitions [72]. There have also been investigations with laser magnetic resonance (LMR) going as far as $N = 3 \leftarrow 2$ [73]; though there have been cases, such as $H_2O^+$and CH_2, where the field-free transition frequencies extrapolated from LMR data had errors much larger than the claimed uncertainties [65, 74]. Rovibrational spectroscopy can help to improve the predictions of rotational transitions. Müller *et al.* [75] combined the field free rotational data [71, 72] with extensive infrared data by Rehfuss *et al.* [76] with reported uncertainties of 0.003 cm^{-1} (90 MHz) to determine an accurate set of Dunham-type spectroscopic parameters and to predict the rotational spectrum of OH^+ well into the terahertz region. Even at high frequencies, these predictions were accurate enough for studies with moderate resolution instruments [68, 70], but they may be not accurate enough for high resolution instruments, such as the German REceiver At Terahertz frequencies (GREAT, [77]) on board SOFIA. In the present work, we have therefore revisited the $v = 1 \leftarrow 0$ band of OH^+ with megahertz accuracy and determined improved molecular parameters from a least squares fit to a $^3\Sigma^-$ linear molecule effective Hamiltonian. The pure rotational spectrum was predicted in turn to assist future astronomical observations with high resolution instruments at terahertz frequencies.

3.2 Methods

The spectra were acquired with the technique Noise Immune Cavity-Enhanced Optical Heterodyne Velocity Modulation Spectroscopy (NICE-OHVMS) [78]. A detailed description of the instrument can be found in Hodges *et al.* [42]. In brief, a commercially available optical parametric oscillator (OPO; Aculight Argos 2400 SF) generates a continuous wave mid-infrared idler beam tunable from 3.2–3.9 μm with approximately 1 W of power. An electro-optic modulator applies an ~80 MHz phase modulation to the pump laser, imprinting RF sidebands onto the idler. The idler is coupled into an external cavity (finesse $\approx$ 150) which surrounds a water-cooled positive column discharge cell. The OH^+ ions were generated by flowing a 2:3:100 H_2:O_2:He mixture at 1.0 Torr through the cell and applying a 50 kHz sinusoidal discharge. Light transmitted through the cavity is focused onto a fast photodiode detector (Boston Electronics Vigo PVM-10.6-1x1). Two mixers referenced 90° out of phase with one another demodulate the signal from the detector at the frequency used to generate the sidebands. The velocity modulation signal is recovered by demodulating the output of each mixer at twice the driving frequency of the discharge (100 kHz) with a set of lock-in amplifiers. The in-phase and quadrature outputs of each lock-in amplifier produces two channels for each mixer, resulting in four total channels of detection.

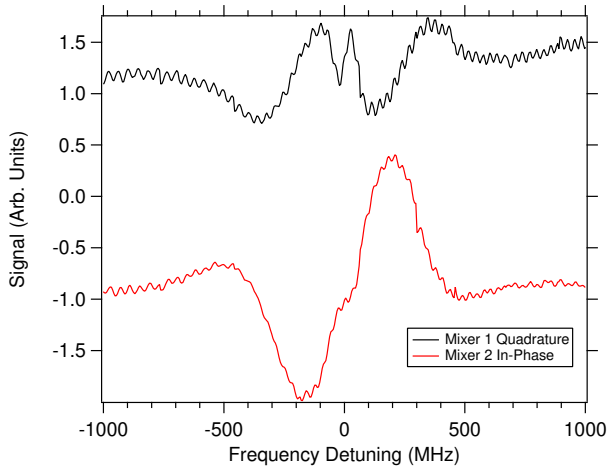

Figure 3.1: A NICE-OHVMS scan of $P(3)$ J = 3 ← 4 centered at 85557445.8 MHz. The top trace is the quadrature component of the velocity modulation of the first mixer and the bottom trace trace is the in-phase component of the second mixer. For clarity the traces are offset from one another.

Frequency calibration of the idler is accomplished by taking the difference of the pump and signal frequencies which are calibrated with an optical frequency comb (Menlo Systems FC-1500; 100 MHz repetition rate). Initially, an infrared wavemeter (Bristol 630:IR-A) was used to measure the pump and signal beams and determine the integer number of comb modes between them. The difference in frequency measured by the wavemeter must be accurate to within half the repetition rate (50 MHz), otherwise a 100 MHz systematic error would occur. To ensure proper determination of the difference in comb modes, systematic offsets of the wavemeter measurements are corrected by measuring methane reference transitions in the HITRAN database [79].

3.3 Results and analysis

Thirty lines were measured in the fundamental band with an average uncertainty of ~2.5 MHz, covering transitions $P(5)$ to $R(5)$. These results are displayed in Table 3.1. The frequencies reported by Rehfuss *et al.* [76] are frequently lower than the remeasured values, and only three transitions are at a higher frequency.

Table 3.1: Present transition frequencies (cm^{-1}) of the $v = 1 \leftarrow 0$ band of OH^+ with quantum numbers, uncertainties Unc. (10^{-6} cm^{-1}), and residuals O–C (10^{-6} cm^{-1}). Overlapping HFS components (with two sets of F quanta) were treated as intensity weighted averages. No HFS was resolved for entries without data.

N'	J'	N''	J''	$F' - F''$	Frequency	Unc.	O–C
4	4	5	5	···	2778.543347	43	−29.2
4	5	5	6	···	2778.752326	100	−101.5
3	2	4	3	1.5 – 2.5, 2.5 – 3.5	2816.464225	55	151.0
3	3	4	4	···	2816.730510	100	−28.3
3	4	4	5	3.5 – 4.5, 4.5 – 5.5	2816.948108	61	142.9

Table 3.1: (cont.)

2	1	3	2	0.5 – 1.5, 1.5 – 2.5	2853.236859	25	−36.6
2	2	3	3	···	2853.653079	80	21.6
2	3	3	4	2.5 – 3.5, 3.5 – 4.5	2853.889147	91	−92.4
1	0	2	1	0.5 – 1.5	2887.654424	230	−33.0
1	2	2	3	1.5 – 2.5, 2.5 – 3.5	2889.544385	46	−22.1
1	1	2	2	···	2889.261936	110	26.0
1	1	2	1	0.5 – 1.5, 1.5 – 1.5	2891.773633	105	−157.3
0	1	1	2	0.5 – 1.5, 1.5 – 2.5	2923.940929	63	−9.9
1	2	0	1	2.5 – 1.5, 1.5 – 0.5	2987.324274	96	9.9
1	1	0	1	0.5 – 1.5, 1.5 – 1.5	2989.353127	63	111.2
2	3	1	2	3.5 – 2.5, 2.5 – 1.5	3017.368784	61	−24.3
2	2	1	1	···	3017.612933	52	59.8
2	1	1	0	1.5 – 0.5	3019.241547	93	87.0
3	4	2	3	4.5 – 3.5, 3.5 – 2.5	3045.765058	65	25.1
3	3	2	2	···	3045.952199	69	63.0
3	2	2	1	2.5 – 1.5, 1.5 – 0.5	3046.372950	47	−59.5
4	5	3	4	5.5 – 4.5, 4.5 – 3.5	3072.547147	25	8.2
4	4	3	3	···	3072.705383	39	−45.4
4	3	3	2	3.5 – 2.5, 2.5 – 1.5	3072.964615	74	63.5
5	6	4	5	···	3097.691735	88	15.3
5	5	4	4	···	3097.831772	110	−126.9
5	4	4	3	···	3098.033887	230	13.1
6	7	5	6	···	3121.165108	130	−65.4
6	6	5	5	···	3121.292151	240	−76.2
6	5	5	4	···	3121.465385	70	84.3

A typical NICE-OHVMS scan can be seen in Figure 3.1. The odd lineshape is a result of the heterodyne and velocity modulation detection scheme. The sub-Doppler feature arises from the bidirectional nature of the cavity. Each component of the FM triplet can act as a pump and probe producing several Lamb dips separated at half integer multiples of the heterodyne frequency, and a least squares fitting routine can extract the line center. In cases where multiple detection channels had sufficient signal-to-noise, a simultaneous fit was performed where the line center, full width, and heterodyne frequency were shared parameters. A technical description of the sub-Doppler fitting procedure can be found in Hodges *et al.* [42]. Figure 4.2 is an example of a typical two channel fit with residuals. A large fringe, similar to the one seen in Figure 4.2, appeared in many of the spectra. The sub-Doppler fit does not appear to have been appreciably affected by the fringe since it is well reproduced within the residuals. Any random offset was further mitigated by collecting five measurements each transition and averaging the line center frequencies. The uncertainty of each transition is reported as the standard deviation and shows an order of magnitude improvement over previous values. However, the precision of this study is not at the sub-MHz level as was achieved in other NICE-OHVMS

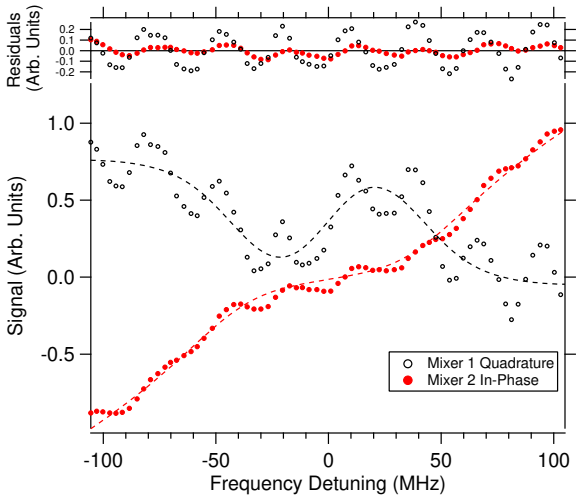

Figure 3.2: An enlarged comb calibrated scan of the sub-Doppler feature of $P(3)$ J = 3 ← 4. The colored markers represent the experimental data and the dashed lines represent the fit to the sub-Doppler feature. The residuals from the fit are shown above, which reproduce the fringing seen in the experimental trace.

studies [42, 44]. This can be attributed to the lower signal-to-noise which is known to decrease the precision of the line centers [42]. The weak signals are likely a result of competing chemical processes such as the formation of H_2O^+. Gas mixtures with dilute quantities of H_2 can minimize this effect but still result in relatively weak signals.

Parameters for the $v = 0$ and $v = 1$ states were determined initially with a two-state fit of the newly measured frequencies and all data in CDMS [75] up to $v = 1$ in order to compare the compatibility of the previously reported transition frequencies and the derived spectroscopic parameters with our data. The transition frequencies from the present investigation were added to the line list as determined, i.e. in units of wavenumber. Overlapping HFS components were treated in the fits as intensity-weighted averages, as is commonly done in fits employing the spfit/spcat program suite [80].

Comparing the new experimental transition frequencies with a prediction of the $v = 1 \leftarrow 0$ spectrum with ^{1}H hyperfine structure (HFS) revealed that a total of four of our lines should show partially resolved HFS splitting of ~0.004 cm^{-1} or ~120 MHz, slightly larger than the sub-Doppler feature's width. Ultimately, trial fits and comparisons with Doppler-limited spectra established that in all four cases the frequencies determined by the Lamb dips corresponded to the stronger of the two lines with similar intensities. In all four cases the weaker line was on the side of the stronger line's Doppler profile, making precise frequency determination impossible. Hyperfine splitting turned out to be non-negligible for lower-N transitions with $J = N \pm 1$ because the weak $\Delta F \neq \Delta J$ HFS components were separated from the two much stronger $\Delta F = \Delta J$ components by ~120 MHz. Because of the small uncertainties of some of our lines, these differences were important for lower-N transitions. The relative intensities of these HFS components diminish rapidly with N, so the effects were negligible at higher N.

Table 3.2: Spectroscopic parameters from a two-state fit (MHz) of OH^+ in comparison to previous studies. Numbers in parentheses are one standard deviation in units of the least significant digits.

Parameter	This work	Prev. IR [76]	Prev. LMR [73]
B_0	492346.278(146)	492345(2)	492346.21(69)
D_0	57.6166(52)	57.614(24)	57.544(75)
H_0	0.0040488(259)	0.004062(87)	0.0037
λ_0	64246.00(55)	64258(18)	64242.9(88)
λ_{D0}	-0.54(12)	···	···
γ_0	-4533.85(34)	-4529.3(53)	-4534.76(124)
γ_{D0}	0.7847(153)	0.90(15)	···
$b_F(^1H)$	-75.14(50)	···	-71.9(125)
$c(^1H)$	126.01(87)	···	130.8(202)
ν_0	88629394.08(91)	88629737(30)	···
B_1	470532.242(135)	470532(2)	···
D_1	56.1557(44)	56.16(2)	···
H_1	0.0039501(243)	0.003969(81)	···
λ_1	63947.4(13)	63949(15)	···
λ_{D1}	-0.86(12)	···	···
γ_1	-4393.34(38)	-4394.1(45)	···
γ_{D1}	0.7473(130)	0.812(48)	···

The quality of a fit was measured using the root mean square (rms) of the errors between the observed and calculated frequencies normalized to their uncertainties, which ideally should be close to 1.0. Starting with the spectroscopic parameters used by Rehfuss *et al.* [76] and the HFS constants b_F and c, it was found that the spin-spin distortion constant λ_D was needed to achieve an rms error of 1.006. The results are shown in Table 3.2 with comparisons to Rehfuss *et al.* [76] and Gruebele *et al.* [73]. The uncertainties of the rotational constant B, centrifugal distortion constant D, and the spin-spin coupling constant λ for both $v = 0$ and $v = 1$ states were significantly improved. The constants determined by Gruebele *et al.* [73] from LMR data are in strong agreement, with every parameter falling within their reported uncertainty. Nearly every parameter from [76] agrees with the results with the exception of the band origin ν_0 which is 343 MHz higher. We have not been able to determine the cause of this discrepancy.

Subsequently, our data were combined with the complete set of previously available field-free data to determine an improved set of Dunham-type spectroscopic parameters. The parameter set used by Müller *et al.* [75] for the analysis of $OH^+$was not sufficient to reproduce the present data adequately. Trial fits were performed to search among all plausible parameters for the one which reduced the rms error of the fit the most. The parameter λ_{20}, the second vibrational correction to the spin-spin coupling parameter λ_{00}, was added first. The vibrational correction γ_{11} to the spin-rotation distortion term had a moderate effect in the overall fit, but improved the reproduction of our transition frequencies by ∼16 %. Finally, we noted that the $v = 5 \leftarrow 4$ transition frequencies from Rehfuss *et al.* [76] showed very similar deviations somewhat larger than the increased uncertainties of 0.010 cm^{-1}. Inclusion of Y_{50} in the fit not only reproduced these data much better, but also reduced the rms error of the fit considerably. Consequently,

the uncertainties of this vibrational band were put to the initial 0.003 cm^{-1}, and the fit was rerun. The resulting spectroscopic parameters are in Table 3.3 together with previous values for OH^+ [75] as well as recent values for its heavier homolog SH^+ [81].

The rms error of the present fit is 0.908, hence on average the experimental transition frequencies have been reproduced within their uncertainties. The values for our data and the $v = 1 \leftarrow 0$ data of Rehfuss *et al.* [76] are 1.062 and 1.107, respectively. The latter data are on average lower than the calculated frequencies by 0.0013 cm^{-1} or 40 MHz, which may indicate a calibration error of approximately that magnitude. The diviations are, however, within the reported uncertainties of 0.003 cm^{-1} or 90 MHz [76]. An *a posteriori* correction of these data will likely improve the reproduction of these data and may even be beneficial for reproducing our data.

Table 3.3: Present and previous spectroscopic parameters (MHz, cm^{-1}) of OH^+ in comparison to those of SH^+. Numbers in parentheses are one standard deviation in units of the least significant digits.

Parameter	This work	Previous [75]	SH^+ [81]
Y_{10}[a]	3119.2892 (56)	3119.3173 (27)	2547.4948 (104)
Y_{20}[a]	−83.1273 (57)	−83.1606 (19)	−49.4293 (90)
Y_{30}[a]	1.01953 (241)	1.03525 (55)	0.2097 (30)
$Y_{40} \times 10^3$ [a]	2.435 (453)	−0.795 (54)	−16.01 (34)
$Y_{50} \times 10^3$ [a]	−0.241 (31)	···	···
Y_{01}	503486.90 (26)	503486.86 (70)	278094.99 (36)
Y_{11}	−22435.77 (62)	−22435.87 (151)	−8577.33 (85)
Y_{21}	308.47 (39)	308.28 (55)	16.15 (32)
Y_{31}	−1.410 (51)	−1.434 (61)	···
Y_{02}	−58.3436 (59)	−58.3607 (128)	−14.7380 (76)
Y_{12}	1.4649 (37)	1.4649 (105)	0.1229 (27)
$Y_{22} \times 10^3$	7.51 (137)	7.03 (192)	···
$Y_{03} \times 10^3$	4.115 (31)	4.184 (57)	0.46[b]
$Y_{13} \times 10^3$	−0.1326 (187)	−0.1733 (288)	···
λ_{00}	64379.5 (26)	64413.2 (38)	171488.3 (58)
λ_{10}	−254.3 (66)	−340.2 (79)	−471.8 (146)
λ_{20}	−24.1 (33)	···	−79.1 (67)
λ_{01}	−0.68 (11)	0.75 (59)	−1.13 (24)
γ_{00}	−4605.16 (42)	−4604.23 (108)	−5036.29 (91)
γ_{10}	143.47 (67)	142.58 (220)	116.4 (20)
γ_{20}	−1.45 (35)	−2.14 (52)	3.52 (64)
γ_{01}	0.796 (17)	0.789 (54)	0.432 (35)
γ_{11}	−0.0354 (88)	···	···
$b_{F,00}(^1H)$	−75.11 (49)	−74.78 (54)	−55.15 (40)[c]
$b_{F,10}(^1H)$	···	···	−3.46 (79)
$c_{00}(^1H)$	125.95 (87)	125.48 (94)	33.60 (67)

[a] In units of cm^{-1}.

[b] Held fixed in Müller *et al.* [81].

[c] Derived from Müller *et al.* [81].

Most of the present spectroscopic parameters of OH^+ are close to the previous ones. Larger changes occur for parameters which have relatively large uncertainties, e.g. λ_{01}, or by inclusion of additional higher order parameters if their values appear rather small in magnitude compared to the parameters of lower and higher order (Y_{40} and λ_{10}). The Y_{ij} of different isotopic species scale with $\mu^{-j-i/2}$, where μ is the reduced mass. The ratios of several spectroscopic parameters of OH^+ and SH^+ are surprisingly close to these ratios, but the magnitude of Y_{40} of SH^+ is actually much larger than that of OH^+.

The ratio of λ_{00} of related molecules such as SH^+ and OH^+ scale with the ratios of A_{SO}, ~2.64, which holds quite well in the present case. The slight change in b_F and the larger change in c are usually seen for light hydrides compared to their heavier homologs. Predictions from $N = 1 - 0$ to $N = 5 - 4$ are presented in Table 3.4 with comparison to predictions from the current version of the CDMS. The predicted THz transitions from this work show strong agreement with the predictions from CDMS and improve the precision by a factor of 2 - 5. More extended predictions will be available in the catalog section of the CDMS.

These predictions can guide new searches in regions where it is feasible that OH^+ is rotationally excited. The only spectrograph currently capable of observing transitions of OH^+ above $N = 1 - 0$ is the recently upgraded GREAT instrument aboard the airborne SOFIA which covers all of the $N = 2 - 1$ rotational transitions. Rotational emission of OH^+ has been observed in the Orion Bar. Calculations performed by van der Tak *et al.* [67] suggest that the reason for the excitation of OH^+ in the Orion Bar is likely a combination of collisional excitation, radiative pumping, and formation pumping. It would be interesting to search this region for $N = 2 - 1$ emission, which would enable deeper understanding of this environment. Rotationally excited transitions of OH^+ were already detected at moderate resolution in nearby galaxies [70] and in our galaxy [68].

Table 3.4: Predicted rotational transitions of OH^+ (MHz)

$N' - N''$	$J' - J''$	$F' - F''$	This work	CDMS [75]
1 – 0	0 – 1	1/2 – 1/2	909045.0(8)	909045.2(10)[a]
1 – 0	0 – 1	1/2 – 3/2	909159.4(8)	909158.8(10)[a]
1 – 0	2 – 1	5/2 – 3/2	971804.2(5)	971803.8(15)[a]
1 – 0	2 – 1	3/2 – 1/2	971805.3(5)	971805.3(15)[a]
1 – 0	2 – 1	3/2 – 3/2	971919.7(7)	971919.2(10)[a]
1 – 0	1 – 1	1/2 – 1/2	1032998.6(7)	1032997.9(8)
1 – 0	1 – 1	3/2 – 1/2	1033005.1(7)	1033004.4(10)[a]
1 – 0	1 – 1	1/2 – 3/2	1033112.9(7)	1033111.8(9)
1 – 0	1 – 1	3/2 – 3/2	1033119.5(7)	1033118.6(10)[a]
2 – 1	1 – 1	1/2 – 3/2	1892111.1(9)	1892106.5(20)
2 – 1	1 – 1	1/2 – 1/2	1892117.7(9)	1892113.2(19)
2 – 1	1 – 1	3/2 – 3/2	1892232.1(8)	1892227.1(19)
2 – 1	1 – 1	3/2 – 1/2	1892237.7(8)	1892233.7(19)

Table 3.4: (cont.)

2 – 1	3 – 2	7/2 – 5/2	1959561.6(6)	1959560.0(13)
2 – 1	3 – 2	5/2 – 3/2	1959562.0(6)	1959560.4(13)
2 – 1	2 – 1	3/2 – 3/2	1967533.1(6)	1967535.9(19)
2 – 1	2 – 1	5/2 – 3/2	1967536.7(6)	1967539.6(19)
2 – 1	2 – 1	3/2 – 1/2	1967539.7(6)	1967542.6(19)
2 – 1	1 – 0	1/2 – 1/2	2016071.1(8)	2016066.1(20)
2 – 1	1 – 0	3/2 – 1/2	2016192.2(7)	2016186.6(19)
2 – 1	2 – 2	3/2 – 3/2	2028732.9(10)	2028735.2(20)
2 – 1	2 – 2	5/2 – 5/2	2028852.0(11)	2028853.9(20)
3 – 2	2 – 2	3/2 – 3/2	2885078.7(13)	2885065.0(51)
3 – 2	2 – 2	5/2 – 5/2	2885194.2(13)	2885179.9(51)
3 – 2	4 – 3	9/2 – 7/2	2941432.3(6)	2941428.8(21)
3 – 2	4 – 3	7/2 – 5/2	2941432.5(6)	2941429.0(21)
3 – 2	4 – 3	7/2 – 7/2	2941548.4(8)	2941544.5(20)
3 – 2	3 – 2	5/2 – 5/2	2947851.2(6)	2947854.9(28)
3 – 2	3 – 2	7/2 – 5/2	2947853.8(6)	2947857.5(28)
3 – 2	3 – 2	5/2 – 3/2	2947854.9(6)	2947858.6(28)
3 – 2	2 – 1	3/2 – 3/2	2960379.6(10)	2960373.8(25)
3 – 2	2 – 1	5/2 – 3/2	2960498.8(6)	2960492.5(23)
3 – 2	2 – 1	3/2 – 1/2	2960500.7(6)	2960494.4(23)
3 – 2	3 – 3	5/2 – 5/2	3017025.7(15)	3017033.4(48)
3 – 2	3 – 3	7/2 – 7/2	3017144.2(16)	3017151.3(48)
4 – 3	3 – 3	7/2 – 7/2	3869337.1(22)	3869310.2(97)
4 – 3	5 – 4	11/2 – 9/2	3918330.7(8)	3918324.8(33)
4 – 3	5 – 4	9/2 – 7/2	3918330.8(8)	3918324.9(33)
4 – 3	4 – 3	9/2 – 7/2	3924036.3(7)	3924040.2(41)
4 – 3	4 – 3	7/2 – 5/2	3924036.8(7)	3924040.8(41)
4 – 3	3 – 2	7/2 – 5/2	3931996.7(9)	3931987.8(35)
4 – 3	3 – 2	5/2 – 3/2	3931997.4(9)	3931988.4(35)
4 – 3	4 – 4	9/2 – 9/2	3999748.2(22)	3999762.7(90)
5 – 4	6 – 5	13/2 – 11/2	4889412.3(13)	4889403.4(52)
5 – 4	6 – 5	11/2 – 9/2	4889412.4(13)	4889403.5(52)
5 – 4	5 – 5	11/2 – 9/2	4894719.8(9)	4894723.3(57)
5 – 4	5 – 4	9/2 – 7/2	4894720.2(9)	4894723.7(57)
5 – 4	4 – 3	9/2 – 7/2	4901121.3(15)	4901108.8(53)
5 – 4	4 – 3	7/2 – 5/2	4901121.7(15)	4901109.2(53)

a:[71]

Chapter 4

Rovibrational spectroscopy of D_2H^+

4.1 Introduction

H_3^+ and its isotopologues are the simplest polyatomic molecules, and their experimentally determined energy levels act as valuable benchmarks for cutting-edge *ab initio* theory [25]. Calculations which go beyond the Born–Oppenheimer approximation with corrections for adiabatic, non-adiabatic, and relativistic effects should be of similar quality for all isotopologues, making H_2D^+ and D_2H^+ of particular importance for investigations of H_3^+ [35].

H_3^+ also plays a central role in the chemistry of molecular clouds, where it is generated by cosmic ray ionization of H_2 and initiates a chain of ion–neutral reactions [14, 15]. Despite the estimated low galactic D/H ratio of 2.3×10^{-5} [82], deuterium fractionation leads to significant abundances of D_2H^+ in cold and shielded regions such as dense molecular clouds and prestellar cores [83]. The first astronomical observation of D_2H^+ was of its $1_{10} \rightarrow 1_{01}$ rotational transition in a prestellar core. It was found to be in similar abundance to H_2D^+, which helped confirm new models of deuterium chemistry [84]. The $1_{11} \leftarrow 0_{00}$ transition has since been observed with the German REceiver for Astronomy at Terahertz frequencies (GREAT) on board the airborne Stratospheric Observatory For Infrared Astronomy (SOFIA), where the *ortho* to *para* ratio of D_2H^+ helped determine the age of the prestellar core [85]. The $3_{22} - 3_{13}$ and $4_{13} - 4_{04}$ transitions near 2.5 THz are within the coverage of GREAT, and their predicted frequencies have uncertainties of 5–15 MHz [75]. However, the energies of the 3_{13} and 4_{04} states are 200 cm^{-1} (288 K) and 316 cm^{-1} (454 K) respectively, and to have sufficient population for an observation the rotational temperature would need to be higher than that of a dense molecular cloud. If an event caused the cloud to be warmed after D_2H^+ was generated, such as the formation of a protostar, observations of these transitions could become feasible.

To date, there have been seven pure rotational transitions of D_2H^+ measured in either extended negative glow discharges or cold ion traps [86, 87, 88, 89]. The remaining THz transitions must be inferred indirectly using rovibrational data via combination differences (CDs) or spectroscopic constants by fitting to an effective Hamiltonian. So far,

10 rovibrational transitions have been measured with sub-MHz uncertainties by laser induced reaction spectroscopy [90]. The remaining data from multipass absorption experiments have estimated uncertainties of 60 MHz [91, 92]. To obtain MHz-level uncertainty on calculated THz transitions, more extensive rovibrational data are needed.

Here, we report the measurement of 37 rovibrational transitions of D_2H^+ in the ν_1 fundamental band using the technique Noise Immune Cavity Enhanced Optical Heterodyne Velocity Modulation Spectroscopy (NICE-OHVMS) [78]. Of these, 10 had never been observed and 17 had their uncertainties reduced from 60 MHz to 2 MHz. Using CDs and a fit to an Euler Hamiltonian [93], improved predictions of unobserved THz transitions are provided.

4.2 Methods

In order to precisely determine the rest frequencies of rovibrational transitions, measurements must overcome Doppler broadening which can be on the order of several 100 MHz. Sub-Doppler spectroscopy uses counter-propagating beams to generate a Lamb dip centered at the rest frequency, where the width is determined instead by the much smaller homogeneous broadening. Sub-Doppler spectroscopy of molecular ions in laboratory plasmas is challenging given that ions have large collisional cross sections, which significantly increases the homogeneous broadening. In addition, ions are generated in low abundances requiring sensitive spectroscopic techniques. The technique Noise-Immune Cavity-Enhanced Optical Heterodyne Molecular Spectroscopy (NICE-OHMS) is highly sensitive and can generate a large amount of intracavity power which is beneficial for sub-Doppler spectroscopy [41]. However, NICE-OHMS can suffer from background signals due to parasitic etalons and residual amplitude modulation [94], and to mitigate these we have implemented velocity modulation [37] as an additional layer of modulation in the combined technique NICE-OHVMS [78].

All measurements were obtained using our NICE-OHVMS instrument, which has been described previously [42]. In brief, ~1 W of tunable mid-infrared (mid-IR) light from an optical parametric oscillator (OPO, Aculight Argos 2400 SF) is locked to an external cavity (finesse ~150) using a Pound–Drever–Hall scheme. A fiber-coupled elecro-optic modulator phase modulates the pump laser of the OPO at a frequency equal to the free spectral range of the cavity (77 MHz). This allows for the FM sidebands used for heterodyne detection to be generated on the mid-IR idler beam and coupled into cavity modes adjacent to the carrier. The cavity surrounds a triple-jacketed positive column discharge cell, "Black Widow" [95]. Ions are generated by flowing a 2:1 mixture of D_2:H_2 through the cell at 470 mTorr of total pressure, and electrodes at the ends of the cell are driven by a 50 kHz 2 kV peak-to-peak sinusoidal voltage from a step-up transformer. The ions are cooled by flowing either liquid nitrogen or chilled water around the inner cell, achieving rotational temperatures of 170 and 600 K respectively. A CaF_2 window is used to pick off 500 μW of the light transmitted from the cavity, which is focused onto a fast mid-IR thermoelectrically cooled MCT

detector (VIGO PVI-4TE-6). The signal is first demodulated by a pair of RF mixers referenced to the heterodyne modulation frequency, and a 90° delay cable is used to obtain the in-phase (dispersion) and quadrature (absorption) signals. The outputs of the mixers are further demodulated by a pair of lock-in amplifiers referenced to twice the discharge frequency (100 kHz) to recover the velocity modulation signal.

Accurate frequency calibration of the idler is accomplished by measuring the difference between the pump and signal frequencies of the OPO using a GPS-referenced optical frequency comb (Menlo Systems FC-1500, 100 MHz repetition rate). The integer difference in comb modes is determined using a mid-IR wavemeter, and the signal beam is locked at a 20 MHz offset to the nearest comb tooth using a phase-locked loop. The frequency is scanned by stepping the pump frequency in 2 MHz increments, and a double-pass acousto-optic modulator (AOM) keeps the beat between the pump and the nearest comb tooth within a bandpass centered at 30 MHz using a feed-forward scheme [96]. When the AOM reaches the end of its diffraction efficiency, it jumps 100 MHz to the next comb tooth. With this, the idler frequency can be determined to within 100 kHz.

4.3 Results

An example NICE-OHVMS scan of the $2_{11} \leftarrow 2_{02}$ transition of the ν_1 fundamental band of D_2H^+ can be seen in Figure 4.1. The detection angle can be set such that the dispersion (in-phase) and absorption (quadrature) components of the signal are separated. The overall odd lineshape is the Doppler profile, and the narrower feature at the center is a set of Lamb dips separated by half-integer multiples of our heterodyne frequency centered around the line center. The homogeneous broadening is approximately 70 MHz, causing these features to overlap. The sub-Doppler feature is fit using Lorentzian functions for the Lamb dips and the Doppler profile is fit with a cubic function centered at the line center, which is shown in Figure 4.2. By fitting all channels simultaneously, the line center can be determined as described by Hodges *et al.* [42].

When we measured 5 scans of the $2_{21} \leftarrow 1_{10}$ transition we found a standard deviation of 300 kHz, but when we compared this to Jusko *et al.* [90] we found it was in error by 3.1 MHz. Similar results were found with other transitions. First, we confirmed that the source of the error was not our frequency calibration using sub-Doppler measurements of methane with a double-pass experiment [96]. Ultimately, we found that small adjustments to the alignment to our cavity would cause one of the lobes of the Doppler profile to be diminished, giving the appearance of the Lamb dip being nearer to the top or bottom of the Doppler profile. This caused a shift in the frequency from the fit and structure to appear in the residuals due to the Doppler profile not being centered around the Lamb dips. The asymmetries in the Doppler profile persisted when the heterodyne modulation was removed for scans using cavity-enhanced velocity modulation spectroscopy, and without velocity modulation in Noise-Immune Cavity-Enhanced

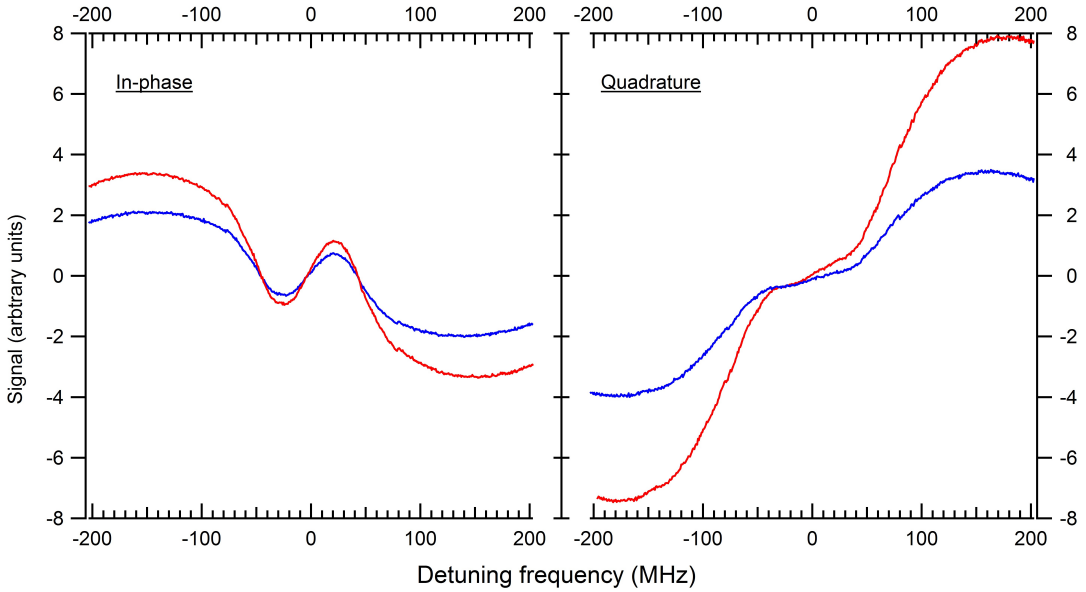

Figure 4.1: A NICE-OHVMS scan of the $2_{11} \leftarrow 2_{02}$ transition of the ν_1 fundamental band of D_2H^+, with the frequency offset by 83035089.34 MHz for clarity. The left plot displays the in-phase channels with respect to heterodyne detection, while the right plot displays the quadrature signals. The red and blue traces represent the in-phase and quadrature components of velocity modulation respectively.

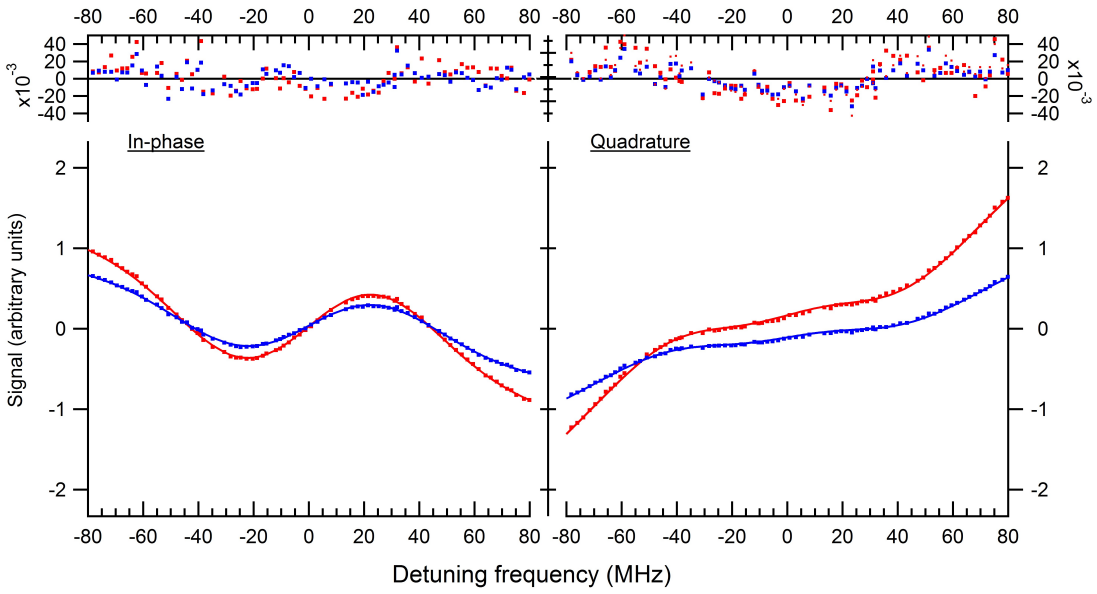

Figure 4.2: The sub-Doppler feature of a NICE-OHVMS scan of the $2_{11} \leftarrow 2_{02}$ transition of the ν_1 fundamental band of D_2H^+, with the frequency offset by 83035089.34 MHz for clarity. The points represent the data and solid traces represent the fit, with the residuals shown above. The left plot displays the in-phase channels with respect to heterodyne detection, while the right plot displays the quadrature signals. The red and blue traces represent the in-phase and quadrature components of velocity modulation respectively.

Optical Heterodyne Molecular Spectroscopy (NICE-OHMS) scans of methane.

This turned out to be useful, as the NICE-OHMS scans of methane could be used to quantify the asymmetry. The Doppler profile of methane transitions were fit to a NICE-OHMS lineshape with an asymmetry parameter. The angle of injection was adjusted until the asymmetry was eliminated, and then scans of D_2H^+ were collected with the same alignment. The D_2H^+ Lamb dips would then appear centered on the Doppler profile, improving the quality of the fits. This reduced the discrepancy with the values reported by Jusko *et al.* to within 1.05 MHz. We were also able to compare energy level spacings determined by CDs with highly accurate rotational data, in which all agreed within 1.9 MHz. More information can be found in Section 4.6.

Using methane to set the alignment before each set of scans, we measured 37 transitions in the ν_1 fundamental band. The line center frequencies, which are the average of two sets of 4–5 scans taken on two separate days, are listed in Table 4.1 with comparisons to previous values. The uncertainty for each transition is reported as 2 MHz or the standard deviation of all scans, whichever is larger. Of these 37 transitions, 10 had never been previously observed and 17 were only known to within 60 MHz.

Table 4.1: Transition frequencies of the ν_1 fundamental band from this work with residuals (O–C) from the fit and comparisons with previous studies. The 1σ uncertainties are given in parentheses.

Transition	This work (MHz)	O–C (MHz)	Prev. Value (MHz)	Diff.	Ref.
$2_{11} \leftarrow 3_{22}$	77590937.46(200)	-2.92	–		
$1_{10} \leftarrow 2_{21}$	78389394.87(200)	-1.93	–		
$3_{13} \leftarrow 4_{04}$	78509936.60(200)	-3.39	–		
$2_{02} \leftarrow 3_{13}$	79070989.38(200)	-0.94	79070980(60)	9.38	[91]
$2_{12} \leftarrow 3_{03}$	79433535.00(200)	-1.53	–		
$4_{04} \leftarrow 4_{13}$	79446380.39(211)	4.13	–		
$3_{13} \leftarrow 3_{22}$	79481913.99(200)	1.04	–		
$1_{01} \leftarrow 2_{12}$	79782520.69(200)	1.22	79782508(60)	12.69	[91]
$2_{12} \leftarrow 2_{21}$	79941256.46(200)	-2.73	–		
$1_{11} \leftarrow 2_{02}$	80452752.63(200)	0.98	80452751.59(75)	1.04	[90]
$0_{00} \leftarrow 1_{11}$	80575855.74(200)	0.24	80575855.46(12)	0.28	[90]
$3_{12} \leftarrow 3_{21}$	80615629.64(200)	1.62	–		
$2_{11} \leftarrow 2_{20}$	80626375.46(200)	0.15	–		
$1_{01} \leftarrow 1_{10}$	81349548.28(200)	-0.01	81349548.38(15)	-0.10	[90]
$1_{10} \leftarrow 1_{01}$	82713780.02(200)	-0.35	82713780.40(15)	-0.37	[90]
$2_{11} \leftarrow 2_{02}$	83035089.34(200)	-0.83	83035106(60)	-16.66	[91]
$3_{21} \leftarrow 3_{12}$	83258225.69(200)	-1.71	83258242(60)	-16.31	[91]
$2_{20} \leftarrow 2_{11}$	83319483.33(200)	-1.51	83319459(60)	24.33	[91]
$1_{11} \leftarrow 0_{00}$	83502180.44(200)	-0.65	83502181.08(90)	-0.64	[90]
$2_{02} \leftarrow 1_{11}$	83591104.21(200)	0.29	83591103.84(15)	0.37	[90]
$3_{12} \leftarrow 3_{03}$	83611788.86(200)	-0.24	83611817(60)	-28.14	[91]
$2_{21} \leftarrow 2_{12}$	84014925.65(200)	0.21	84014926.35(78)	-0.69	[90]

Table 4.1: (cont.)

$2_{12} \leftarrow 1_{01}$	84265643.03(200)	0.26	84265642.81(12)	0.22	[90]
$3_{30} \leftarrow 3_{21}$	84277356.85(200)	0.65	–		
$4_{13} \leftarrow 4_{04}$	84400948.70(223)	0.19	84400990(60)	-41.30	[91]
$3_{22} \leftarrow 3_{13}$	84414871.55(200)	-0.33	84414901(60)	-29.45	[91]
$3_{03} \leftarrow 2_{12}$	84558339.15(200)	0.71	84558381(60)	-41.85	[91]
$3_{13} \leftarrow 2_{02}$	84926063.15(200)	0.41	84926047(60)	16.22	[91]
$4_{04} \leftarrow 3_{13}$	85412859.83(200)	-3.15	85412850(60)	9.83	[91]
$4_{14} \leftarrow 3_{03}$	85573374.36(200)	0.32	85573389(60)	-14.64	[91]
$2_{21} \leftarrow 1_{10}$	85581954.85(200)	0.57	85581954.15(18)	0.70	[90]
$2_{20} \leftarrow 1_{11}$	85930971.82(200)	0.12	85930971.78(15)	0.04	[90]
$5_{05} \leftarrow 4_{14}$	86188742.45(200)	1.36	86188773(60)	-30.55	[91]
$5_{15} \leftarrow 4_{04}$	86248883.92(200)	-1.79	86248911(60)	-27.08	[91]
$3_{22} \leftarrow 2_{11}$	86323498.28(200)	-0.31	86323499(60)	-0.72	[91]
$3_{21} \leftarrow 2_{12}$	87486539.30(346)	-0.83	87486574(60)	-34.70	[91]
$3_{30} \leftarrow 2_{21}$	87781239.63(200)	-0.31	87781240(60)	-0.37	[91]

4.4 Discussion

The new rovibrational transition frequencies can predict pure rotational transitions either through CDs or a fit to an effective Hamiltonian. CDs in the ground state are determined by taking the difference between two transitions that share a final state. These CDs can then be combined with known rotational frequencies to predict unobserved transitions. Our new measurements lead to 20 ground state CDs, which are presented in Table 4.2 along with CDs determined by Jusko *et al.* [90] and comparisons to spacings calculated from THz data [86, 87, 89]. Ten unobserved rotational transitions can be predicted from these CDs with uncertainties of approximately 3 MHz, which are presented in Table 4.4. In cases where a rotational transition could be calculated in different ways, multiple frequencies are listed.

Frequencies predicted by CDs are trustworthy in that they do not rely on fitting to a model Hamiltonian, whereas predictions from molecular constants will depend on how extensive the initial data set was, and what particular parameters were included in the fit. However, molecular constants can predict a larger set of transitions and can have improved uncertainties when even a limited number of transitions measured with microwave accuracy are included in the fit. Therefore, we also included a fit to an effective Hamiltonian and used the frequencies predicted by CDs as a validation.

D_2H^+ is a "floppy" molecule, which leads to large centrifugal distortion at excited rotational levels. This causes parameters in a Watson-type Hamiltonian to have oscillatory behavior, especially for the series of N_z^{2n} coefficients. This leads to poor convergence unless a large number of terms are included. For this reason we opted to use an Euler Hamiltonian using the method developed by Pickett *et al.* [93], which Jusko *et al.* [86] successfully used to fit the

Table 4.2: List of ground state CDs derived from measurements of the ν_1 fundamental band with comparison to values calculated from THz measurements. The 1σ uncertainties are given in parentheses.

CD	Frequency (MHz)	From THz data (MHz)	Diff. (MHz)
$3_{03} - 2_{21}$	507721.46(283)	–	–
$4_{04} - 3_{22}$	971977.39(283)	–	–
$2_{12} - 1_{10}$	1567027.58(283)	–	–
$2_{12} - 1_{10}$	1567029.20(283)	–	–
$2_{12} - 1_{10}$	1567027.80(80) [90]	–	–
$3_{13} - 2_{11}$	1908626.74(283)	1908626.71(10) [86, 87]	0.03
$2_{20} - 2_{02}$	2408713.89(283)	2408714.74(30) [86, 89]	-0.85
$2_{11} - 1_{11}$	2611488.49(283)	2611486.86(10) [86, 87]	1.63
$3_{21} - 3_{03}$	2996159.22(283)	2996161.11(14) [87]	-1.89
$3_{22} - 2_{20}$	3035437.99(283)	–	–
$2_{02} - 0_{00}$	3049427.81(283)	3049429.43(10) [86, 87]	-1.62
$2_{02} - 0_{00}$	3049427.49(76) [90]	3049429.43(10) [86, 87]	-1.94
$3_{21} - 2_{21}$	3503882.79(283)	–	–
$3_{12} - 2_{12}$	4228313.61(283)	–	–
$2_{21} - 1_{01}$	4324385.16(283)	–	–
$2_{21} - 1_{01}$	4324386.57(283)	–	–
$3_{13} - 1_{11}$	4520114.84(283)	4520113.57(14) [87]	1.27
$3_{03} - 1_{01}$	4832108.03(283)	–	–
$3_{22} - 2_{02}$	5444149.16(283)	–	–
$3_{22} - 2_{02}$	5444151.88(283)	–	–
$4_{13} - 3_{13}$	5966479.44(291)	–	–
$4_{04} - 2_{02}$	6431252.66(283)	–	–

ground state of D_2H^+. It has also been successfully used to fit other molecules which have large centrifugal distortion such as D_2O and CH_2 to high rotational levels [97, 98]. The standard angular momentum operators N_i^2 and $\mathbf{N}^2$ are replaced by the Euler functions N_i^{2*} and $\mathbf{N}^{2*}$ which are defined as:

$$N_i^{2*} = \frac{N_i^2}{1 + aN_z^2 + b(\mathbf{N}^2 - N_z^2)} \tag{4.1}$$

$$\mathbf{N}^{2*} = \frac{\mathbf{N}^2 - N_z^2}{1 + aN_z^2 + b(\mathbf{N}^2 - N_z^2)} \tag{4.2}$$

where the coefficients a and b are chosen transformation parameters. The subscript i represents the rotational axis a, b, or c, and in the I^r representation $a = z$, $b = x$, and $c = y$. The Euler expansion of the Hamiltonian is then:

$$\mathcal{H}_{rot}^E = \sum_{i,j} X_{ij}(N_a^{2*})^i(\mathbf{N}^{2*})^j + \sum_{i,j} \frac{1}{2} Y_{ij}\{(N_a^{2*})^i(\mathbf{N}^{2*})^j, N_b^{2*} - N_c^{2*}\} \tag{4.3}$$

where $\{,\}$ is the anticommutator and X_{ij} and Y_{ij} are the diagonal and off-diagonal spectroscopic parameters, respectively. It should be noted that the a and b transformation parameters in Equations 4.1 and 4.2 need not be the same for different vibrational states, or for the diagonal and off-diagonal parts of the expansion [93].

For our two-state fit, the ground state parameters were initially held to the values determined by Jusko *et al.* [86], and initial guesses for a and b parameters for $\nu_1 = 1$ were calculated from the Watson-type parameters [93]. First, CDs from rovibrational studies of the ν_2 and ν_3 fundamental bands and pure rotational data were included [86, 87, 89, 92, 99]. Then, rovibrational transitions from this work and Lubic & Amano [91] were added sequentially in order of increasing final K_a. When the root-mean-square (RMS) error grew large, the term which was found to reduce the error the most was included. When the transitions $4_{23} \leftarrow 4_{14}$ and $6_{06} \leftarrow 5_{15}$ were included, we found that their assignments by Lubic & Amano [91] needed to be switched. Once all transitions were added, 12 total rotational parameters were used in the $\nu_1 = 1$ excited state. Then, all X_{ij} and Y_{ij} parameters for both states were allowed to float and the transformation parameters a_X, b_X, a_Y, and b_Y were then adjusted one at a time to obtain the best fit result. Overall, 25 parameters were used to fit 49 states from 121 transitions and CDs. A reduced RMS error of 0.72 was obtained for all data and 0.71 for our data alone. The files from the fit are included in the supplementary material. In comparison, a fit to a traditional two-state Watson-type Hamiltonian with 25 parameters resulted in a reduced RMS error of 2.2, and required an additional 8 parameters to reach a reduced RMS error below 1 of 0.60.

Table 4.3: Spectroscopic parameters from a two-state fit of the ν_1 fundamental band to an Euler Hamiltonian. All values are in MHz. The 1σ uncertainties are given in parentheses.

Parameter	Ground	$\nu_1 = 1$
$a_x \times 10^3$	2.5	1.2
$b_x \times 10^3$	0.48	0.37
$a_y \times 10^3$	7.3	12
$b_y \times 10^3$	1.5	1.6
ν_0	–	82052461.194(114)
X_{01}	1085199.67(51)	1062119.165(237)
X_{10}	523757.577(120)	518150.388(130)
X_{20}	1893.84(65)	413.410(82)
X_{11}	1409.674(115)	719.762(176)
X_{02}	79.0888(254)	9.7879(293)
X_{30}	4.239(126)	1.0551(84)
X_{21}	0.8502(139)	-1.4353(233)
X_{12}	2.0071(153)	1.3862(147)
X_{03}	0.05467(54)	0.08293(94)
Y_{00}	65984.820(134)	65141.907(162)
Y_{10}	28.279(114)	311.871(121)
Y_{01}	33.9370(74)	36.0269(66)

The resulting parameters from the fit are in Table 4.3, and the residuals from the fit are listed in Table 4.1. Calculated rotational transition frequencies are listed in Table 4.4 along with comparisons to predictions from CDs and the Cologne Database for Molecular Spectroscopy (CDMS) [75]. Predictions from the newly determined molecular constants have improved upon the uncertainties of previous values by at least a factor of 2, and in most cases by a factor of ~10. The two transitions which fall within the coverage of the SOFIA GREAT instrument, $3_{22} \leftarrow 3_{13}$ and

$4_{13} \leftarrow 4_{04}$, had their uncertainties improved from 15.4 and 5.07 MHz to 1.42 and 1.45 MHz respectively.

Table 4.4: Comparison of predicted rotational frequencies from CDs, molecular constants, and CDMS [75]. All values are in MHz. The 1σ uncertainties are given in parentheses.

Transition	From CDs	From molecular constants	From CDMS
$2_{21} \leftarrow 2_{12}$	2065696.17(400)	2065694.313(420)	2065690.46(283)
–	2065696.91(294)	–	–
–	2065698.32(294)	–	–
$3_{12} \leftarrow 2_{21}$	2162617.23(283)	2162618.406(809)	2162613.00(714)
–	2162617.45(283)	–	–
$2_{12} \leftarrow 1_{01}$	2258688.24(80)	2258689.259(273)	2258688.25(77)
$3_{22} \leftarrow 3_{13}{}^{a}$	2496859.31(283)	2496859.93(142)	2496835.9(154)
–	2496862.03(283)	–	–
–	2496862.89(285)	–	–
$4_{13} \leftarrow 4_{04}{}^{a}$	2497642.74(400)	2497653.56(145)	2497660.95(507)
$3_{03} \leftarrow 2_{12}$	2573417.84(283)	2573416.977(578)	2573407.69(506)
–	2573419.78(294)	–	–
$4_{04} \leftarrow 3_{13}$	3468836.70(283)	3468833.17(165)	3468810.1(192)
$4_{13} \leftarrow 3_{22}$	3469616.55(401)	3469626.80(213)	3469635.2(277)
$2_{21} \leftarrow 1_{10}$	3632724.71(283)	3632723.129(416)	3632718.28(303)
–	3632726.12(283)	–	–
$3_{22} \leftarrow 2_{11}$	4405486.02(283)	4405486.65(142)	4405462.6(154)
–	4405488.74(283)	–	–
–	4405489.59(284)	–	–
$3_{21} \leftarrow 2_{12}$	5569578.95(283)	5569578.058(590)	5569568.80(507)

a: Within coverage of the SOFIA GREAT instrument

The Euler-type parameters can be converted to Watson-type parameters for comparison by expanding the denominators of N_i^{2*} and $\mathbf{N}^{2*}$ in Equation 5.4 and gathering terms of the correct order [93]. The converted Watson parameters are presented in Table 4.5 and compared to previous works. The ground state molecular constants are generally in agreement with those determined by Yu *et al.*. Many parameters do disagree outside of their respective uncertainties, however molecular constants for "floppy" molecules can vary widly depending on the particular line list and parameter set used [86]. A comparison of the converted $\nu_1 = 1$ parameters with those from Lubic & Amano [91] was omitted, since the switched assignment of the $4_{23} \leftarrow 4_{14}$ and $6_{06} \leftarrow 5_{15}$ transitions caused their parameters to be significantly off.

4.5 Conclusion

In this work, we have greatly expanded the number of rovibrational transitions of D_2H^+ measured with MHz-level uncertainty from 10 to 37 using the sub-Doppler technique NICE-OHVMS. These values have been used to predict unobserved rotational transitions using molecular constants from a fit to an Euler Hamiltonian. The uncertainties of the predicted frequencies, including two within the coverage of the SOFIA GREAT instrument, have been significantly

Table 4.5: Watson-type molecular constants calculated from the Euler-type parameters determined by the fit for the ground state, with comparison to Watson-type parameters determined by Yu *et al.* [87]

Parameter	Converted	Previous work [87]
A	1085199.67(51)	1085216.75(175)
B	655727.217(293)	655655.2(24)
C	391787.937(292)	391847.91(168)
Δ_K	570.85(66)	569.29(182)
Δ_{JK}	75.99(13)	89.01(135)
Δ_J	172.315(25)	169.580(183)
δ_K	388.37(11)	354.91(92)
δ_J	65.0402(74)	63.509(79)
Φ_K	5.36(13)	4.98(40)
Φ_{KJ}	-5.371(37)	-3.82(43)
Φ_{JK}	1.465(16)	1.367(167)
Φ_J	0.0993(6)	0.0[a]

a: Held to 0.0

reduced to approximately 1.5 MHz. These frequencies will also assist in laboratory searches for unobserved THz transitions. Moreover, these new measurements will act as valuable benchmarks for *ab intio* calculations which go beyond the Born–Oppenheimer approximation.

4.6 Supplemental material: NICE-OHVMS asymmetry

4.6.1 Issues with NICE-OHVMS line center determination

In the past, measurements of transition frequencies using Noise Immune Cavity Enhanced Optical Heterodyne Velocity Modulation Spectroscopy (NICE-OHVMS) were reported after measuring the transition at least five times. The sub-Doppler feature of each scan was fit using a global least-squares fitting routine, with the line center being a shared parameter [42]. The line center was reported as the average, and the uncertainty as the standard deviation of all the scans, which usually was on the order of 1 MHz.

When a survey of D_2H^+ transitions using NICE-OHVMS was being conducted, it became clear that transitions which had previously been measured by Jusko *et al.*[90] disagreed well outside of our claimed uncertainty. Table 4.6 shows a comparison of the eight transitions, where 5 disagreed outside of 1 σ. The RMS error was 2.3 MHz. This meant that either the values reported by Jusko *et al.* or measured by NICE-OHVMS were underestimating the uncertainty. Comparing with pure rotational data made it clear that the issue was with NICE-OHVMS. The redundant CDs for the $2_{11} - 1_{11}$ transition measured by NICE-OHVMS disagreed by 5.5 MHz. They also disagreed by 2 and -3.5 MHz with the CD calculated from highly accurate rotational data. Additionally, measuring on different days caused the average frequency to change by up to 5.9 MHz, although it never disagreed with the values of Jusko *et al.* by more than 4 MHz.

Table 4.6: D_2H^+ transitions measured using NICE-OHVMS in comparison to the values reported by Jusko *et al.*[90] All values are in MHz, and uncertainties are given in parentheses in units of the least significant digit.

Transition	Frequency (Jusko *et al.*)	Frequency (NICE-OHVMS)	Difference
$1_{01} \leftarrow 1_{10}$	81349548.38(15)	81349548.84(77)	0.46
$1_{10} \leftarrow 1_{01}$	82713780.40(15)	82713782.18(60)	1.78
$1_{11} \leftarrow 0_{00}$	83502181.08(9)	83502181.04(11)	-0.04
$2_{02} \leftarrow 1_{11}$	83591103.84(15)	83591103.66(34)	-0.19
$2_{21} \leftarrow 2_{12}$	84014926.35(78)	84014922.34(138)	-4.01
$2_{12} \leftarrow 1_{01}$	84265642.81(12)	84265646.00(203)	3.19
$2_{21} \leftarrow 1_{10}$	85581954.15(18)	85581957.22(37)	3.08
$2_{20} \leftarrow 1_{11}$	85930971.78(15)	85930973.38(15)	1.61

First, the calibration with the frequency comb was investigated. After ensuring that the software and the frequency comb electronics were operating as designed, standard transitions of methane were measured. The new measurements

agreed with the past measurements with an RMS error of 160 kHz[96], while the disagreements with NICE-OHVMS measurements persisted.

4.6.2 Asymmetry

After some troubleshooting, it was found that small changes in the alignment to the external cavity introduced an asymmetry to the Doppler profile. Figure 4.3 shows a scan of the $R(1,1)^u$ transition of the ν_2 fundamental band of H_3^+. This scan was taken with a heterodyne frequency of 231 MHz, and all Lamb dips are resolved. When an adjustment was made to the fine adjustment screw on the lens which focuses the light into the cavity, it caused the Doppler profile to become asymmetric, as shown in Fig. 4.4. This was an extreme case where the alignment was far from optimized.

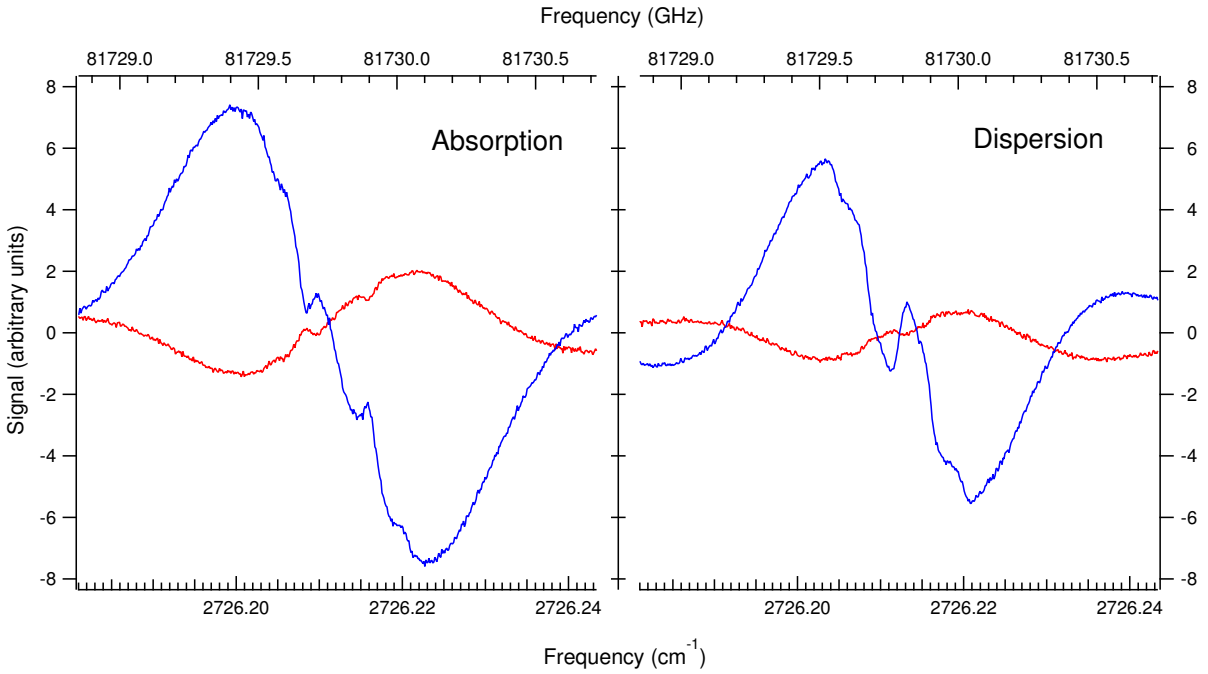

Figure 4.3: A NICE-OHVMS scan of the $R(1,1)^u$ transition, where the aligment produced a symmetric Doppler profile. The left and right plot represent the absorption and dispersion channels respectively. The Lamb dips are resolved because of the 231 MHz heterodyne frequency.

In order to investigate the effect the injection angle had on the line center determination, the mirror just before the cavity was placed in a piezo driven mirror mount. It was found that changes on the order of 1 mrad could cause MHz-level shifts in the frequency determination. Figure 4.5 shows how a change in 0.7 mrad changed the measured line center by 5 MHz. Figure 4.6 shows the change in offset as the angle was slewed from -1.5–2.5 mrad, where the disagreement reached 6 MHz. Also, the difference "turned around" at 1.5 mrad in this case. Generally, the change of ~4 MHz/mrad was consistent.

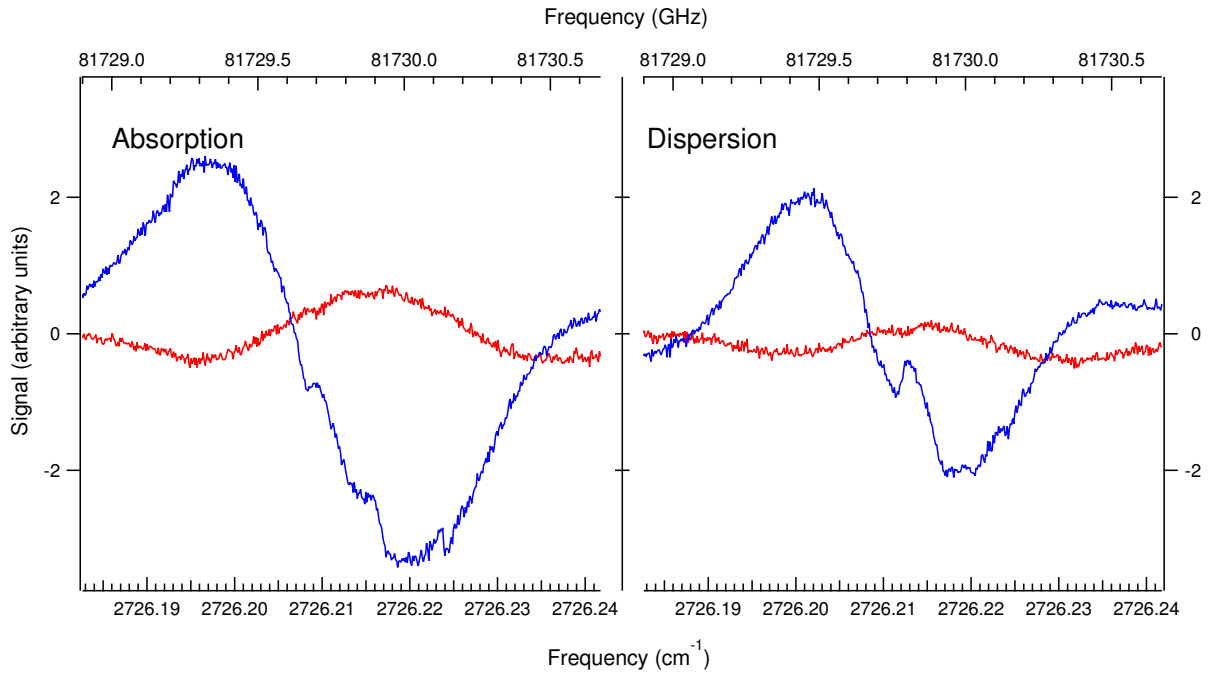

Figure 4.4: A NICE-OHVMS scan of the $R(1,1)^u$ transition taken just after the scan in Fig. 4.3 after a small adjustment was applied to the lens just before the cavity. The left and right plot represent the absorption and dispersion channels respectively.

The source of the asymmetry was investigated by removing layers of modulation and seeing its effect on the asymmetry. Frequency modulation (FM) spectroscopy can suffer from residual amplitude modulation (RAM). To test whether RAM was the cause of the asymmetry, the heterodyne modulation was removed, and the light transmitted from the cavity was demodulated only at twice the velocity modulation frequency. This is known as cavity-enhanced velocity modulation spectroscopy (CE-VMS)[38]. It was found that changing the injection angle still changed the asymmetry. Taking NICE-OHVMS scans directly after CE-VMS scans showed that they shared the same asymmetry. Figures 4.7 and 4.8 show the optimized alignment for NICE-OHVMS and CE-VMS respectively, while Figs. 4.9 and 4.10 show scans after the alignment was changed. This is evidence that the asymmetry is not caused by some form of RAM. If the asymmetry were caused by RAM, the CE-VMS scans should appear symmetric.

To see if the effect was somehow related to velocity modulation, Noise-Immune Cavity-Enhanced Optical Heterodyne Molecular Spectroscopy (NICE-OHMS) scans were taken of methane. A beam chopper was placed after the cavity, and the output of the detector was first demodulated at the heterodyne frequency and then at the chopper frequency. The asymmetry did change with the alignment, but the effect was much more apparent in the absorption channels than in the dispersion channels. Figures 4.11 and 4.12 show NICE-OHMS scans of methane before and after the alignment was detuned. This does demonstrate that the asymmetry is not due to velocity modulation, however it is not obvious why the dispersion channel is less affected by the change in alignment for NICE-OHMS scans, while

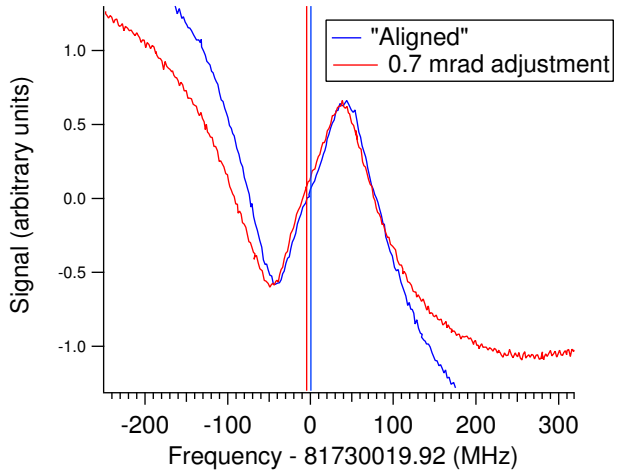

Figure 4.5: Two NICE-OHVMS scans of the $R(1,1)^u$ transition taken before (blue)and after (red) a 0.7 mrad change in the injection angle of the light into the cavity. The vertical lines represent the line center frequency as determined by the least-squares fits of each scan. The line center measured by Jusko *et al.* [90] is subtracted from the frequency axis for comparison.

the effect is strong in NICE-OHVMS dispersion channels as seen in Figs. 4.4 and 4.9.

4.6.3 Tentative solutions

The NICE-OHMS scans of methane allow for a quantitative way to measure the extent of the asymmetry. This is because NICE-OHMS line shapes are understood in comparison to NICE-OHVMS line shapes. The Doppler profiles of scans were fit to determine the extent of the asymmetry, and the alignment to the cavity was adjusted until the NICE-OHMS lineshape was symmetric. Then, NICE-OHVMS scans were taken with the same alignment, which was found to greatly reduce the offsets. For D_2H^+ measurements, this was done before each transition, and all transitions were measured on two separate days. This reduced the differences with the measurements by Jusko *et al.* from an RMS error of 2.3 MHz to 560 kHz [100].

However, this approach was not taken with measurements of H_3^+, due to a large number of transitions in the ν_2 fundamental band and the $2\nu_2^2 \leftarrow \nu_2$ hot band having already been measured, and the significant amount of time required to properly optimize the alignment. Therefore, scans were taken with the alignment to the cavity being optimized for the best coupling efficiency, and small changes being made if a qualitative asymmetry was observed. Because the disagreements with the D_2H^+ measurements by Jusko *et al.* had an RMS error of 2.3 MHz, a conservative estimate of 4 MHz was taken for the uncertainty of NICE-OHVMS measurements.

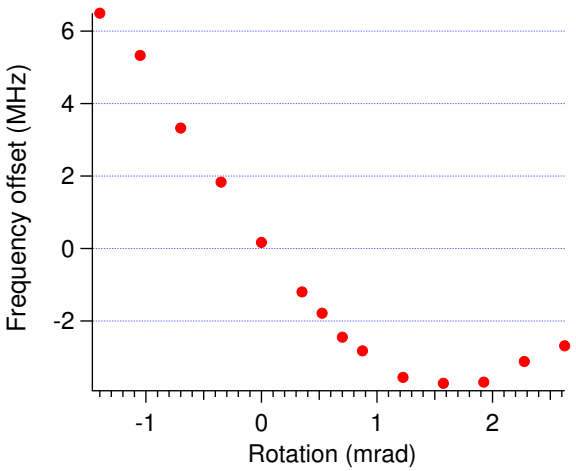

Figure 4.6: The difference between the measured line center of $R(1,1)^u$ and the value reported by Jusko *et al.*[90] as the injection angle was changed using a piezo driven mirror mount.

4.6.4 Conclusion

An asymmetry was found in NICE-OHVMS measurements, which caused shifts in the line center frequency of several MHz. The asymmetry was found to be dependent on the injection angle of the beam into the cavity, and in extreme cases could change the line center frequency by 6 MHz. The asymmetry in the Doppler profile occurred regardless of modulation scheme, appearing in CE-VMS and NICE-OHMS scans. Ultimately, a tentative solution was found where NICE-OHMS scans were used to set the alignment before taking NICE-OHVMS measurements which was used for our investigation of D_2H^+ [100]. However, for $H_3{}^+$, due to the scale of the survey this strategy was not taken, and an estimated uncertainty of 4 MHz was used to capture the error caused by the asymmetry.

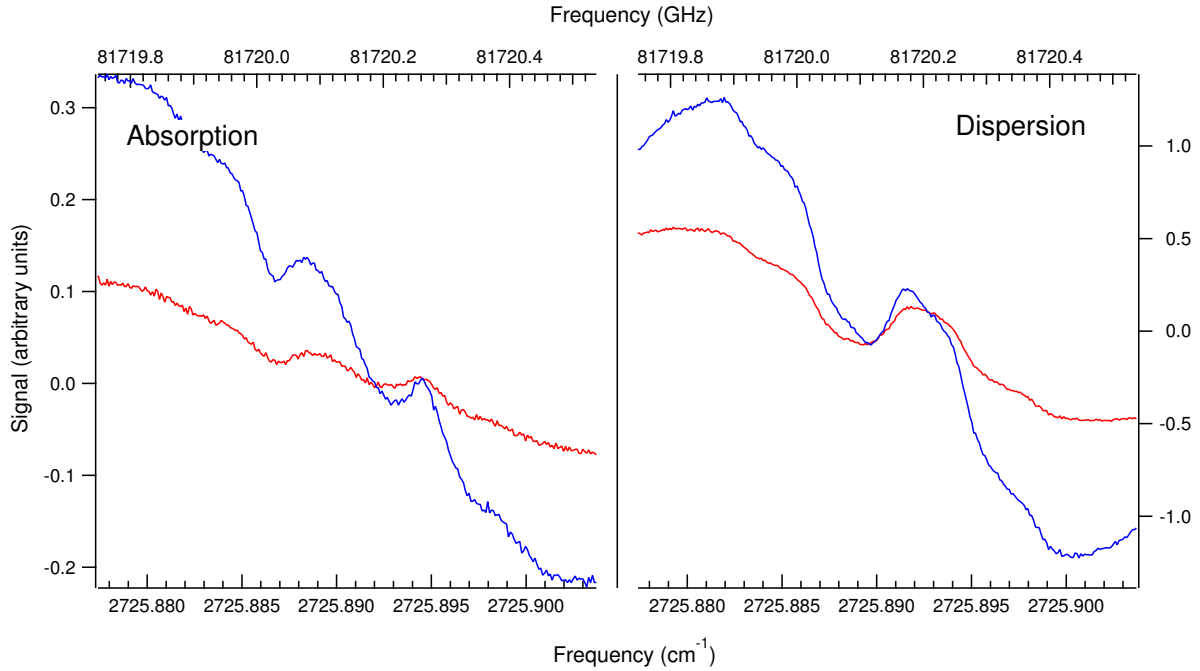

Figure 4.7: A NICE-OHVMS scan of $R(1,1)^u$ when the alignment to the cavity was optimized to produce a symmetric Doppler profile.

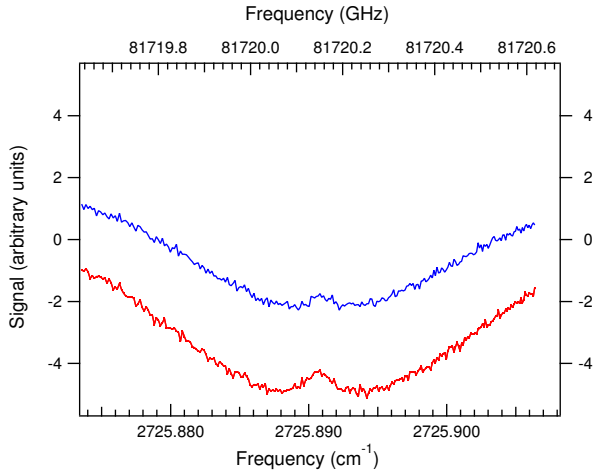

Figure 4.8: A CE-VMS scan taken with the same alignment as the scan in Fig. 4.7. The red and blue traces represent the in-phase and quadrature components of the velocity modulation signal. The feature in the center is the Lamb dip.

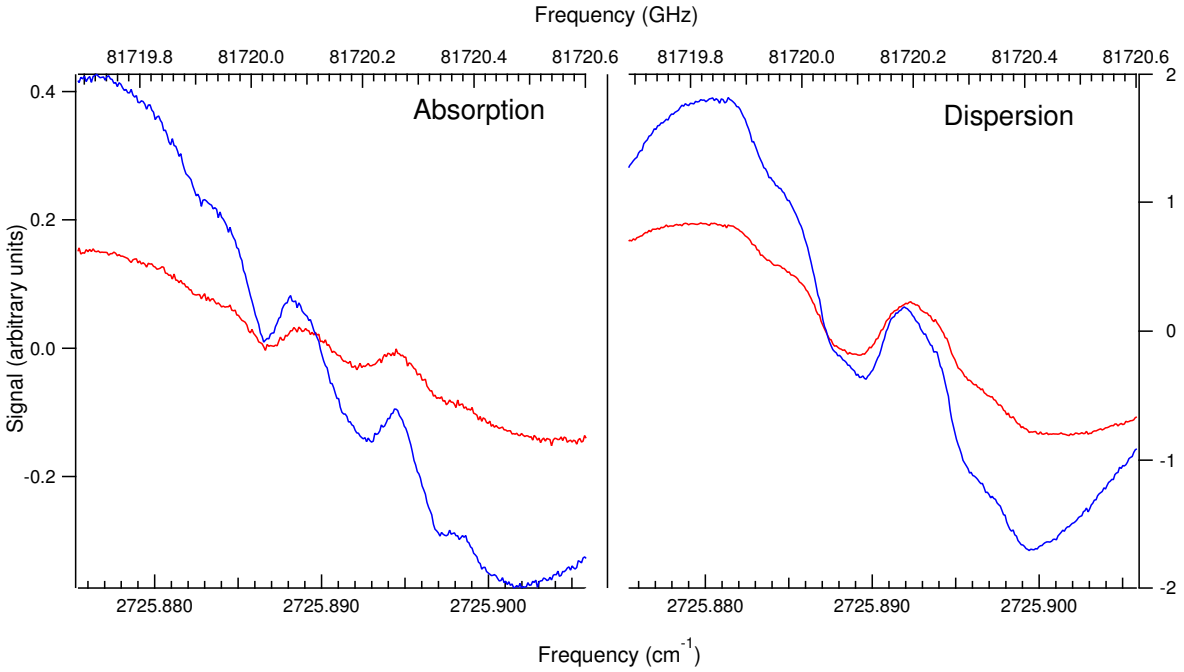

Figure 4.9: A NICE-OHVMS scan of $R(1,1)^u$ after the alignment to the cavity was changed, which caused the Doppler profile to appear asymmetric.

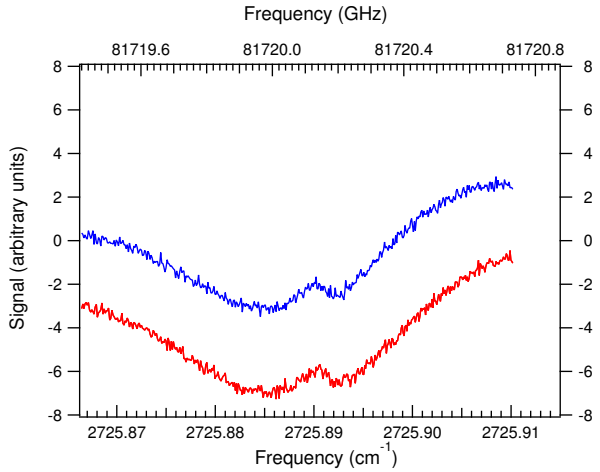

Figure 4.10: A CE-VMS scan taken with the same alignment as the scan in Fig. 4.9 after the alignment was detuned. The red and blue traces represent the in-phase and quadrature components of the velocity modulation signal. The feature in the center is the Lamb dip.

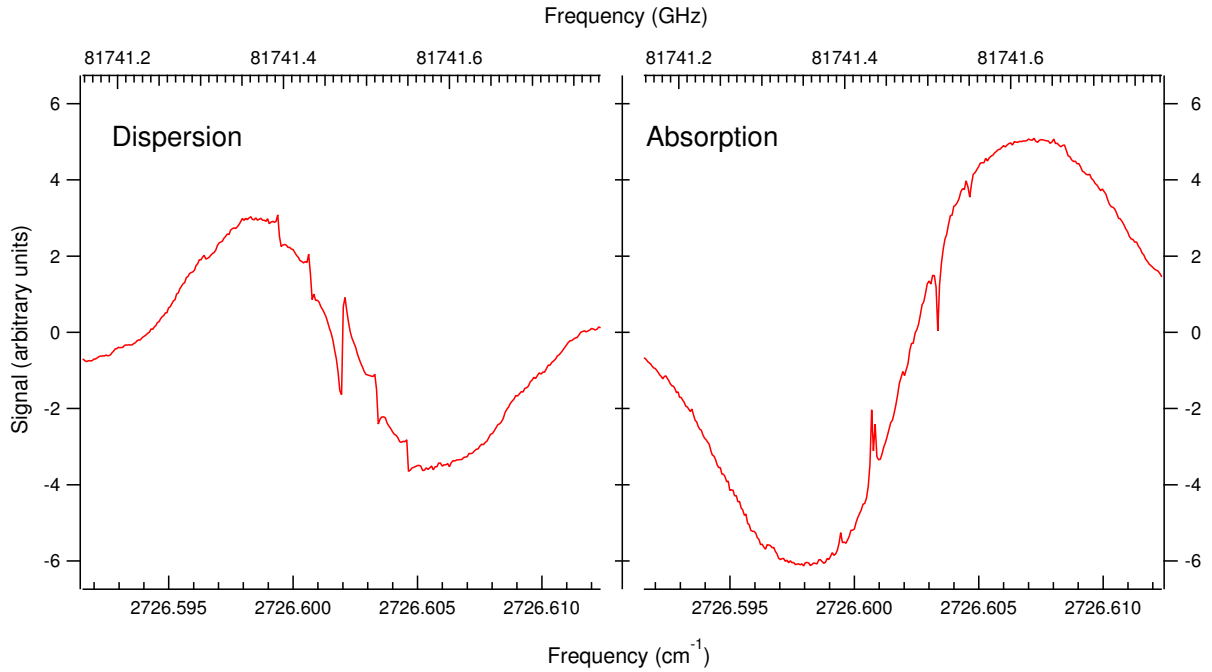

Figure 4.11: A NICE-OHMS scan of the $P(7)A_2$ transition in the $\nu_2 + \nu_4$ combination band of methane, with the left and right plots showing dispersion and absorption respectively. The sharp features are the fully resolved Lamb dips.

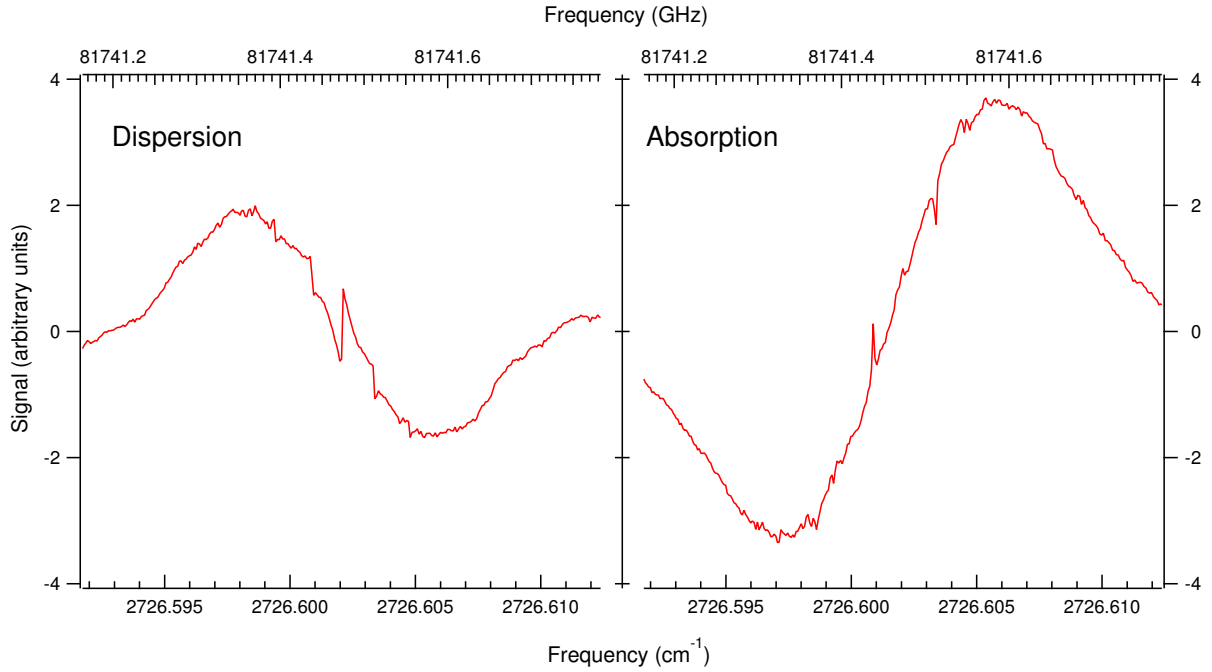

Figure 4.12: A NICE-OHMS scan of the $P(7)A_2$ transition in the $\nu_2 + \nu_4$ combination band of methane after the alignment was changed by 1 mrad, with the left and right plots showing dispersion and absorption respectively. The Doppler profile in the absorption channel clearly shifted relative to the Lamb dips, whereas it is only slight affected in the dispersion channel.

Chapter 5

Highly-accurate experimentally determined energy levels of H_3^+

5.1 Introduction

H_3^+ is the simplest polyatomic molecule, and calculations of its rovibrational energy levels have been a useful test for state-of-the-art *ab initio* calculations [25]. For astronomers, observations of H_3^+ have allowed for probing conditions in a range of environments, from molecular clouds to the ionospheres of gas giants [101, 102]. Astronomers and theoreticians rely on laboratory measurements for accurate and precise transition frequencies, while experimentalists have relied on theorists to understand and assign the spectrum of H_3^+ as they have moved to higher vibrational quanta.

Highly accurate calculations of H_3^+ must go beyond the clamped nuclei Born–Oppenheimer approximation. The accurate potential energy surface (PES) calculated by Pavanello *et al.* [35] included corrections for relativistic effects and adiabatic coupling between electronic and nuclear motion, and was able to reproduce rovibrational transitions to within 0.2 cm^{-1}, even for states beyond the barrier to linearity ($\sim$10,000 cm^{-1}). The accuracy of H_3^+ calculations is currently limited by treatment of the nonadiabatic coupling, where electronic motion changes the effective mass of the nuclei [5]. To account for this, Diniz *et al.* [29] calculated coordinate-dependent masses, and were able to achieve agreement with high-precision rovibrational transition frequencies on the order of 0.001 cm^{-1}, after empirical scaling of the mass surfaces. As the accuracy of *ab initio* calculations continue to approach experimental uncertainties, there is a need for improved experimentally determined transition frequencies and absolute energy levels.

A few spectroscopic techniques have demonstrated the ability to measure rovibrational transition frequencies of H_3^+ with MHz-level uncertainty, all of which have relied on optical frequency combs (OFCs) for accurate frequency calibration. Laser-induced reaction spectroscopy on ions in a 4 K ion trap was able to measure low-lying rotational transitions of H_3^+ and isotopologues with sub-MHz uncertainties [90]. However, due to the low temperature of the trap and the large rotational constants of H_3^+, only the lowest rotational states were accessible. Other experiments have utilized sub-Doppler spectroscopy of H_3^+ ions generated in normal glow discharges, which can access higher rotational

states. The first published sub-Doppler measurements of H_3^+ used a double-pass pump-probe scheme with wavelength modulation on an extended negative glow discharge cell [49]. However, issues with the frequency calibration were later found [42, 90], which were resolved with a new double pass spectrometer which used an intensity modulated pump and a new scheme for frequency calibration [103]. In the past, we have demonstrated that the technique Noise Immune Cavity Enhanced Optical Heterodyne Velocity Modulation Spectroscopy (NICE-OHVMS) [78] is capable of determining rovibrational transitions frequencies with MHz-level uncertainty [42, 43]. To date, 24 rovibrational transitions frequencies have been measured with MHz-level uncertainty or better, all of which are from the $\nu_2 \leftarrow 0$ band and all but four of which are from the *R* branch.

In this study, NICE-OHVMS has been used to measure rovibrational transitions of H_3^+ in a positive column discharge cell, and an OFC was used for accurate frequency calibration. We have measured 36 transitions in the $\nu_2 \leftarrow 0$ band spanning the *P*, *Q*, and *R* branches, 16 transitions in the $2\nu_2^2 \leftarrow \nu_2$ hot band, and 7 transitions in the $2\nu_2^2 \leftarrow 0$ overtone band of H_3^+ improving the uncertainties to ~4 MHz, which for most transitions is an improvement by a factor of 40 or more. These new data have been used to significantly improve predictions of forbidden rotational transitions and to determine absolute rovibrational energy levels.

5.1.1 H_3^+ structure and notation

H_3^+ is an oblate symmetric top, and has the equilibrium geometry of an equilateral triangle belonging to the point group D_{3h}. It has two vibrational modes: the infrared inactive symmetric stretch ν_1 and the doubly degenerate infrared active stretch ν_2. The degeneracy of the ν_2 mode leads to vibrational angular momentum *l*, and the standard notation for a vibrational state with vibrational quanta v_2 in the ν_2 mode is $v_2\nu_2^l$. For vibrationally excited states, *k* and *l* are not good quantum numbers due to strong *l*-resonance, and it is useful to define the better quantum number $g \equiv k - l$ [104]. In cases were two combinations of *k* and *l* can produce the same $G = |g|$, the states are labeled with a *u* or *l* for the upper and lower levels respectively. Similar to standard symmetric top labeling, the notation for rotational states is $(J, G)u|l$. Additional information on the notation can be found in the comprehensive evaluation on H_3^+ spectroscopy by Lindsay & McCall [105].

The three protons are identical Fermions, and must adhere to the Pauli Principle. Under the three-particle permutation-inversion group S_3^*, the total wavefunction must be antisymmetric upon the exchange of two nuclei (12), and symmetric upon a cyclic (123) permutation. For *ortho* states, where the nuclear spin $I = 3/2$, only states with $G = 3n$ have the Pauli allowed symmetry, where *n* is an integer ≥ 0. The remaining *para* states with $I = 1/2$ will follow $G = 3n \pm 1$. Additionally, in the ground vibrational state, when $G = 0$ only states with odd *J* values have the proper symmetry. Notably, the lowest rotational state (0,0) does not exist.

Important selection rules to consider for rovibrational transitions are $\Delta J = 0, \pm 1$, Δk is odd, and $\Delta g = 3n$. Because

Δk must be odd, it follows that hot band and fundamental band transitions with $\Delta l = \pm 1$ must follow $\Delta g = 0$, and overtone transitions with $\Delta l = \pm 2$ follow $\Delta g = \pm 3$. Transitions are labeled with the usual P, Q, and R to indicate ΔJ, with the inclusion of a superscript t or n if $\Delta g = +3$ or -3 respectively and a final superscript u or l when it is necessary to indicate the final state.

These selection rules can be used to our advantage for experimentally determining energy levels in the ground state. If two transitions share a final state, the difference in their frequencies provides an energy level spacing between their initial states, which is called a ground state combination difference (CD). The selection rule $\Delta G = 0$ for fundamental band transitions means they can only connect states with the same G value. Connecting different G ladders is possible using $2\nu_2^2 \leftarrow 0$ overtone transitions with the selection rule $\Delta G = \pm 3$. Then, fundamental and hot band transitions can be used to complete the CD by connecting the ground to the $2\nu_2^2$ state.

Because transitions between *ortho* and *para* states are strictly forbidden, CDs are only able to determine energy levels relative to the lowest *ortho* or *para* levels. Connecting the *ortho* and *para* manifolds, and determining energy levels relative to the forbidden $(0, 0)$ state requires additional analysis using an effective Hamiltonian or empirically scaled numerical calculations.

5.2 Experimental

5.2.1 Spectrometer

All data were collected with our NICE-OHVMS spectrometer, and the configuration for measurements from 3.2 to 3.9 μm has been described in detail previously [42]. In brief, tunable 1064 nm light from a distributed feedback laser is passed through a fiber coupled proton-exchanged electro-optic modulator (EOM). The EOM phase modulates the light at both the heterodyne detection frequency to generate a frequency modulation (FM) triplet, and at ~4 MHz for Pound-Drever-Hall locking [40]. The light is then amplified by a ytterbium doped fiber amplifier to 10 W. This is sent to a commercial optical parametric oscillator (OPO, Aculight Argos 2400 SF) which generates the signal and idler beams with up to 1 W of power. For the fundamental and hot band measurements, the idler beam from a signal-resonant C (3.2–3.9 μm) or D (3.9–4.6 μm) module was used for spectroscopy. For the overtone transitions, the signal beam from an idler-resonant A module (1.96–2.01 μm) was used.

There are a number of challenges for using an OPO with a periodically poled lithium niobate (PPLN) crystal at wavelengths longer than 3.9 μm. As the wavelength increases from 3.9 μm, multi-phonon absorption causes the output power to decline, with only ~30 mW of idler available near 4.51 μm. Also, at idler wavelengths of 3.96–4.03 μm, PPLN has an OH absorption at the signal wavelength which leads to significantly higher threshold power. There are also a number of "blind spots" with little-to-no output power due to absorption from H_2O or CO_2 within the OPO

cavity. In regions where the threshold power was too high, the mode-selecting etalon within the OPO cavity was removed. This significantly reduced the threshold power, but also led to problems with multi-mode behavior and rapid frequency drift. Single-mode operation was achieved by setting the pump power just above threshold, which also resulted in less idler power. The frequency was stabilized by locking the signal beam to an OFC, which is described in Section 5.2.2.

The beam which was used for spectroscopy was locked onto resonance of an external cavity (finesse 100-400) using a PDH locking scheme. In order to generate the PDH error signal, the light reflected off the first cavity mirror was picked off with a CaF_2 window and focused onto a fast mid-IR detector. Slow PDH corrections (< 100 Hz) were sent to piezoelectric transducers (PZTs) on both of the cavity mirrors, and fast corrections were sent to a fiber coupled acousto-optic modulator (AOM) on the seed laser. Brewster-plate spoilers [56, 106] were set before and after the cavity to average out signals from parasitic etalons. The heterodyne frequency was set to 77 or 231 MHz to be an integer multiple of the free spectral range (FSR) of the cavity (77 MHz) in order to couple the FM sidebands into cavity modes on either side of the carrier.

A triple-jacketed liquid-cooled discharge cell, "Black Widow" [95], was used to generate the H_3^+ ions, and was placed within the external cavity. The ends of the cell were sealed with Brewster windows, and a mixture of H_2 and He gas was flowed through the cell. Electrodes at the ends of the cell were driven by a 2 kV sinusoidal voltage to generate a discharge. The discharge was cooled by flowing chilled water or liquid nitrogen around the jacket surrounding the cell, depending on the desired rotational temperature.

The detector scheme depended on the wavelength of light being used for spectroscopy. For measurements from 3.2–4.6 μm, fast thermoelectrically-cooled HgCdTe detectors (Boston Electronics Vigo PVI-4TE-6) were used for generating the PDH error signal and measuring the light transmitted from the cavity. To avoid saturating the detector, a fraction of the light was picked off, further attenuated to < 500 μW, and focused onto the detector. For measurements near 2 μm, fast liquid nitrogen cooled InSb detectors (Kolmar, KISDP-0.1) were used instead.

The output of the transmission detector was sent to a pair of radio frequency (RF) mixers set 90° out of phase with each other in order to recover the in-phase and quadrature components of the heterodyne signal. The mixer outputs were low-pass filtered and sent to a pair of dual-channel lock-in amplifiers referenced to twice the velocity modulation frequency to recover the in-phase and quadrature components of the velocity modulation signal. This results in four total channels of detection. The lock-in amplifiers were set to a 300 ms time constant, and scans were taken by stepping the frequency in 3 MHz steps and holding for 2 s at each point.

5.2.2 Frequency calibration

A GPS referenced OFC (Menlo Systems FC-1500, 100 MHz repetition rate) which spans 1050–2100 nm was used to accurately calibrate the frequency while spectra were recorded. For wavelengths between 3.2 and 4.6 μm, the idler frequency was determined indirectly by taking the difference between the pump and signal frequencies. The pump and signal beats were generated using free-space optics, as described previously [42]. The integer number of comb modes between the pump and signal was determined by taking a rough measurement of the idler frequency with a mid-IR wavemeter (Bristol 621). The beat generated between the signal and the nearest comb tooth was locked at 20 MHz using a phase-locked loop (PLL) with corrections sent to a PZT on the OPO signal cavity, which also acted to stabilize the idler frequency. Because the pump frequency steps in 3 MHz increments during a scan, a double-pass AOM was used to keep the beat frequency within a 30 MHz bandpass using a feed-forward scheme [96]. When the AOM reached the end of its diffraction efficiency, it shifted the pump 100 MHz to the next comb tooth. A delay of 2 s after each step ensured the frequency counters had time to measure both beat frequencies. The frequency of the idler can then be determined by

$$\nu_{idler} = \Delta n \times f_{RR} \pm f_{pb} \mp f_{sb} - 2 \times f_{AOM}$$

where Δn is the number of comb modes between the pump and signal frequencies, f_{RR} is the repetition rate of the comb, f_{pb} and f_{sb} are the frequencies of the pump and signal beats respectively, and f_{AOM} is the frequency applied to the AOM. The sign of the beat notes represents whether the frequency of the beam was above or below the nearest comb tooth, which can be determined by applying a small step to the repetition rate of the OFC and observing the change in the beat frequency. The accuracy of the frequency calibration was found to be ~160 kHz using standard transitions of methane [96].

For measurements at 2 μm, the wavelength of the signal beam was within the coverage of the OFC and could be measured directly and calculated using the equation

$$\nu_{signal} = n \times f_{RR} \pm f_{CEO} \pm f_{sb}$$

where n is the integer mode number of the nearest comb tooth and f_{CEO} is the carrier envelope offset (CEO) frequency. The mode number of the nearest comb tooth can be determined by measuring the signal with the wavemeter. The CEO was locked at 20 MHz using a PLL.

To generate the beat between the signal and the comb, they were overlapped using fiber optics, which offers superior spatial overlap compared to free space methods. First, a fraction of the signal beam was picked off before the external cavity and fiber coupled. The polarization of the light was controlled using a fiber optic paddle polarizer (Thorlabs FPC024) before being sent into one input of a 2×2 fiber optic coupler (Thorlabs TW2000R5A2B). The

OFC was also fiber coupled and sent into the other input of the 2×2 coupler. One of the outputs of the coupler was sent into free space, reflected off of a grating, and focused onto a fast liquid nitrogen cooled InSb detector (Kolmar KISDP-0.5). The beat frequency was locked at 20 MHz using a frequency-to-voltage converter with corrections sent to the PZT driver that controlled the seed laser of the OPO. The frequency of the signal beam was scanned in 3 MHz steps by stepping the repetition rate of the comb, which allowed for $\sim$ 400 MHz of scanning.

5.3 Results

An example of a NICE-OHVMS scan of the $Q(1,0)$ transition in the $\nu_2 \leftarrow 0$ fundamental band is shown in Fig. 5.1. The left and right plots represent the in-phase and quadrature components of the heterodyne signal, and the red and blue traces represent the in-phase and quadrature components of the velocity modulation signal. The Doppler profile appears as a wide derivative lineshape, while the narrower feature at the center is a set of Lamb dips separated by half integer multiples of the heterodyne frequency. Due to the large homogeneous broadening of approximately 80 MHz, these features overlapped when the heterodyne frequency was 77 MHz, and were resolved when it was 231 MHz [106].

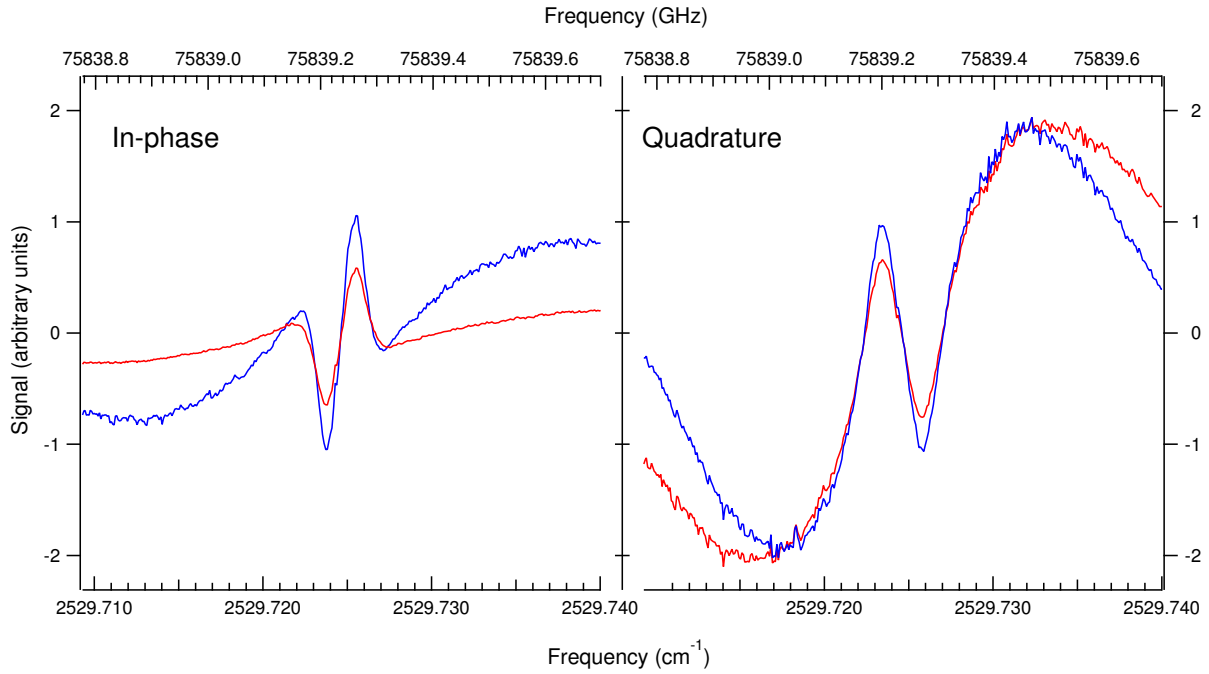

Figure 5.1: A NICE-OHVMS scan of the $Q(1,0)$ transition in the $\nu_2 \leftarrow 0$ fundamental band, recorded with a 77 MHz heterodyne modulation frequency. The left and right plots represent the in-phase and quadrature components of the heterodyne signal, while the red and blue traces represent the in-phase and quadrature components of the velocity modulation signal.

The line center is determined by fitting the sub-Doppler feature in all four channels simultaneously using a global

least-squares fitting routine, where the center frequency is a shared parameter [42]. In the past, the uncertainty was reported as the standard deviation of a set of at least five scans, and ranged from 700 kHz to 2.5 MHz with most having an uncertainty of ~1 MHz [42, 43].

When NICE-OHVMS was used to investigate the $\nu_1 \leftarrow 0$ fundamental band of D_2H^+, problems with the line center determination were discovered [100]. Disagreements with the values reported by Jusko *et al.* [90] were as large as 4 MHz, well outside of our measured uncertainty. Remeasuring transitions on multiple days revealed day-to-day changes of up to 6 MHz, although the disagreement with the previous values never exceeded 4 MHz. To verify that the OFC calibration was not causing the issue, standard methane transitions were measured using sub-Doppler spectroscopy, and the line center frequencies agreed within 200 kHz with an root-mean-square (RMS) error of 160 kHz [96].

The origin of the disagreement was determined to be asymmetry in the Doppler profile, where one lobe was diminished relative to the other, giving the appearance that the Lamb dip was sitting nearer to the top or bottom of the profile. The asymmetry along with the offset would change with small adjustments to the alignment of the beam to the cavity. The cause of this effect has not yet been determined, but the error was contained within 4 MHz when the alignment to the cavity was optimized. The disagreement with values reported by Jusko *et al.* were distributed with an RMS error of 2.3 MHz, and an estimated uncertainty of 4 MHz has been applied for our $H_3{}^+$ NICE-OHVMS measurements to give a conservative estimate of the error which encapsulates the asymmetry offsets. Examples showing this effect are available in the supplementary material, Section 4.6.

5.3.1 Fundamental band $\nu_2 \leftarrow 0$

To measure transitions in the ν_2 fundamental band, $H_3{}^+$ ions were generated in a discharge of 300 mTorr of H_2, with either liquid nitrogen or chilled water flowing through the jacket surrounding the cell. Liquid nitrogen cooling was used for transitions starting from states with $J < 3$, which resulted in a rotational temperature of ~ 170 K. Transitions that started from higher rotational levels were observed with chilled water as the coolant, which gave a rotational temperature of ~450 K.

Previously, NICE-OHVMS was used to measure 20 R branch transitions spanning $R(1,1)^l$ to $R(4,1)^u$ [42, 43]. Changes to the instrument allowed this to be expanded. The introduction of Brewster-plate spoilers significantly improved the sensitivity of the instrument by avoiding parasitic etalons, allowing for weaker transitions to be measured [106]. Also, a set of high reflectivity mirrors which covered 3.7–4.77 μm (Layertec, 99% reflectivity) were acquired, which extended the coverage of the instrument to include Q and P branch transitions. Additionally, locking the signal frequency to the comb enabled stable operation of the D module (3.9–4.6 μm), and made measurements of many Q branch and P branch transitions possible.

With these changes, an additional 36 transitions have been measured from $P(4,4)$ to $R(5,5)^u$ with an estimated uncertainty of 4 MHz. It should be noted that 18 of the transitions from the current study were presented at the International Symposium on Molecular Spectroscopy [107, 108]. The new transition frequencies are listed in Table 5.1 with comparisons to the most recent literature values. The measurements by McKellar *et al.* [109] using absorption Fourier transform infrared spectroscopy (FTIR) compare extraordinarily well, with an average offset of 3 MHz, and an RMS error of only 20 MHz, despite their claimed uncertainties of 150 MHz. Values measured using emission FTIR [110] compare less favorably, with an average offset of 75 MHz and an RMS error of 170 MHz, which is larger than the estimated uncertainty of 120 MHz. Emission spectroscopy of H_3^+ is difficult in this region, due to interference from H_2 electronic transitions, which could explain the understated uncertainty. Additionally, the 5 transitions from the literature which were measured with MHz-level uncertainty [103] agreed with the new values within our estimated uncertainty of 4 MHz.

Table 5.1: Newly measured rovibrational transitions in the $\nu_2 \leftarrow 0$ fundamental band with comparison to previous values. All units are in MHz, and uncertainties are given in parentheses in units of the least significant digit.

Transition	Frequency (this work)	Frequency (previous)	Difference	Reference
$P(4,4)$	66477520.51(400)	66477509(120)	11.51	[110]
$P(4,3)$	66497862.13(400)	66497835(120)	27.13	[110]
$P(4,1)^u$	66850568.90(400)	66850570(120)	-1.10	[110]
$P(3,3)$	68920206.83(400)	68920188(120)	18.83	[110]
$Q(6,5)^l$	73348494.68(400)	73348182(120)	312.68	[110]
$Q(6,3)^l$	73530562.21(400)	73530636(120)	-73.79	[110]
$Q(6,4)^l$	73551669.33(400)	73551321(120)	347.33	[110]
$P(1,1)$	73667685.63(400)	73667701(150)	-15.37	[109]
$Q(5,4)^l$	73975496.87(400)	73975378(90)	118.87	[111]
$Q(5,0)$	74106385.57(400)	74106387(90)	-1.43	[111]
$Q(5,1)^l$	74118638.05(400)	74118439(120)	199.05	[110]
$Q(5,3)^l$	74134186.83(400)	74134058(120)	128.83	[110]
$Q(5,2)^l$	74145994.94(400)	74145810(120)	185.94	[110]
$Q(4,3)^l$	74545148.64(400)	74545163(150)	-14.36	[109]
$Q(4,2)^l$	74700633.00(400)	74700636(150)	-3.00	[109]
$Q(4,1)^l$	74724417.54(400)	74724379(150)	38.54	[109]
$Q(3,0)$	75220254.22(400)	75220266(150)	-11.78	[109]
$Q(2,1)^l$	75494063.34(400)	75494067(150)	-3.66	[109]
$Q(1,0)$	75839225.87(400)	75839225.64(85)	0.23	[103]
$Q(1,1)$	76309753.78(400)	76309754.18(93)	-0.04	[103]
$Q(2,1)^u$	76536660.62(400)	76536655(150)	5.62	[109]
$Q(2,2)$	76586944.78(400)	76586946.28(158)	-1.50	[103]
$Q(3,3)$	76791725.52(400)	76791723.23(255)	2.29	[103]
$Q(3,2)^u$	76879298.48(400)	76879318(150)	-19.52	[109]

Table 5.1: (cont.)

$Q(4,4)$	76965382.04(400)	76965358(150)	24.04	[109]
$Q(3,1)^u$	77007873.75(400)	77007929(150)	-55.25	[109]
$Q(4,3)^u$	77186330.11(400)	77186335(150)	-4.89	[109]
$Q(5,4)^u$	77381778.20(400)	77381950(120)	-171.80	[110]
$Q(4,2)^u$	77433718.54(400)	77433721(300)	-2.46	[111]
$Q(6,5)^u$	77555627.17(400)	77555859(120)	-231.83	[110]
$Q(5,3)^u$	77750464.98(400)	77749975(120)	490.98	[110]
$R(3,1)^l$	84881719.64(400)	84881438(300)	281.64	[112]
$R(4,2)^l$	86696143.62(400)	86695992(300)	152.47	[112]
$R(5,3)^l$	88425484.47(400)	88425434(120)	50.11	[110]
$R(5,4)^l$	88593414.11(400)	88593288(300)	125.71	[113]
$R(4,4)^u$	90180929.71(400)	90180933.3(39)	-3.59	[103]

5.3.2 Hot band $2\nu_2^2 \leftarrow \nu_2$

To observe transitions in the $2\nu_2^2 \leftarrow \nu_2$ hot band, the H_3^+ ions needed to be vibrationally hot yet rotationally cold. The addition of a He buffer gas, which has a higher ionization energy than H_2, increases the electron temperature of the plasma which results in a higher vibrational temperature [111]. For all of our hot band measurements, the gas mixture was 300 mTorr of H_2 and 2 Torr of He. Liquid nitrogen was flowed around the cell, which was able to rotationally cool the ions without significantly affecting the vibrational temperature. This is because collisions are more efficient at rotational cooling than vibrational cooling [114].

Higher pressures will increase the power required to saturate a transition and observe a Lamb dip, and we found that we were still able to saturate transitions with the 2 Torr of He buffer gas. An example of the $R(2,0)$ hot band transition is shown in Fig. 5.2. To our knowledge, these are the first sub-Doppler measurements of H_3^+ hot band transitions. It appears that the He buffer gas may have also led to higher translational temperature, causing larger Doppler broadening.

Overall, 16 transitions in the $2\nu_2^2 \leftarrow \nu_2$ band from $Q(2,0)$ to $R(4,0)$ were measured with an estimated uncertainty of 4 MHz. The results can be found in Table 5.2 with comparisons to measurements by Bawendi *et al.* [111] The previous values are systematically lower by an average of 97 MHz, and all but 6 are outside of one standard deviation. This is consistent with other studies from the Oka group during this time, when scanning rates were too rapid for the lock-in time constants. This led to "line dragging" that resulted in a systematic offset in the reported frequencies. For this reason, Lindsay & McCall recommended an increased uncertainty of 300 MHz for this and other works from the Oka group during this time [105].

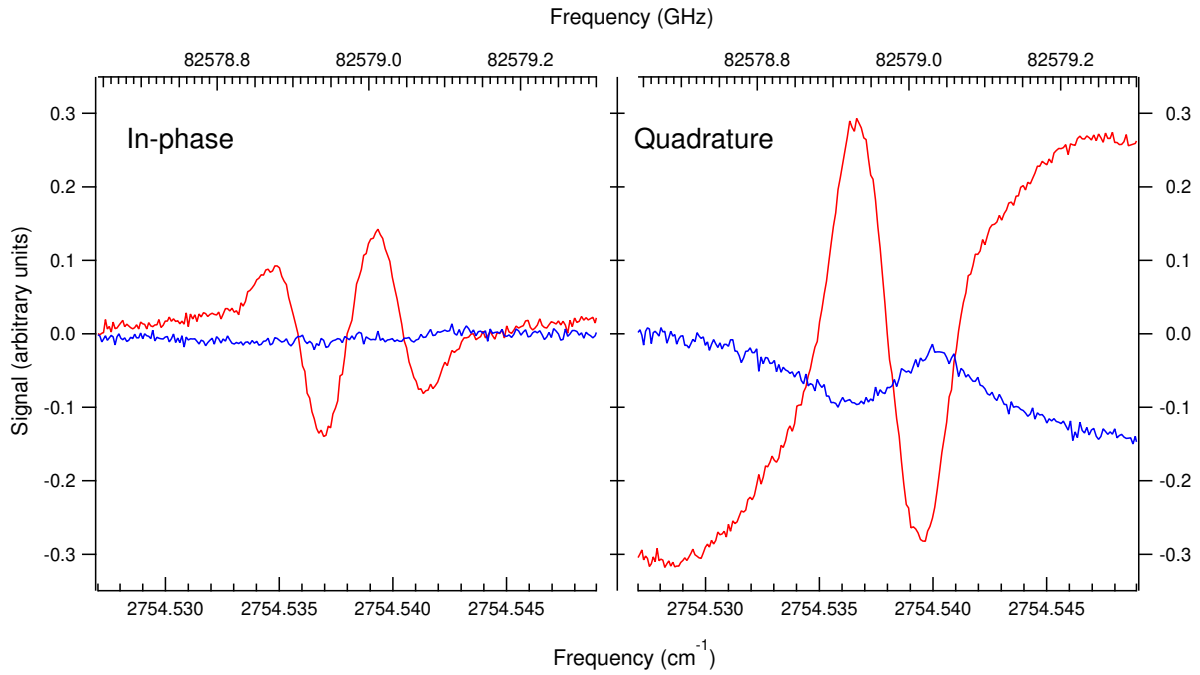

Figure 5.2: A NICE-OHVMS scan of the $R(2,0)$ transition in the $2\nu_2^2 \leftarrow \nu_2$ hot band. The left and right plots represent the in-phase and quadrature components of the heterodyne signal, while the red and blue traces represent the in-phase and quadrature components of the velocity modulation signal.

5.3.3 Overtone band $2\nu_2^2 \leftarrow 0$

To extend the coverage of the NICE-OHVMS instrument to include the $2\nu_2^2 \leftarrow 0$ overtone band at 2 μm, high reflectivity mirrors which covered 1.92–2.18 μm (Layertec, 99.0% reflectivity) were used for the NICE-OHVMS cavity. The H_3^+ ions were generated in a discharge of 300 mTorr of H_2, and because all the desired transitions were from low lying rotational states only liquid nitrogen cooling was used.

The large anharmonicity of the H_3^+ potential leads to strong overtone transitions, and the $2\nu_2^2 \leftarrow 0$ band is no exception with 1/7 the intensity of the $\nu_2 \leftarrow 0$ fundamental band [115]. Despite the transition dipole moment being smaller, it was found that the instrument was still capable of saturating transitions to generate strong sub-Doppler features, and an example of the ${}^tR(1,1)$ overtone transition is shown in Fig. 5.3. To our knowledge, these are the first sub-Doppler measurements of H_3^+ overtone transitions.

Ultimately, 7 transitions were measured from ${}^tR(1,1)$ to ${}^tR(1,0)$. We were unable to measure transitions below ${}^tR(1,1)$ since the OPO would become unstable when tuned below 4950 cm^{-1}. The results can be found in Table 5.3 with comparison to measurements by Xu *et al.* [116] The previous values displayed an even larger systematic offset than the hot band measurements by Bawendi *et al.* [111], with all transitions being outside of their estimated uncertainty of 150 MHz with an average offset of 225 MHz. It is likely that the measurements suffered from the same systematic error due to scanning too rapidly.

Table 5.2: Newly measured rovibrational transitions in the $2\nu_2^2 \leftarrow \nu_2$ hot band with comparison to previous values. All units are in MHz, and the uncertainties are given in parentheses in units of the least significant digit.

Transition	Frequency (This work)	Frequency (Previous) [111]	Difference
$Q(2,0)$	74170467.71(400)	74170273(90)	194.71
$Q(1,2)$	76130916.62(400)	76130826(90)	90.62
$Q(3,0)$	76190405.61(400)	76190245(90)	160.61
$Q(2,2)$	76221275.11(400)	76221243(90)	32.11
$Q(3,3)$	76575377.32(400)	76575268(90)	109.32
$Q(3,4)$	77338982.2(400)	77338899(90)	83.20
$Q(4,4)$	77441047.83(400)	77441039(90)	8.83
$Q(5,5)$	77924189.92(400)	77924094(90)	95.92
$R(0,1)$	78062541.75(400)	78062448(90)	93.75
$Q(5,0)$	79405938.33(400)	79405789(90)	149.33
$R(1,0)$	80051627.89(400)	80051601(90)	26.89
$R(1,2)$	81491483.59(400)	81491445(90)	38.59
$R(2,0)$	82578971.99(400)	82578882(90)	89.99
$R(3,4)$	87928908.53(400)	87928768(90)	140.53
$R(4,0)$	88283855.00(400)	88283722(90)	133.00

Table 5.3: Newly measured rovibrational transitions in the $2\nu_2^2 \leftarrow 0$ overtone band with comparison to previous values. All units are in MHz, and the uncertainties are given in parentheses in units of the least significant digit.

Transition	Frequency (This work)	Frequency (Previous) [116]	Difference
${}^tR(1,1)$	148945367.99(400)	148945047(150)	320.99
${}^nP(3,3)$	149043829.87(400)	149043649(150)	180.87
${}^nQ(1,1)$	150600776.89(400)	150600621(150)	155.89
${}^nQ(2,1)$	150767979.04(400)	150767756(150)	223.04
${}^tR(3,2)$	150869192.88(400)	150868966(150)	226.88
${}^tR(2,1)$	151751556.50(400)	151751405(150)	151.50
${}^tR(1,0)$	152721132.07(400)	152720814(150)	318.07

5.4 Discussion

5.4.1 Combination differences and forbidden rotational transitions

CDs are able to determine energy level spacings in the ground state and predict forbidden rotational transitions without the need of an effective Hamiltonian. The improved transition frequencies were used to calculate 21 CDs in the ground state with uncertainties of 4–8 MHz, which are presented in Table 5.4. The transitions which contributed to each CD are provided in the supplementary material. Different CDs which calculated the same energy level spacing were used to assess the estimated uncertainty of the NICE-OHVMS measurements. The differences between redundant CDs had an RMS error of 4.7 MHz, and a reduced RMS of 0.72. This confirms that the estimated uncertainty of 4 MHz was

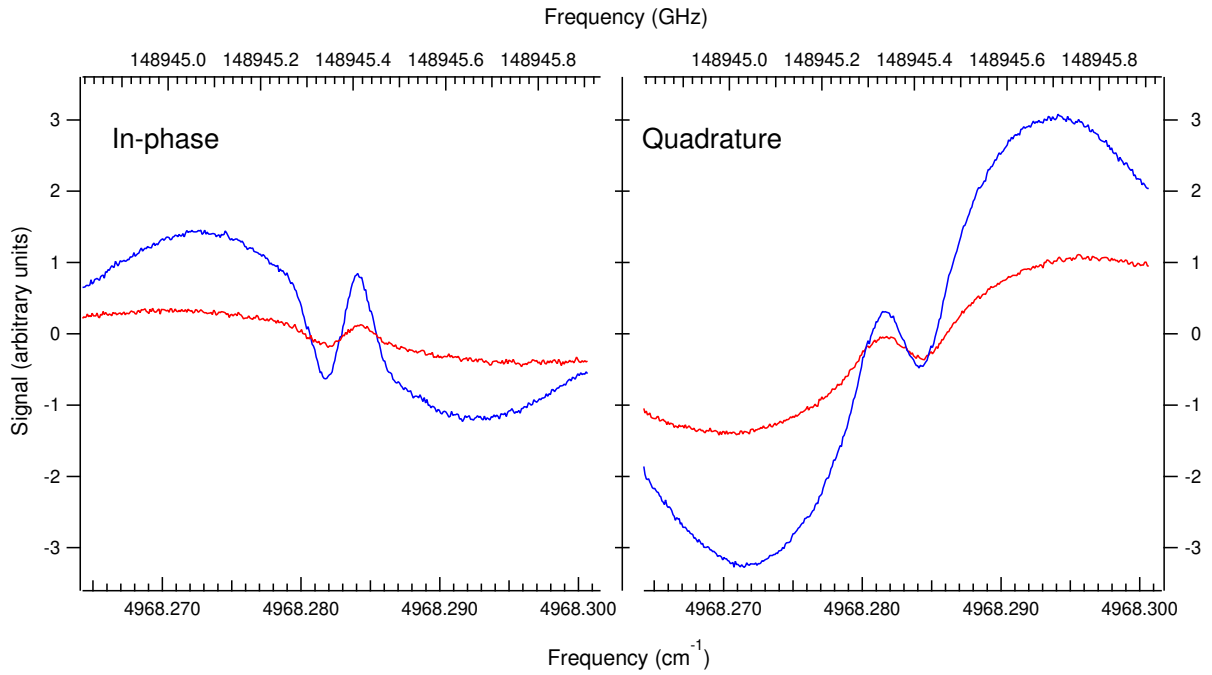

Figure 5.3: A NICE-OHVMS scan of the ${}^{t}R(1,1)$ transition in the $2\nu_2^2 \leftarrow 0$ overtone band. The left and right plots represent the in-phase and quadrature components of the heterodyne signal, while the red and blue traces represent the in-phase and quadrature components of the velocity modulation signal.

sufficient, if not slightly overstated.

Calculating CDs between states with different G values is essential for predicting forbidden rotational transitions, and for calculating absolute energy levels. This was made possible by the new measurements of overtone transitions which have the selection rule $\Delta G = \pm 3$, coupled with measurements of fundamental band and hot band transitions. With the new measurements, five CDs were calculated connecting states with $G = 0$ and 3, and $G = 1, 2$, and 4, which had uncertainties of 5.7–9.0 MHz. These values are also presented in Table 5.4.

Table 5.4: Ground state CDs of H_3^+. All frequencies are in MHz, the uncertainties are given in parentheses in units of the least significant digit.

$(J', G') - (J'', G'')$	Energy difference
$\Delta G = 0$	
$(2,1) - (1,1)$	5193359.2(40)
	5193359.5(40)
$(3,1) - (2,1)$	7716972.8(56)
$(3,2) - (2,2)$	7756239.3(40)
$(4,1) - (3,1)$	10157302.1(56)
	10157304.8(56)
$(4,2) - (3,2)$	10206479.3(41)
	10206485.8(56)
$(4,3) - (3,3)$	10293857.6(41)

Table 5.4: (cont.)

	10293861.1(47)
	10293864.3(40)
$(5,2)-(4,2)$	12550148.7(56)
$(5,3)-(4,3)$	12644246.8(56)
	12644254.4(41)
$(5,4)-(4,4)$	12799151.5(56)
	12799151.6(56)
$(3,0)-(1,0)$	12888688.8(69)
$(6,3)-(5,3)$	14894922.2(56)
$(6,4)-(5,4)$	15041744.8(56)
$(6,5)-(5,5)$	15272463.6(40)
$(5,0)-(3,0)$	22615726.8(80)
$\Delta G = 3$	
$(2,1)-(2,2)$	2040242.2(59)
$(2,2)-(1,1)$	3153122.9(81)
$(3,3)-(1,0)$	6847023.5(57)
$(4,4)-(2,1)$	7935052.8(69)
	7935052.5(89)

The forbidden rotational transitions of H_3^+ have been predicted to be relatively strong, with transition dipole moments as large as 38 mD due to the significant centrifugal distortion [117]. The selection rules are $\Delta J = 0, \pm 1$ and $\Delta k = \pm 3$, and the transition frequencies can be predicted directly from CDs. Redundant CDs were averaged, and in cases where two different sets of CDs could calculate the same transition the average was used. This resulted in 16 predicted forbidden rotational transitions, with uncertainties of 7–14 MHz, which are presented in Table 6.3.

Of particular interest to astronomers is the $(4,4) \leftarrow (3,1)$ forbidden rotational transition, which is well positioned to be an astrophysical maser [118], The lifetime of the $(4,4)$ state is on the order of 10 years, while the $(3,1)$ state has a lifetime of less than 8 hrs [117]. This would lead to population inversion in an environment where there is sufficient excitation and limited collisional quenching. These conditions could be met in the molecular gas surrounding an active galactic nucleus or possibly in the ionospheres of gas giants. The uncertainty of the predicted frequency has been improved from 280 to 10 MHz, which greatly improves the prospects for an astronomical detection.

5.4.2 Absolute energy levels

For direct comparison with *ab initio* calculations, it is desirable to have experimentally determined energy levels relative to the $(0,0)$ state. However, this cannot be accomplished using CDs alone. The $(0,0)$ state is forbidden by the Pauli principle, and transitions between *ortho* and *para* states are strictly forbidden. Absolute energy levels can be

Table 5.5: Predictions for forbidden rotational transitions of H_3^+, calculated from combination differences. All frequencies are in MHz, the uncertainty is given in parentheses in units of the least significant digit.

$(J', G') - (J'', G'')$	Freq.
$(4,4) \leftarrow (3,1)$	218079.7(89)
$(3,1) \leftarrow (3,2)$	2000972.8(103)
$(2,1) \leftarrow (2,2)$	2040239.3(76)
$(5,4) \leftarrow (4,1)$	2859927.8(120)
$(2,2) \leftarrow (1,1)$	3153120.0(95)
$(4,3) \leftarrow (3,0)$	4252195.7(72)
$(3,2) \leftarrow (2,1)$	5716000.0(93)
$(5,0) \leftarrow (5,3)$	5719280.4(137)
$(3,0) \leftarrow (3,3)$	6041665.2(90)
$(4,2) \leftarrow (3,1)$	8205509.7(115)
$(6,3) \leftarrow (5,0)$	9175641.9(131)
$(3,1) \leftarrow (2,2)$	9757212.1(95)
$(4,1) \leftarrow (4,4)$	9939223.8(106)
$(5,2) \leftarrow (4,1)$	10598354.9(140)
$(4,1) \leftarrow (3,2)$	12158276.3(118)
$(5,0) \leftarrow (4,3)$	18363531.0(128)

determined by fitting the ground state to an effective Hamiltonian, and then using the molecular constants to calculate the energy of the $(1,0)$ and $(1,1)$ states. Then, CDs can be used to fill out the rest of the energy levels. This strategy was used by Lindsay & McCall in their comprehensive review of H_3^+ spectroscopy [105], and their values for the $(1,0)$ and $(1,1)$ energy levels have been used since [36, 119].

Determining molecular constants

H_3^+ suffers from severe centrifugal distortion, which makes fitting CDs or energy levels to an effective Hamiltonian challenging. Our goal for determining the molecular constants of H_3^+ was to calculate the energies of the $(1,0)$ and $(1,1)$ states, and it was therefore of critical importance that the parameters were well behaved at low J. Including higher order parameters can lead to issues with the lower order terms, especially when there is lack of accurate experimental data at higher rotational levels. To avoid this, limited data sets were used for fitting in order to avoid the need of higher order parameters.

Fits were performed on energy levels relative to $(1,0)$ and $(1,1)$ for *ortho* and *para* states respectively. CDs from Table 5.4 were used to calculate lower rotational states, and in cases where there were redundant CDs the average

value was used. The standard Watson-type effective Hamiltonian for an oblate symmetric top is the following:

$$\begin{aligned}\mathcal{H}_{rot}^{W} &= B\mathbf{J}^2 + (C-B)J_z^2 - D_J\mathbf{J}^4 - D_{JK}\mathbf{J}^2J_z^2 - D_KJ_z^4 + H_J\mathbf{J}^6 \\ &+ H_{JK}\mathbf{J}^4J_z^2 + H_{KJ}\mathbf{J}^2J_z^4 + H_KJ_z^6 + h_3(J_+^6 + J_-^6)\end{aligned} \tag{5.1}$$

where h_3 is the off-diagonal sextic splitting term for symmetric tops with 3-fold symmetry, which is nonzero for $G = 3$ states. Least squares fits were performed using the software SPFIT developed by Pickett [80]. States were added incrementally in the order of increasing J, and when the RMS error grew too large the parameter which improved the fit the most was included. The highest order parameters included in the fit were the sextic centrifugal distortion constants. If a state required octic or higher order terms, either the state was omitted or the relative energy from Lindsay & McCall was used instead, which had a larger uncertainty. Ultimately, 20 rotational states up to $(J, G) = (6, 5)$ were fit using 10 parameters with a reduced RMS error of 1.11. Of the 18 relative energy levels, 10 were from the accurate newly determined values. The resulting molecular constants and predictions for the $(1, 0)$ and $(1, 1)$ energy levels relative to $(0, 0)$ can be found in Table 5.6.

There are some concerns with using a Watson-type Hamiltonian to fit a "floppy" molecule. They require relatively large centrifugal distortion constants, and successive terms in the expansion change sign, which can lead to truncation errors and poor convergence behavior. An alternative approach is to use an Euler-type Hamiltonian, which was derived by Pickett [93]. Euler's transformation can convert an alternating series to a series where all the terms have the same sign, while still converging to the same value. For an oblate symmetric top, this can be accomplished by replacing the angular momentum operators J_z^2 and $\mathbf{J}^2$ with the Euler functions J_z^{2*} and $\mathbf{J}^{2*}$. These have the form

$$J_z^{2*} = \frac{J_z^2}{1 + aJ_z^2 + b(\mathbf{J}^2 - J_z^2)} \tag{5.2}$$

$$\mathbf{J}^{2*} = \frac{\mathbf{J}^2 - J_z^2}{1 + aJ_z^2 + b(\mathbf{J}^2 - J_z^2)} \tag{5.3}$$

where a and b are transformation parameters. The Euler-type Hamiltonian is then

$$\mathcal{H}_{rot}^{E} = \sum_{i,j} X_{ij}(J_z^{2*})^i(\mathbf{J}^{2*})^j + h_3(J_+^6 + J_-^6) \tag{5.4}$$

where X_{ij} are the molecular constants. This can improve the convergence characteristics and the ability to predict the energy of unobserved states. Euler-type Hamiltonians have been successfully used to fit the isotopologues D_2H^+ and H_2D^+, and other molecules which suffer from poorly converging Watson-type Hamiltonians [86, 97, 98, 100].

The Euler functions are built into SPFIT, and the initial guesses for a and b were calculated using the Watson-

type parameters as derived by Pickett [93]. The fit was approached in the same manner as the Watson-type fit by incrementally adding states and parameters, and limiting coefficients to the sextic order or lower. Then, the a and b transformation parameters were adjusted iteratively to achieve the best fit. This performed better than the Watson-type Hamiltonian, with 22 rotational states being fit with 9 parameters, and a reduced RMS error of 1.12. Of the 20 relative energies, 12 were from the accurate newly determined values. The resulting molecular constants and calculated energy levels are also shown in Table 5.6. The results are in good agreement with the predictions from the Watson-type parameters, with the calculated energies of $(1,1)$ and $(1,0)$ differing by 2 and 8 MHz respectively.

Table 5.6: Molecular constants from an Euler-type and Watson-type fit. All values are in MHz, the 1σ uncertainties are given in parentheses in units of the least significant digit.

Parameter	Watson-type	Parameter	Euler-type
		$a \times 10^{-3}$	0.35
		$b \times 10^{-3}$	1.80
B	1306013.96(308)	$X_{01} = B$	1306024.20 (204)
C	618003.61(438)	$X_{10} = C$	617993.57(231)
D_J	1250.39(33)	X_{02}	1096.683(217)
D_{JK}	-2278.51(100)	X_{11}	1354.34(66)
D_K	1134.16(125)	X_{20}	108.897(192)
H_J	2.0886(78)	X_{03}	2.1525(55)
H_{JK}	-8.787(80)	X_{12}	-1.318(35)
H_{KJ}	11.856(224)	X_{21}	1.274(36)
H_K	-5.142(151)		
h_3	-0.2184(44)	h_3	-0.20774(144)
State	Predicted energy		Predicted energy
(1,1)	1922439.0(44)		1922441.1(27)
(1,0)	2607043.1(50)		2607051.1(33)

In order to ensure the chosen parameters were appropriate for predicting low lying energy levels, a test was devised. A new experimental data set was constructed from CDs where the energies of all $G = 2$ states were determined relative to $(2,2)$ instead of $(1,1)$, and all remaining *para* levels were calculated relative to $(2,1)$. This is as if the $(1,1)$ state were forbidden, and the $G = 2$ states were of a different spin species. Then, the parameters were used to fit the new relative energy levels, and the predictions of the $(2,1) - (1,1)$ and $(2,2) - (1,1)$ CDs were compared with the experimental values, which is analogous to calculating the $(1,0)$ and $(1,1)$ energy levels relative to $(0,0)$. Both parameter sets were found to behave satisfactorily, where predictions for the $(2,1) - (1,1)$ and $(2,2) - (1,1)$ CDs by the Watson-type parameters differed with the experimental values by -11(20) MHz and -2(19) MHz respectively, while the predictions from the Euler type parameters differed by -3(11) MHz and 2(9) MHz.

In compiling a set of experimentally determined energy levels, the energies of the $(1,0)$ and $(1,1)$ states relative

to $(0,0)$ were calculated using the Euler-type molecular constants, because of their overall better performance in fitting the ground state and predicting low lying energy levels. After this, CDs and transition frequencies were used to calculate the remaining energy levels. In cases where a state could be calculated with different sets of CDs or transitions, the average value was calculated. In total, 62 absolute energy levels were determined, with 18 in the ground state, 33 in the ν_2 state, and 11 in the $2\nu_2^2$ state with uncertainties of ~10 MHz. These can be found in Table 5.7.

Table 5.7: Experimentally determined energy levels of H_3^+ rovibrational states relative to $(0,0)$. The energy levels were calculated from CDs, rovibrational transition frequencies, and the energies of $(1,1)$ and $(1,0)$ as determined by molecular constants.

$(J,G)u\|l$	Energy/MHz	Energy/cm^{-1}
Ground state		
$(1,1)$	1922441.1(27)	64.12573(9)
$(1,0)$	2607051.1(33)	86.96186(11)
$(2,2)$	5075561.1(81)	169.30259(27)
$(2,1)$	7115800.4(48)	237.35755(16)
$(3,3)$	9454074.6(66)	315.35399(22)
$(3,2)$	12831800.4(91)	428.02279(29)
$(3,1)$	14832773.2(74)	494.76806(25)
$(4,4)$	15050853.0(102)	502.04241(34)
$(3,0)$	15495739.9(77)	516.88225(25)
$(4,3)$	19747935.6(79)	658.72023(25)
$(4,2)$	23038282.9(103)	768.47440(34)
$(4,1)$	24990076.7(94)	833.57923(31)
$(5,4)$	27850004.6(116)	928.97615(39)
$(5,3)$	32392186.3(93)	1080.48703(31)
$(5,2)$	35588431.6(118)	1187.10230(39)
$(5,0)$	38111466.6(111)	1271.26169(37)
$(6,4)$	42891749.4(129)	1430.71475(43)
$(6,3)$	47287108.5(109)	1577.32816(36)
ν_2		
$(1,2)$	76392298.8(112)	2548.17280(37)
$(1,1)$	78232195.2(37)	2609.54514(12)
$(2,3)$	78374281.2(73)	2614.28462(24)
$(1,0)$	78446276.7(41)	2616.68613(13)
$(3,4)$	81528373.8(116)	2719.49382(39)
$(2,2)$	81662507.3(97)	2723.96804(32)
$(2,1)l$	82609863.8(48)	2755.56845(16)
$(2,1)u$	83652460.9(48)	2790.34574(16)
$(2,0)$	84327427.7(33)	2812.86021(11)
$(3,3)$	86245797.8(83)	2876.85015(27)

Table 5.7: (cont.)

$(3,2)l$	87880331.0(81)	2931.37231(27)
$(3,2)u$	89711098.9(91)	2992.44015(29)
$(3,1)l$	90024740.3(54)	3002.90210(18)
$(3,0)$	90715994.1(86)	3025.95985(29)
$(3,1)u$	91840646.5(85)	3063.47421(27)
$(4,4)$	92016235.0(102)	3069.33121(36)
$(4,3)l$	94293085.9(78)	3145.27879(25)
$(4,3)u$	96934264.0(78)	3233.37901(25)
$(4,2)l$	97738917.5(105)	3260.21936(35)
$(4,1)l$	99714493.5(94)	3326.11748(31)
$(4,2)u$	100471999.8(101)	3351.38517(34)
$(5,4)l$	101825501.5(109)	3396.53312(39)
$(4,1)u$	102622585.9(85)	3423.12100(27)
$(4,0)$	103339935.5(86)	3447.04921(29)
$(5,4)u$	105231784.6(109)	3510.15449(39)
$(5,3)l$	106526370.9(95)	3553.33725(32)
$(5,2)l$	109734426.5(118)	3660.34647(39)
$(5,3)u$	110142653.1(91)	3673.96344(29)
$(5,0)$	112217852.2(118)	3743.18463(39)
$(5,2)u$	113712178.2(111)	3793.02998(37)
$(5,1)u$	115822055.2(102)	3863.40791(34)
$(6,4)l$	116443418.7(123)	3884.13435(43)
$(6,3)l$	120817670.7(109)	4030.04370(36)
$2\nu_2^2$		
$(2,4)$	150867809.0(48)	5032.40842(16)
$(1,2)$	152523216.7(91)	5087.62688(29)
$(2,3)$	155328183.2(52)	5181.19049(17)
$(2,2)$	157883782.4(112)	5266.43610(37)
$(2,0)$	158497901.5(63)	5286.92091(21)
$(3,4)$	158867356.4(98)	5299.24460(33)
$(3,3)$	162821175.1(92)	5431.12980(31)
$(4,5)$	163700993.3(99)	5460.47737(33)
$(3,0)$	166906399.7(77)	5567.39822(25)
$(4,4)$	169457282.5(120)	5652.48651(40)
$(5,0)$	191623790.5(111)	6391.88163(37)

Comparing theory and experiment

The accurate and precise experimentally determined energy levels can be directly compared with highly accurate calculations, which can reveal structure in the residuals that was previously hidden in the noise. Calculations are currently limited by the treatment of nonadiabatic coupling between electronic and nuclear motion, which is caused by electrons following the nuclei and increasing their effective mass [5]. The new experimental results can be used to closely assess the behavior of different approaches to this problem.

A straightforward method for addressing nonadiabatic effects is to use motion-dependent masses for the vibrational and rotational terms in the kinetic energy operator. However, determining the appropriate effective masses from first principles is challenging. For H_2^+, Moss used a perturbative approach to calculate the effective vibrational mass [120], which was larger than the nuclear mass (m_{nuc}) by approximately one half of the mass of an electron (m_e). When the Moss mass (m_{nuc} + 0.47531m_e) was adopted for calculations of H_3^+, it improved agreement with rovibrational transition frequencies by a factor of two with an RMS error of 0.101 cm^{-1}[121]. Mátyus *et al.* scaled the vibrational mass in order to achieve the best possible agreement with experimental transition frequencies, and found a minimum at a lower effective mass of m_{nuc} + 0.31224m_e [121]. This improved the agreement with experimental values by an order of magnitude to 0.008 cm^{-1}. However, when these results are compared with the experimentally determined absolute energy levels the differences have an RMS error of 0.026 cm^{-1}, which is indicative of a cancellation of error when comparing with transition frequencies. A comparison between the experimental energy levels and calculations using nuclear, Moss, and empirically scaled vibrational masses is shown in Fig. 5.4. Changing the effective vibrational mass shifts the offset of the ν_2 state, while in all three calculations the disagreement changes with the rotational energy by approximately -1.5 MHz/cm^{-1}.

To address rotational contributions to the nonadiabatic coupling, Diniz *et al* [29]. calculated a coordinate-dependent rotational mass using an empirically derived formula. Additionally, coordinate-dependent vibrational masses were calculated using Mullikan analysis of the electron density for the ground and ν_2 vibrational states. These surfaces were scaled using experimental transition frequencies to determine effective rotational and vibrational masses, and a comparison between the results of Diniz *et al.* and the new experimentally derived energy levels is shown in Fig. 5.5. The effective masses both removed the offset of the ν_2 state and reduced the rotational energy dependence of the residuals to 270 kHz/cm^{-1}, resulting in an RMS error of 0.01 cm^{-1}.

The accurate experimental rotational levels also reveal further structure in the residuals. In addition to the linear dependence of the disagreement on the state's energy, there is a clear dependence on G. Figure 5.6 shows the difference between the experimentally determined ground state energy levels and values calculated by Diniz *et al* [29]. The residuals of energy levels with the same G were fit to a line, and it was found that the slope was unaffected by the magnitude of G, while the intercept clearly increased with G. This trend also exists for calculations which use fixed

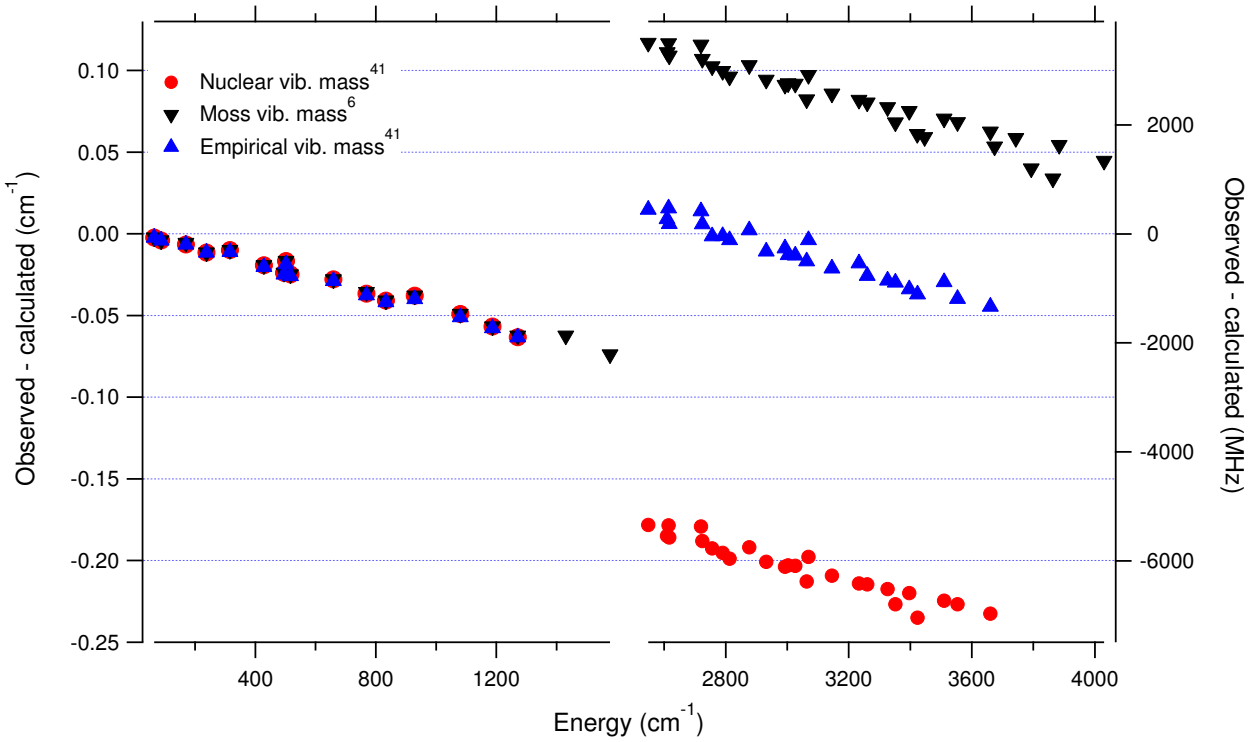

Figure 5.4: The differences between the experimental energy levels and calculations which used nuclear rotational masses and different effective vibrational masses [29, 121].

masses, and Fig. 5.7 shows the intercepts of the linear fits for different G values from calculations using scaled and nuclear rotational mass. Despite the slopes of the two approaches being significantly different (-1.5 MHz/cm^{-1}and 270 kHz/cm^{-1}), the intercepts are quite similar, and both have a quadratic relationship with G. This could be due to the rotational nonadiabatic coupling having a dependence on the projection of angular momentum on the molecular axis, and this behavior cannot be captured by simply scaling the rotational mass of the nuclei. Although the general trend also exists for the ν_2 state, it is not as clear of an effect.

5.5 Conclusion

In this work, we report the results of a precise and accurate spectroscopic survey of H_3^+ rovibrational transitions in the $\nu_2 \leftarrow 0$, $2\nu_2^2 \leftarrow \nu_2$, and $2\nu_2^2 \leftarrow 0$ bands using the sub-Doppler technique NICE-OHVMS and frequency calibration with an OFC. Measurements spanned from 1.96–4.51 μm, and in total 54 transitions had their uncertainties improved by more than an order of magnitude. These are the first sub-Doppler measurements of H_3^+ overtone and hot band transitions, which allowed for accurate and precise determination of energy level spacings in the ground state using

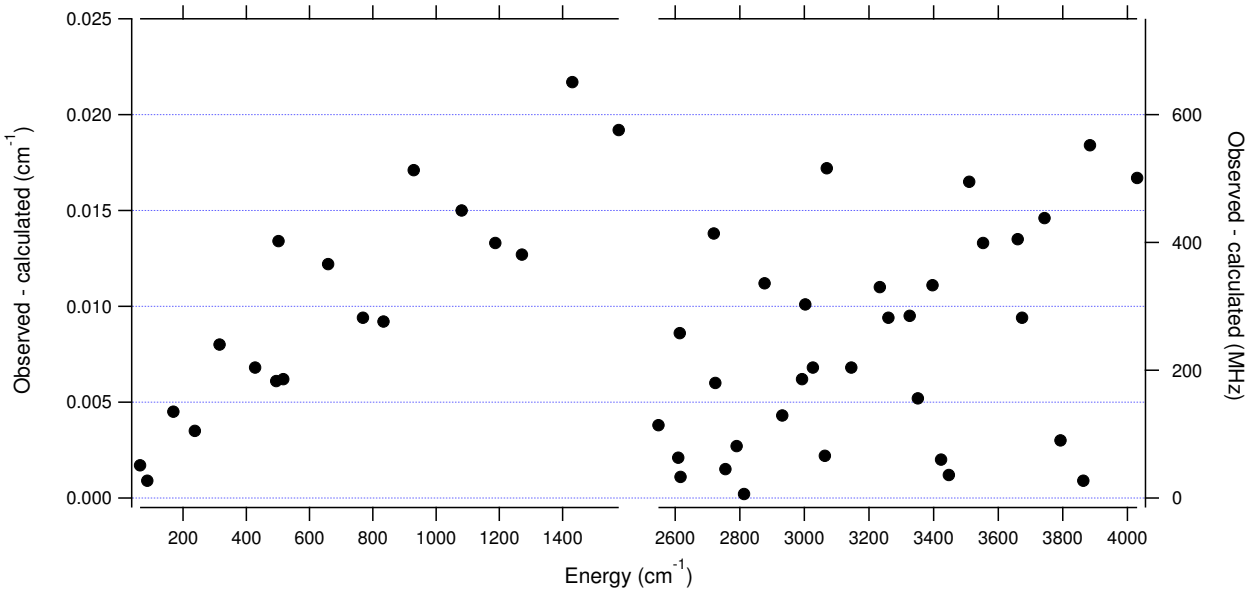

Figure 5.5: The differences between the experimental energy levels and calculations which used scaled rotational and vibrational coordinate-dependent masses [29].

CDs, including between states with $\Delta G = \pm 3$. This in turn allowed for the direct prediction of 16 forbidden rotational transitions with uncertainties of approximately 10 MHz. This includes the transition $(4,4) \leftarrow (3,1)$ which is a possible astrophysical maser, and the improved frequency of this transition opens up a new avenue for astronomical detection of H_3^+.

Ground state molecular constants were determined by fitting the relative energy levels to an effective Hamiltonian, which were used to calculate the energies of the lowest *ortho* and *para* levels relative to the forbidden $(0,0)$ level. This allowed for 62 accurate rovibrational energy levels to be determined through CDs and rovibrational transition frequencies. These results were compared with accurate *ab initio* calculations, and the residuals revealed a dependence on G which could not be discerned with comparisons to previous experimental measurements. As theorists continue to develop new strategies for addressing nonadiabatic effects for this fundamental molecular system, the results from this work will provide valuable experimental benchmarks.

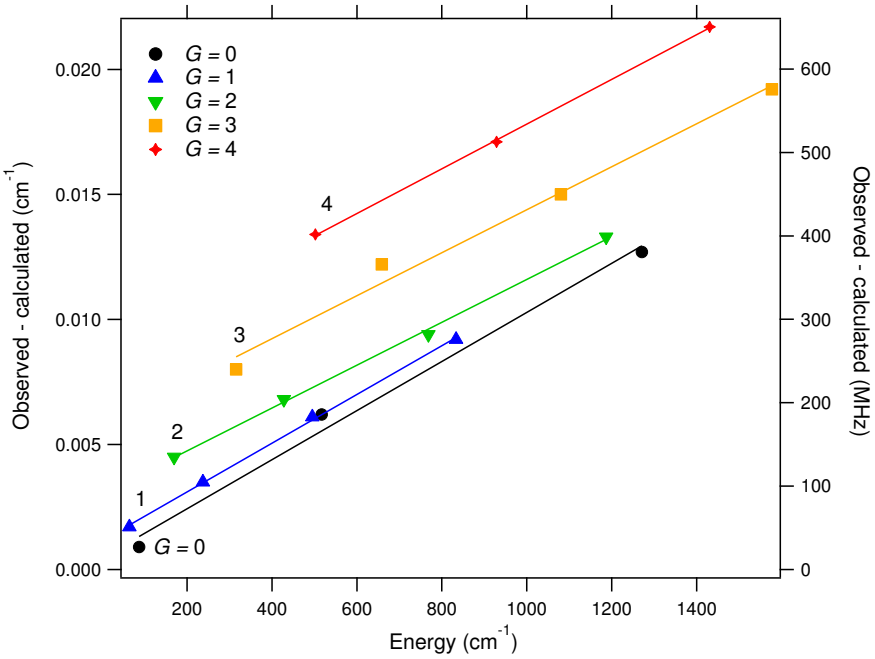

Figure 5.6: A comparison between the experimental and calculated ground state energy levels using scaled rotational and vibrational coordinate-dependent masses [29], with the G value of the state color coded. Linear fits of each G value are shown to demonstrate the G-dependent offset.

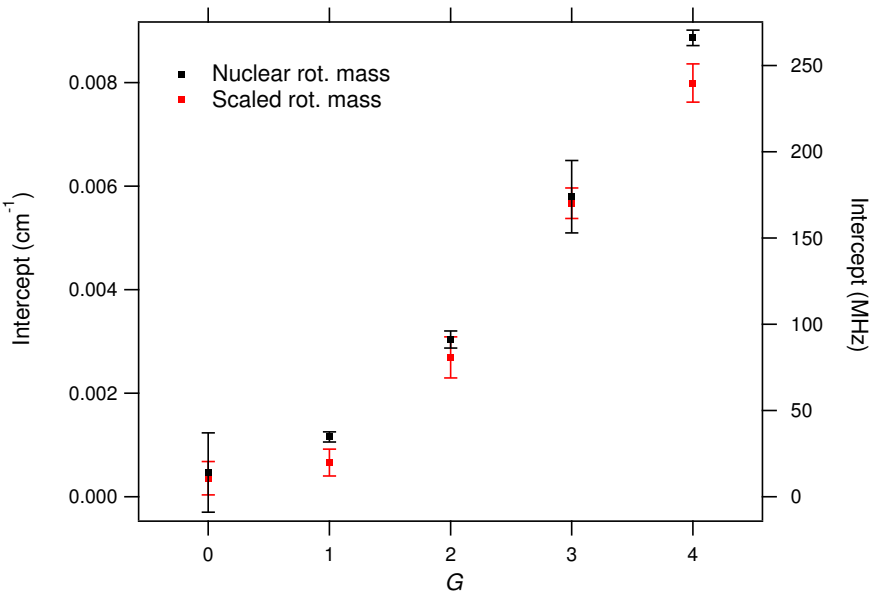

Figure 5.7: The intercepts of the linear fits of the observed - calculated values for both scaled and nuclear rotational masses for different G values in the ground vibrational state [29]. The error bars are the uncertainty of the intercepts determined by the least-squares fits.

5.6 Combination differences

Table 5.8: Ground state CDs of H_3^+ and the transitions used to calculate them. All frequencies are in MHz, the uncertainties are given in parentheses in units of the least significant digit.

$(J',G')-(J'',G'')$	Contributing transitions		Energy difference
$(2,1)-(1,1)$	$\nu_2 \leftarrow 0$	$R(1,1)^u[90]$, $Q(2,1)^u$	5193359.2(40)
$(2,1)-(1,1)$	$\nu_2 \leftarrow 0$	$R(1,1)^l[90]$, $Q(2,1)^l$	5193359.5(40)
$(3,1)-(2,1)$	$\nu_2 \leftarrow 0$	$R(2,1)^u[42]$, $Q(3,1)^u$	7716972.8(56)
$(3,2)-(2,2)$	$\nu_2 \leftarrow 0$	$R(2,2)^u[90]$, $Q(3,2)^u$	7756239.3(40)
$(4,1)-(3,1)$	$\nu_2 \leftarrow 0$	$R(3,1)^l$, $Q(4,1)^l$	10157302.1(56)
$(4,1)-(3,1)$	$\nu_2 \leftarrow 0$	$Q(3,1)^u[43]$, $P(4,1)^u$	10157304.8(56)
$(4,2)-(3,2)$	$\nu_2 \leftarrow 0$	$R(3,2)^u[103]$, $Q(4,2)^u$	10206479.3(41)
$(4,2)-(3,2)$	$\nu_2 \leftarrow 0$	$R(3,2)^l[42]$, $Q(4,2)^l$	10206485.8(56)
$(4,3)-(3,3)$	$\nu_2 \leftarrow 0$	$R(3,3)^u[103]$, $Q(4,3)^u$	10293857.6(41)
$(4,3)-(3,3)$	$\nu_2 \leftarrow 0$	$R(3,3)^l[103]$, $Q(4,3)^l$	10293864.3(40)
$(4,3)-(3,3)$	$\nu_2 \leftarrow 0$	$Q(3,3)[103]$, $P(4,3)$	10293861.1(47)
$(5,2)-(4,2)$	$\nu_2 \leftarrow 0$	$R(4,2)^l$, $Q(5,2)^l$	12550148.7(56)
$(5,3)-(4,3)$	$\nu_2 \leftarrow 0$	$R(4,3)^l[103]$, $Q(5,3)^l$	12644246.8(56)
$(5,3)-(4,3)$	$\nu_2 \leftarrow 0$	$R(4,3)^u[103]$, $Q(5,3)^u$	12644254.4(41)
$(5,4)-(4,4)$	$\nu_2 \leftarrow 0$	$R(4,4)^u$, $Q(5,4)^u$	12799151.5(56)
$(5,4)-(4,4)$	$\nu_2 \leftarrow 0$	$R(4,4)^l[43]$, $Q(5,4)^l$	12799151.6(56)
$(3,0)-(1,0)$	$\nu_2 \leftarrow 0$	$R(1,0)[90]$, $Q(3,0)$	12888688.8(69)
	$2\nu_2^2 \leftarrow \nu_2$	$R(2,0)$, $Q(3,0)$	
$(6,3)-(5,3)$	$\nu_2 \leftarrow 0$	$R(5,3)^l$, $Q(6,3)^l$	14894922.2(56)
$(6,4)-(5,4)$	$\nu_2 \leftarrow 0$	$R(5,4)^l$, $Q(6,4)^l$	15041744.8(56)
$(6,5)-(5,5)$	$\nu_2 \leftarrow 0$	$R(5,5)^l[103]$, $Q(6,5)^l$	15272463.6(40)
$(5,0)-(3,0)$	$\nu_2 \leftarrow 0$	$R(3,0)$, $Q(5,0)$	22615726.8(80)
	$2\nu_2^2 \leftarrow \nu_2$	$R(4,0)$, $Q(5,0)$	
$\Delta G = 3$			
$(2,1)-(2,2)$	$\nu_2 \leftarrow 0$	$Q(2,2)[103]$	2040242.2(59)
	$2\nu_2^2 \leftarrow \nu_2$	$Q(2,2)$	
	$2\nu_2^2 \leftarrow 0$	${}^nQ(2,1)$	
$(2,2)-(1,1)$	$\nu_2 \leftarrow 0$	$Q(2,2)[103]$	3153122.9(81)
	$2\nu_2^2 \leftarrow \nu_2$	$R(1,2)$, $Q(2,2)$, $Q(1,2)$	
	$2\nu_2^2 \leftarrow 0$	${}^nQ(1,1)$	
$(3,3)-(1,0)$	$\nu_2 \leftarrow 0$	$Q(1,0)[103]$	6847023.5(57)
	$2\nu_2^2 \leftarrow \nu_2$	$R(1,0)$	
	$2\nu_2^2 \leftarrow 0$	${}^nP(3,3)$	
$(4,4)-(2,1)$	$\nu_2 \leftarrow 0$	$Q(4,4)$	7935052.5(89)
	$2\nu_2^2 \leftarrow \nu_2$	$R(3,4)$, $Q(4,4)$, $Q(3,4)$	
	$2\nu_2^2 \leftarrow 0$	${}^tR(2,1)$	

(Table 5.8: cont.)

$(4,4)-(2,1)$	$\nu_2 \leftarrow 0$	$P(4,4)$	7935052.8(69)
	$2\nu_2^2 \leftarrow \nu_2$	$Q(3,4)$	
	$2\nu_2^2 \leftarrow 0$	${}^tR(2,1)$	

Chapter 6

Rovibrational and rotational spectroscopy of $CH_2NH_2^+$

The simplest primary imine, methanimine (methylene imine, CH_2NH), has been observed in a variety of objects in the interstellar medium (ISM), including giant molecular clouds [122], hot cores [123, 124], infrared galaxies [125], and both high mass and solar-type protostellar systems [126, 127]. As a possible precursor to the amino acid glycine [126], its formation and reactivity are of particular interest to astronomers. Unlike methylamine (CH_3NH_2) which is thought to form on the surface of interstellar dust grains [128], gas phase reactions are needed to explain the observed abundances of CH_2NH. The dominant formation path is predicted to be through the neutral-neutral reaction of NH + $CH_3 \rightarrow CH_2NH$ +H, which can occur during the "warm up phase" after the birth of a nearby protostar [126]. The second most significant route is predicted to be dissociative recombination of $CH_2NH_2^+$ with e^-, where $CH_2NH_2^+$ is formed through the ion-neutral reaction $CH_2^+ + NH_3 \rightarrow CH_2NH_2^+ + H$ [126]. Having a high proton affinity of $\sim$ 200 kcal/mol [129], it is likely that CH_2NH would be protonated by interstellar H_3^+, HCO^+, or H_3O^+ to reform $CH_2NH_2^+$. Observations of $CH_2NH_2^+$ would provide valuable insight into the formation of CH_2NH. However, the lack of high resolution spectroscopic data has prevented an astronomical search.

Methanimine and its protonated form, methaniminium cation, also play an important role in the thermosphere of Titan. When the *Cassini* orbiter passed through Titan's upper atmosphere, the Ion and Neutral Mass Spectrometer (INMS) observed a plethora of N-bearing molecules [130]. A signal at mass 30 was assigned to $CH_2NH_2^+$, indicating that it is one the most abundant species in Titan's atmosphere from 1000–1200 km and implying a high abundance of CH_2NH. Dissociative recombination of $CH_2NH_2^+$ is thought to be a critical step in the formation of ammonia in the upper atmosphere of Titan [131]. Additionally, the barrierless reaction between CH_2NH and $CH_2NH_2^+$ can initiate polymerization, which could be an important step towards aerosol production in Titan's atmosphere [132]. Until another mission reaches the Saturnian system, future studies of $CH_2NH_2^+$ in Titan's upper atmosphere must be accomplished remotely through observations of its vibrational and rotational transitions.

The only spectroscopic studies of $CH_2NH_2^+$ have been through low-resolution infrared (IR) measurements of the argon tagged species [133] and the *ab initio* calculations performed by Thackston & Fortenberry [134]. Therefore, we

have surveyed the fundamental band of the ν_4 CH symmetric stretch mode of $CH_2NH_2^+$, using literature values the band origin [133, 134] and our own calculations of the rotational structure. The rovibrational data were used to predict pure rotational transition frequencies, which were then measured directly using rotation-vibration double resonance spectroscopy. This work presents the first rotational measurements of $CH_2NH_2^+$, and is the first demonstration of double resonance using laser-induced inhibition of complex growth (LIICG).

6.1 Experimental methods

The rovibrational and rotational transitions of $CH_2NH_2^+$ were measured in the 4 K trapping instrument COLTRAP, which has previously been described in detail [135, 136]. In brief, the ions were generated in a storage ion source by electron impact ionization ($E_e \approx 30$ eV) of the precursor gas (CH_3NH_2, Aldrich Chem. Corporation, CAS 74-89-5, 98%), which was admitted to the source via a slightly heated leakage valve. Every second, a pulse of several ten thousand mass-selected $CH_2NH_2^+$ ions ($m = 30$ u) was injected into the 22-pole ion trap connected to a coldhead, which was held at 4 K and filled with $\sim 10^{14}$ cm^{-3} He. During the trapping time of 700 ms, $CH_2NH_2^+$-He complexes formed by three-body collisions with He. In the action spectroscopic methods applied here (see details below), the resonant absorption of the infrared (IR) and/or mm-wave radiation by the trapped cold $CH_2NH_2^+$ cations is detected by observing the decrease in the number of $CH_2NH_2^+$-He complexes. A transition is thus recorded by repeatedly extracting the ion ensemble from the trap in 1 s cycles and counting the mass-selected $CH_2NH_2^+$-He complexes ($m = 34$ u) as a function of the irradiation frequency.

The IR radiation was supplied by an Aculight Argos Model 2400 cw optical parametric oscillator (OPO), operating in the 3 μm spectral region. Its narrow beam was sent through the 22-pole ion trap via a thin diamond vacuum window, with power on the order of 100 mW. The frequency of the IR radiation has been measured by a Bristol model 621A wavemeter with an accuracy of about 0.001 cm^{-1}. The mm-wave radiation was supplied by a synthesizer driving a multiplier chain source (Virginia Diodes, Inc.) covering the range 170-1100 GHz. The synthesizer (Rohde & Schwarz SMF100A) was locked to a rubidium atomic clock with a typical stability of 10^{-11}. For the double-resonance experiments both radiation sources were used simultaneously, and their beams combined by an elliptical mirror containing a small hole for the IR beam [137].

The action spectroscopic methods used in this work exploit the fact that excitation of the bare cation can inhibit He-attachment in a ternary collision process at 4 K. Such a scheme was first demonstrated for electronic excitation [138] and later rovibrational excitation [136, 139, 140, 141, 142, 143] and is now referred to as LIICG. Very interestingly, rotational excitation is also able to influence the ternary rate coefficient for He attachment [144], and can therefore be used to record high-resolution rotational spectra of molecular cations [143, 145, 146, 147, 148, 149, 150]. But in

contrast to electronic or vibrational excitation, the photons involved in molecular rotational transitions carry very little energy (on the order of only $E/hc \approx 10$ cm^{-1}), so the depletion of the complexes upon resonant absorption is rather limited, since the ternary attachment of He is hindered instead of inhibited. To improve this limited depletion signal in a pure rotational excitation, we present here a double resonance scheme which is based on the more pronounced LIICG-signal of the rovibrational excitation. For vibrational excitation into a typical C-H stretching mode the internal energy of the naked cation is increased by about $E/hc \approx 3000$ cm^{-1}, which is much higher than a typical helium binding energy corresponding to some 50 cm^{-1}. For this scheme, the IR excitation frequency of the OPO is held on a rovibrational transition, producing a LIICG depletion signal. This LIICG depletion can then be altered by a rotational transition which pumps additional ions into the rotational state probed by the IR laser (for a detailed example see Section 6.4). By scanning the mm-wave excitation frequency over the rotational transition frequency while the IR wavenumber is kept fixed on resonance, the rotational line can be recorded. As it turns out in this work, this novel double resonance scheme exhibits a signal up to 2–3 times stronger than the rotation-only method, which enabled the detection of weak pure rotational transitions of $CH_2NH_2^+$.

6.2 Computational methods

Complementary quantum-chemical calculations to support the spectroscopic search of $CH_2NH_2^+$ were performed using the CCSD(T) method [151] and Dunning's correlation consistent basis sets [152, 153] which has been shown earlier to provide very accurate equilibrium structural parameters. [154, 155, 156] The calculations were performed with the Cfour suite of programs [157, 158] considering all electrons (ae) in the correlation treatment throughout. Molecular structures were calculated using analytic gradient techniques [159]. Harmonic and anharmonic force fields were calculated at the ae-CCSD(T)/cc-pwCVQZ level of theory using analytic second-derivative techniques [160, 161] followed by additional numerical differentiation to calculate the third and fourth derivatives needed for the anharmonic force fields [161, 162]. A more complete review of the underlying theory is given elsewhere [163]. Best-estimate ground state rotational constants were calculated from the calculated zero-point vibrational corrections $\Delta A_0 = \frac{1}{2}\sum_{i=1}^{12} \alpha_i^A$ (with similar relations for ΔB_0 and ΔC_0; see Table 6.1) and the equilibrium rotational constants obtained at the ae-CCSD(T)/cc-pwCV5Z level (Figure 6.1). Rotational constants of the $v_2 = 1$ state were estimated from the calculated best-estimate ground state rotational constants and the corresponding calculated rotation-vibration interaction constants (Table 6.4).

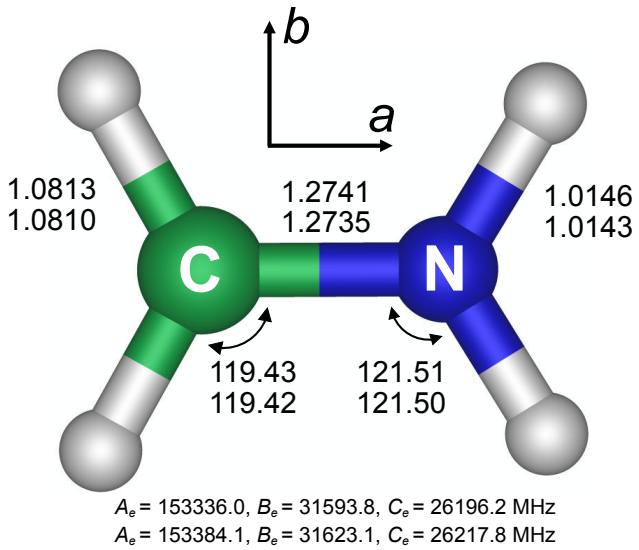

Figure 6.1: Equilibrium structural parameters and rotational constants of $CH_2NH_2^+$ calculated at the CCSD(T)/cc-pwCVQZ (top values) and CCSD(T)/cc-pwCV5Z (bottom values) levels of theory. Bond lengths are given in units of Å and angles in degrees. The permanent electric dipole moment is oriented along the *a* main inertial axis.

6.3 Vibrational spectroscopy

Given that methanimine is isoelectronic with ethylene, C_2H_4, it was expected to be a closed-shell planar molecule. This is supported by quantum-chemical calculations, which also predict it to be near the prolate limit ($\kappa = \frac{2B-A-C}{A-C} = -0.91$, as calculated from the rotational constants summarized in Table 6.4) with C_{2v} symmetry. Except for the ν_6 vibration mode of a_2 symmetry (Table 6.1), all $3N - 6 = 12$ fundamental vibrational modes are infrared active (cf. Ref [134]). Four of those, the N-H and C-H stretching modes ν_1 (symmetric N-H stretch), ν_2 (symmetric C-H stretch), ν_9 (antisymmetric N-H stretch) and ν_{10} (antisymmetric C-H stretch) located around 3μm were observed previously at low spectral resolution using infrared photodissociation of the argon-tagged ion [133]. In the present study, the fundamental *a*-type band ν_2 was targeted in a first high-resolution investigation, most importantly to provide predictions of the ground-state pure rotational spectrum. A search for rovibrational lines of $CH_2NH_2^+$ soon revealed features close to predictions based on the spectroscopic parameters reported in the literature [133, 134] and Tables 6.1 and 6.4. Because of the low temperature of the ion trap and the efficient cooling due to the large mass ratio between the cation and the He buffer gas [164]. the transitions showed narrow Doppler widths of $\sim$ 30 MHz corresponding to a kinetic temperature of 10 K. Predissociation lines of the $CH_2NH_2^+$-He complex were also observed, but could be easily distinguished from lines of the bare ion through their wider life-time broadened Lorentzian profiles. In total, 39 rovibrational transitions of $CH_2NH_2^+$ were measured with uncertainties of $\sim$ 0.001 cm^{-1}, which are summarized in Table 6.2 and shown in Fig. 6.2. Two examples of LIICG scans of $CH_2NH_2^+$ transitions are also shown in Fig. 6.2 as insets. The survey reached $J'' = 5$, and spanned from ${}^pP_a(5_{05})$ to ${}^rR_a(5_{05})$.

Table 6.1: Harmonic and anharmonic vibrational wavenumbers (in cm^{-1}), rotation-vibration interaction constants $\alpha_i^{A,B,C}$ and zero-point vibrational contributions to the rotational constants $\frac{1}{2}\sum_i \alpha_i^{A,B,C}$ (in MHz) calculated at the ae-CCSD(T)/cc-pwCVQZ level of theory.

Mode	Harm	Anharm	α_i^A	α_i^B	α_i^C
$\nu_1(a_1)$	3499	3337	1200.60	44.63	66.24
$\nu_2(a_1)$	3166	3027	1314.23	45.11	71.65
$\nu_3(a_1)$	1766	1705	−496.86	45.85	139.45
$\nu_4(a_1)$	1601	1558	−1338.67	−101.75	68.27
$\nu_5(a_1)$	1462	1434	−719.11	−96.60	−42.43
$\nu_6(a_2)$	1083	1053	2552.37	−793.62	0.54
$\nu_7(b_1)$	1162	1142	1134.03	261.24	−25.97
$\nu_8(b_1)$	942	927	20268.82	158.20	−22.88
$\nu_9(b_2)$	3605	3430	874.27	62.08	54.45
$\nu_{10}(b_2)$	3291	3149	916.38	65.04	57.22
$\nu_{11}(b_2)$	1365	1336	−4147.47	−34.07	196.69
$\nu_{12}(b_2)$	962	956	−17886.56	904.97	60.14
$\frac{1}{2}\Sigma_i\alpha_i^{A,B,C}$			1836.01	280.55	311.68

The band origin was found to be 3026.44493(30) cm^{-1}, which is 16 cm^{-1}higher than the value calculated by Thackston and Fortenberry [134], and within 1 $cm^{-1}$to the value calculated here (Table 6.1) and observed experimentally by Wagner *et al.* using infrared photodissociation of the argon complex.

6.4 Rotational spectroscopy

A search was performed for the pure rotational *a*-type transitions using molecular constants from the fit of the rovibrational data. With a calculated dipole moment of 0.45 D [134], the rotational transitions are not particularly strong. The new IR/mm-wave double resonance spectroscopy scheme described in the experimental section was mainly used to measure the rotational transitions. The scheme is shown in Fig. 6.3a for the rotational transition $4_{04} \leftarrow 3_{03}$. Here, the wavenumber of the IR radiation is held on a rovibrational transition ($\nu_2 = 1 \leftarrow 0$, $5_{05} \leftarrow 4_{04}$ at 3035.8220 cm^{-1}). By this resonant excitation, the $CH_2NH_2^+$-He complexes are decreased by typically a few hundred counts, as can be seen in the insets of Fig. 6.2. When the mm-wave frequency is resonant with the rotational transition $4_{04} \leftarrow 3_{03}$, population will be shifted to the initial state of the rovibrational transition (4_{04}), causing an additional depletion of $CH_2NH_2^+$-He complexes. After normalization to the baseline counts (i.e., the counts with the mm-wave radiation being off-resonant), the double resonance signals were found to be stronger than the direct rotational measurements by a factor of 2–3, and a comparison of a transition measured using each method is shown in Fig. 6.3b. This corresponds to a factor of 4–9 reduction in averaging time. Overall, nine rotational transitions, summarized in Table 6.3 and shown in Fig. 6.4, were measured using double resonance. The lines were typically measured several times (up to 7 times), and

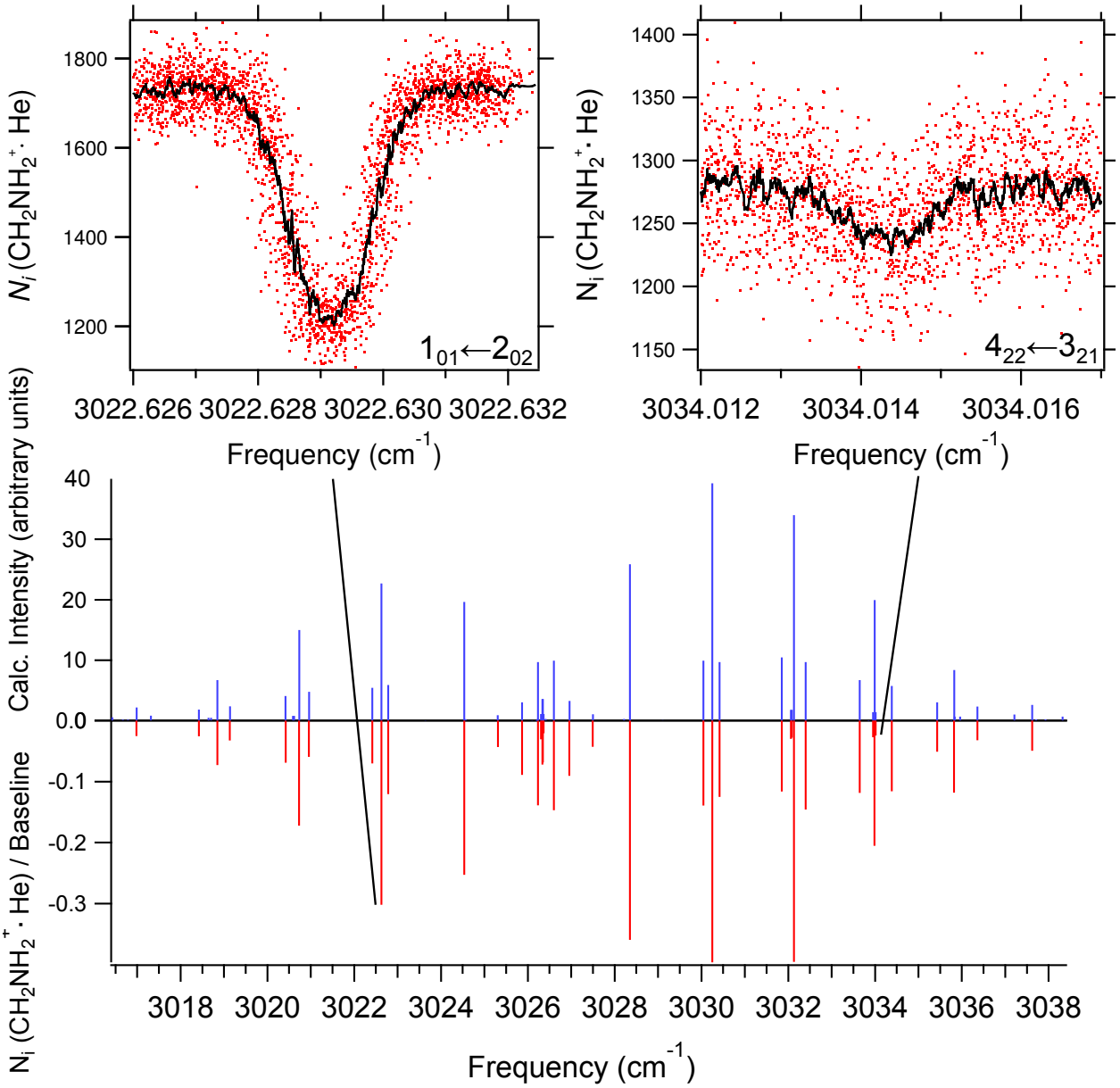

Figure 6.2: Stick spectra of the ν_2 C-H symmetric stretch fundamental band of $CH_2NH_2^+$, with experimental values shown in red and simulated values calculated using PGOPHER [165] are shown in blue. The insets show scans of representative strong and weak transitions, with the boxcar averaged trace in black. An intensity fit determined a rotational temperature of 11 K.

fitted with Gaussian profiles. The individual center frequencies and uncertainties obtained by the fits were combined to yield the values given in Table 6.3. The combined uncertainties for the rotational transitions are on the order of 5 kHz.

The transitions were found to be broader by a factor of 2 to 3 compared to the calculated Doppler widths at 10 K. As calculated at the CCSD(T)/cc-pwCV5Z level of theory, the nitrogen nuclear quadrupole coupling constants are

Table 6.2: Frequencies of rovibrational transitions (in cm^{-1}) of $CH_2NH_2^+$. The precision of the wavemeter was $\sim 1 \times 10^{-3}$ cm^{-1}. The intensity is the depth of the transition relative to the baseline counts.

$J'_{Ka'Kc'} \leftarrow J''_{Ka''Kc''}$	Experimental	Obs - calc	Intensity
$4_{04} \leftarrow 5_{05}$	3016.9836	−0.0013	−0.025
$3_{12} \leftarrow 4_{13}$	3018.4210	−0.0001	−0.026
$3_{03} \leftarrow 4_{04}$	3018.8493	0.0004	−0.073
$3_{13} \leftarrow 4_{14}$	3019.1358	0.0004	−0.033
$2_{11} \leftarrow 3_{12}$	3020.4192	0.0004	−0.069
$2_{02} \leftarrow 3_{03}$	3020.7314	−0.0005	−0.172
$2_{12} \leftarrow 3_{13}$	3020.9569	−0.0007	−0.059
$1_{10} \leftarrow 2_{11}$	3022.4189	−0.0004	−0.070
$1_{01} \leftarrow 2_{02}$	3022.6292	−0.0002	−0.302
$1_{11} \leftarrow 2_{12}$	3022.7807	0.0005	−0.120
$0_{00} \leftarrow 1_{01}$	3024.5356	0.0000	−0.253
$3_{13} \leftarrow 3_{12}$	3025.3108	0.0007	−0.043
$2_{12} \leftarrow 2_{11}$	3025.8664	0.0007	−0.089
$1_{11} \leftarrow 1_{10}$	3026.2355	−0.0006	−0.139
$3_{22} \leftarrow 3_{21}$	3026.3021	−0.0001	−0.031
$2_{21} \leftarrow 2_{20}$	3026.3342	−0.0012	−0.072
$2_{20} \leftarrow 2_{21}$	3026.3465	−0.0010	−0.069
$3_{21} \leftarrow 3_{22}$	3026.3625	−0.0005	−0.021
$1_{10} \leftarrow 1_{11}$	3026.6008	0.0003	−0.147
$2_{11} \leftarrow 2_{12}$	3026.9575	−0.0013	−0.091
$3_{12} \leftarrow 3_{13}$	3027.4961	0.0001	−0.043
$1_{01} \leftarrow 0_{00}$	3028.3510	−0.0002	−0.360
$2_{12} \leftarrow 1_{11}$	3030.0465	−0.0005	−0.139
$2_{02} \leftarrow 1_{01}$	3030.2487	0.0003	−0.396
$2_{11} \leftarrow 1_{10}$	3030.4153	0.0006	−0.125
$3_{13} \leftarrow 2_{12}$	3031.8513	0.0013	−0.116
$3_{22} \leftarrow 2_{21}$	3032.0601	0.0002	−0.030
$3_{21} \leftarrow 2_{20}$	3032.0848	0.0002	−0.028
$3_{03} \leftarrow 2_{02}$	3032.1300	0.0001	−0.395
$3_{12} \leftarrow 2_{11}$	3032.4041	−0.0001	−0.146
$4_{14} \leftarrow 3_{13}$	3033.6462	0.0014	−0.119
$4_{23} \leftarrow 3_{22}$	3033.9520	0.0000	−0.027
$4_{04} \leftarrow 3_{03}$	3033.9889	−0.0008	−0.205
$4_{22} \leftarrow 3_{21}$	3034.0143	0.0003	−0.025
$4_{13} \leftarrow 3_{12}$	3034.3870	0.0008	−0.116
$5_{15} \leftarrow 4_{14}$	3035.4319	0.0021	−0.051
$5_{05} \leftarrow 4_{04}$	3035.8220	−0.0001	−0.118
$5_{14} \leftarrow 4_{13}$	3036.3602	0.0012	−0.032
$6_{06} \leftarrow 5_{05}$	3037.6206	−0.0021	−0.049

very small ($\chi_{aa} = 0.126$ MHz and $\chi_{bb} = -0.104$ MHz, Table 6.4) and as a consequence no hyperfine structure was resolved in the spectra recorded here. Simulations of the hyperfine structure from the calculated quadrupole coupling constants (see, e.g., Fig. 6.3) suggest that the line widths are most likely a consequence of power broadening from the mm-wave source.

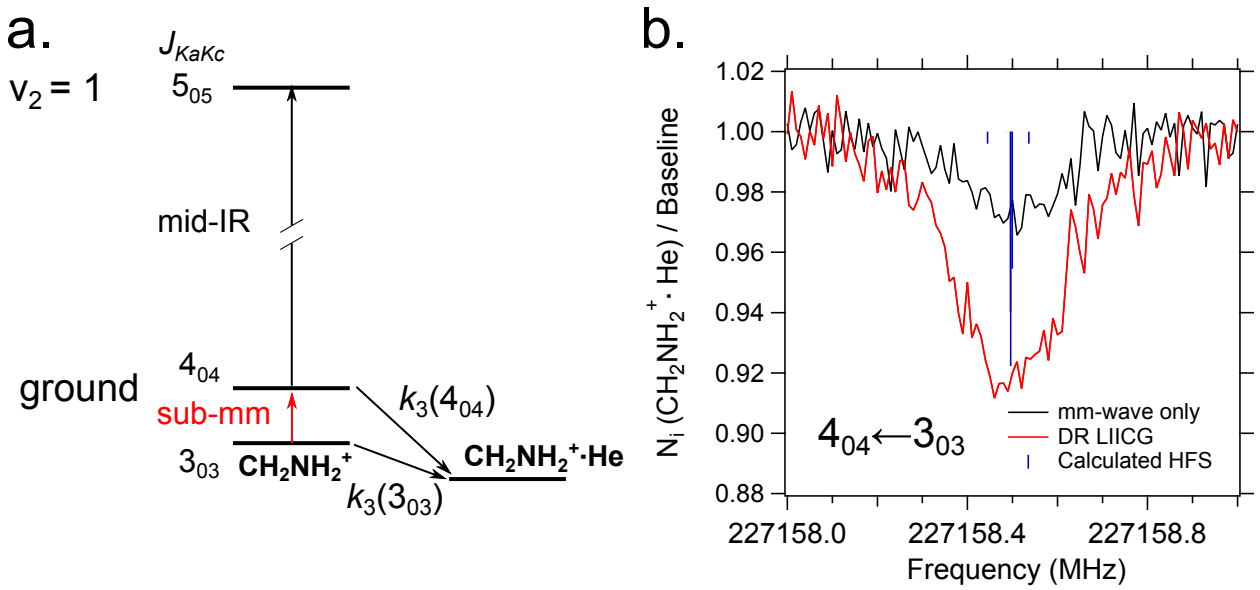

Figure 6.3: **a.** A simple diagram showing the transitions and tagging mechanism involved in the double resonance scheme, with the ternary association rate k_3. **b.** A comparison between scans of the $4_{04} \leftarrow 3_{03}$ transition taken with standard mm-wave only scheme (black) and double resonance using LIICG (red), which in this case was stronger by a factor of three. Hyperfine structure from the ^{14}N nucleus ($I = 1$) is indicated with blue sticks but was not resolved in the spectroscopic measurements. Each trace corresponds to a total integration time on the order of 1 hr.

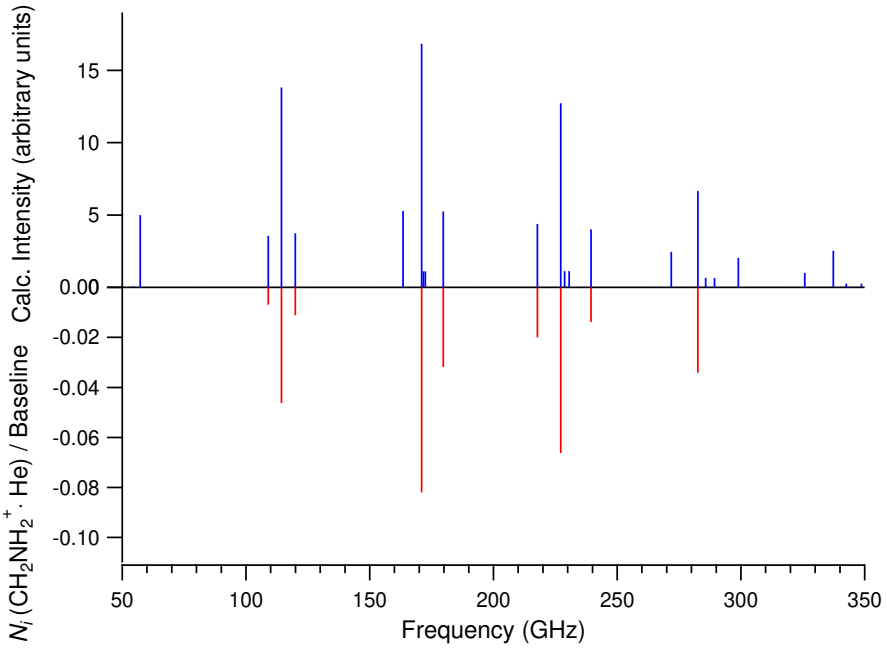

Figure 6.4: Stick spectra of pure rotational transitions of $CH_2NH_2^+$, with experimental values determined using DR shown in red and values from a PGOPHER simulation at 11 K shown in blue.

6.5 Spectroscopic parameters

The results of this work are currently the only high-resolution data available for $CH_2NH_2^+$. The frequencies of the rovibrational and pure rotational lines collected in Tables 6.2 and 6.3 were fit with a standard asymmetric rotor

Hamiltonian using the programs PGOPHER [165] and SPFIT [80]. Given that all transitions were a-type and the limited scope of the data set, the D_K and d_2 distortion constants could not be determined and were held to the calculated values. Due to the relatively large uncertainties of the rovibrational data, the distortion constants D_J, D_{JK}, and d_1 could not be determined for the ground and vibrationally excited states independently but a set of common constants for both states was used. The results of the fit are given in Table 6.4. Overall, 48 transitions were fit with 10 parameters, giving a reduced root mean square (RMS) error of 0.77 with $\mathrm{RMS_{mmw}}$=2 kHz and $\mathrm{RMS_{IR}}$=0.8 $\mathrm{cm^{-1}}$. The fit results are in very good agreement with the calculated values. The calculated and experimental ground rotational constants agree to better than 1 per mill and the calculated equilibrium centrifugal distortions terms and the experimentally derived ones to within 3 percent. The sets of calculated and experimental rotation-vibration interaction constants $\alpha_2^{A,B,C}$ are consistent in both sign and magnitude and agree to within a factor of two.

The molecular constants in Table 6.4 were also used to predict pure rotational transitions that were either outside of our mm-wave source's coverage or too weak to observe here, which are presented alongside the experimental values in Table 6.3. These include transitions up to $8_{17} \leftarrow 7_{16}$ with estimated uncertainties less than 200 kHz.

The inertial defect $\Delta_0 = I_c - I_b - I_a = 0.047\ \mathrm{u\,\AA^2}$ calculated from the ground state rotational constants in Table 6.4 is small and positive as typically observed in planar molecules of similar size [166]. Upon correction of the ground state rotational constants for the effects of zero-point vibration (using the calculated ΔA_0, ΔB_0, and ΔC_0 (Table 6.1) to derive semi-experimental (SE) equilibrium rotational constants), the inertial defect $\Delta_e^{\mathrm{SE}} = I_c^{\mathrm{SE}} - I_b^{\mathrm{SE}} - I_a^{\mathrm{SE}}$ is essentially zero, an indication that the vibrational contributions to the rotational constants are efficiently treated by the present theoretical approach.

6.6 Conclusion and outlook

The first high-resolution measurements of $CH_2NH_2^+$ have been performed in the infrared around 3 μm using LIICG. In total, 39 rovibrational transitions in the ν_2 C-H symmetric stretch fundamental band were measured with $\sim$ 30 MHz uncertainties and used to predict the pure rotational transitions in the ground vibrational state. This enabled the measurement of nine pure rotational transitions with $\sim$ 5 kHz uncertainties with the first demonstration of a double resonance scheme based on LIICG, which was found to generate signals 2 to 3 times stronger than standard mm-wave-only measurements applying the hindering of He-attachment at 4 K. The new measurements were fit to an effective Hamiltonian to calculate spectroscopic constants in order to accurately predict unobserved pure rotational transitions. These new measurements and predictions will enable astronomical searches for $CH_2NH_2^+$ in the ISM, where it is predicted to be an important precursor to the possible prebiotic molecule methanimine. Additionally, $CH_2NH_2^+$ is thought to play an important role in the formation of NH_3 in the upper atmosphere of Titan, and the

results from this work will allow for searches using remote sensing in the post-*Cassini* era. The close agreement of the experimental value for the origin of the weak ν_2 mode with theory provides some additional confidence that the predictions of the stronger ν_1, ν_8, and ν_9 modes could lead to a detection in Titan's atmosphere using past data from the *Cassini* Composite InfraRed Spectrometer, or in future observations by the Stratospheric Observatory for Infrared Astronomy (SOFIA) or the *James Webb Space Telescope* (*JWST*). In the laboratory, high-resolution spectroscopic detection of these infrared active vibrational modes should also be feasible using techniques similar to the ones used here. For example, it would be particularly worthwhile to characterize the strong N-H stretching modes ν_1 and ν_9 at high spectral resolution.

Low-resolution observations of the vibrational fundamentals using free electron lasers would be another promising future direction. There are seven IR active modes of $CH_2NH_2^+$ that have yet to be observed experimentally, which are located between 920 and 1705 cm^{-1}, a standard range for light sources like the Free Electron Laser for Infrared eXperiments [167] (FELIX, Nijmegen, The Netherlands). In a closely related project aimed at the spectroscopic characterization of new H_nCN^+ species we have recently studied protonated methylamine, $CH_3NH_3^+$, detecting vibrational bands at low resolution with the FELion instrument [168] connected to FELIX, and by high-resolution rotational spectroscopy in the millimeter wave range. A detailed analysis of this study will be given elsewhere.

The high sensitivity of the novel double resonance method will enable new investigations of systems for which the mm-wave-only method has failed up to date. Failed attempts include the rotational spectroscopy of O_2H^+ [142], as well as the accurately predicted transition $J = 2 - 1$ of SiH^+ [147] and the $2_0 - 1_0$ and $2_1 - 1_1$ transitions of the symmetric rotor NH_3D^+ [146, 148]. Another interesting case is the $N = 1 - 0$ transition of CO^+ ($^2\Sigma$), where only one fine structure component ($1_{3/2} - 0_{1/2}$) could be detected, but not the second component ($1_{1/2} - 0_{1/2}$) of that doublet [144]. Using the double resonance method, the robustness of the vibrational LIICG signal might permit pure rotational spectroscopy in these cases in the future.

Table 6.3: Frequencies of pure rotational transitions (in MHz) of $CH_2NH_2^+$. The uncertainty is given in parentheses in units of the least significant digit. The intensity is the depth of the transition relative to the baseline counts.

$J'_{Ka'Kc'} \leftarrow J''_{Ka''Kc''}$	Experimental	Predicted[a]	Obs - Calc. (kHz)	Intensity
$1_{01} \leftarrow 0_{00}$	···	57240.1544(8)	···	···
$2_{12} \leftarrow 1_{11}$	109041.7245(57)	109041.7245(55)	0.0	-0.007
$2_{02} \leftarrow 1_{01}$	114298.8800(15)	114298.8790(12)	1.0	-0.046
$2_{11} \leftarrow 1_{10}$	119914.0907(82)	119914.0960(53)	-5.3	-0.011
$3_{13} \leftarrow 2_{12}$	···	163449.6602(57)	···	···
$3_{03} \leftarrow 2_{02}$	170996.1120(23)	170996.1153(12)	-3.3	-0.082
$3_{22} \leftarrow 2_{21}$	···	171708.178(28)	···	···
$3_{21} \leftarrow 2_{20}$	···	172428.314(22)	···	···
$3_{12} \leftarrow 2_{11}$	179753.4859(57)	179753.4831(45)	2.8	-0.032
$4_{14} \leftarrow 3_{13}$	217727.2896(91)	217727.2897(88)	-0.1	-0.020
$4_{04} \leftarrow 3_{03}$	227158.4977(19)	227158.4965(15)	1.2	-0.066
$4_{23} \leftarrow 3_{22}$	···	228799.432(31)	···	···
$4_{22} \leftarrow 3_{21}$	···	230590.962(20)	···	···
$4_{13} \leftarrow 3_{12}$	239446.4259(91)	239446.4280(84)	-2.1	-0.014
$5_{15} \leftarrow 4_{14}$	···	271839.664(22)	···	···
$5_{05} \leftarrow 4_{04}$	282631.9019(47)	282631.9033(37)	-1.4	-0.034
$5_{24} \leftarrow 4_{23}$	···	285766.766(31)	···	···
$5_{23} \leftarrow 4_{22}$	···	289314.066(30)	···	···
$5_{14} \leftarrow 4_{13}$	···	298935.278(23)	···	···
$6_{16} \leftarrow 5_{15}$	···	325758.680(46)	···	···
$6_{06} \leftarrow 5_{05}$	···	337302.181(11)	···	···
$6_{25} \leftarrow 5_{24}$	···	342579.635(31)	···	···
$6_{24} \leftarrow 5_{23}$	···	348679.224(64)	···	···
$6_{15} \leftarrow 5_{14}$	···	358154.719(45)	···	···
$7_{17} \leftarrow 6_{16}$	···	379464.173(82)	···	···
$7_{07} \leftarrow 6_{06}$	···	391119.878(29)	···	···
$7_{26} \leftarrow 6_{25}$	···	399208.071(39)	···	···
$7_{25} \leftarrow 6_{24}$	···	408702.63(12)	···	···
$7_{16} \leftarrow 6_{15}$	···	417029.985(76)	···	···
$8_{18} \leftarrow 7_{17}$	···	432944.515(134)	···	···
$8_{08} \leftarrow 7_{07}$	···	444118.501(64)	···	···
$8_{27} \leftarrow 7_{26}$	···	455623.082(61)	···	···
$8_{26} \leftarrow 7_{25}$	···	469316.29(19)	···	···
$8_{17} \leftarrow 7_{16}$	···	475475.60(11)	···	···

[a] Prediction based on experimental ground state molecular constants given in Table 6.4

Table 6.4: A comparison between calculated and experimentally determined molecular constants. All values are in MHz unless otherwise stated. Uncertainties are given in parentheses in units of least significant digit, and if no uncertainty is provided the value was held to theoretical value.

	Ground state, $v = 0$			$v_2 = 1$		
	Calc. [134]	Calc. (this work)[a]	Experimental	Calc. [134]	Calc. (this work)	Experimental
ν (cm^{-1})	···	···	···	3009.9	3026.8[b]	3026.44493(30)
A	151697.1	151548.1	151415.3(13)	150378.3	150233.9[c]	150660.9(37)
B	31372.5	31342.6	31338.3840(27)	31327.6	31297.5[c]	31318.38(120)
C	25931.3	25906.1	25901.9333(24)	25859.7	25834.5[c]	25831.57(99)
D_J	0.041	0.0405	0.040752(76)[d]	···	···	0.040752(76)[d]
D_{JK}	0.35	0.3505	0.3551(15)[d]	···	···	0.3551(15)[d]
D_K	2.375	2.366	2.366[e]	···	···	2.366[e]
$d_1 \times 10^3$	-8.097	-8.067	-8.281(50)[d]	···	···	-8.281(50)[d]
$d_2 \times 10^3$	-1.559	-1.556	-1.556[e]	···	···	-1.556[e]
χ_{aa}(N)	···	0.126	···	···	···	···
χ_{bb}(N)	···	-0.104	···	···	···	···
χ_{cc}(N)	···	-0.022	···	···	···	···
α_2^A	···	···	···	1318.8	1314.2	754.4(35)
α_2^B	···	···	···	44.9	45.1	20.01(120)
α_2^C	···	···	···	71.6	71.7	70.36(99)
Δ_0 (uÅ^2)	···	···	0.047[f]	···	···	···
Δ_e^{SE} (uÅ^2)	···	···	-0.002[g]	···	···	···

[a] Ground state rotational constants calculated from CCSD(T)/cc-pwCV5Z equilibrium rotational constants and CCSD(T)/cc-pwCVQZ zero-point vibrational corrections; equilibrium centrifugal distortion constants and nuclear quadrupole coupling constants calculated at the CCSD(T)/cc-pwCVQZ and CCSD(T)/cc-pwCV5Z levels, respectively.

[b] CCSD(T)/cc-pwCVQZ.

[c] From calculated ground state rotational constants and CCSD(T)/cc-pwCVQZ vibration-rotation interaction constants.

[d] Shared constants for ground and $v_2 = 1$ states.

[e] Constrained to the values calculated at the CCSD(T)/cc-pwCVQZ level of theory.

[f] Inertial defect $\Delta_0 = I_c - I_b - I_a$, calculated from experimental ground state rotational constants.

[g] Inertial defect $\Delta_e^{\mathrm{SE}} = I_c^{\mathrm{SE}} - I_b^{\mathrm{SE}} - I_a^{\mathrm{SE}}$, calculated from experimental ground state rotational constants corrected for zero-point vibrational contributions.

Appendix A

Communication: High precision sub-Doppler infrared spectroscopy of the HeH^+ ion

This appendix is resproduced from Adam J. Perry, James N. Hodges, Charles R. Markus, G. Stephen Kocheril, and Benjamin J. McCall, The Journal of Chemical Physics, 141, (2014), 101101, with the permission of AIP Publishing.

Communication: High precision sub-Doppler infrared spectroscopy of the HeH^+ ion

Adam J. Perry,[1] James N. Hodges,[1] Charles R. Markus,[1] G. Stephen Kocheril,[1] and Benjamin J. McCall[1,2,a)]
[1]*Department of Chemistry, University of Illinois, Urbana, Illinois 61801, USA*
[2]*Departments of Astronomy and Physics, University of Illinois, Urbana, Illinois 61801, USA*

(Received 30 July 2014; accepted 28 August 2014; published online 9 September 2014)

The hydrohelium cation, HeH^+, serves as an important benchmark for *ab initio* calculations that take into account non-adiabatic, relativistic, and quantum electrodynamic effects. Such calculations are capable of predicting molecular transitions to an accuracy of ~300 MHz or less. However, in order to continue to push the boundaries on these calculations, new measurements of these transitions are required. Here we measure seven rovibrational transitions in the fundamental vibrational band to a precision of ~1 MHz using the technique of Noise Immune Cavity Enhanced Optical Heterodyne Velocity Modulation Spectroscopy. These newly measured transitions are included in a fit to the rotation-vibration term values to derive refined spectroscopic constants in the $v = 0$ and $v = 1$ vibrational states, as well as to calculate rotation-vibration energy levels with high precision.
 [http://dx.doi.org/10.1063/1.4895505]

I. INTRODUCTION

Composed of the two most abundant elements in the universe, the HeH^+ cation is predicted to be among the first molecules ever formed,[1,2] which makes this species of vital significance to chemical models of the early universe. Astronomical observations targeted at HeH^+ have yet to yield an unequivocal detection of this molecule. The difficulty in detecting this species is attributed to the many chemical processes that compete with the formation of HeH^+, ultimately resulting in a low abundance of this molecule. However, this molecule is easily formed in laboratory plasmas, which has spurred much experimental work on this fundamental species.

First discovered in 1925,[3] the HeH^+ ion has been the subject of many spectroscopic studies. In 1979, the first rovibrational spectrum of this molecule was acquired by Tolliver and co-workers, who observed the P(12) and P(13) lines in the fundamental vibrational band as well as the P(9)-P(11) transitions in the $v = 2 \leftarrow 1$ hot band with an accuracy of ~0.002 cm^{-1}.[4] In 1982, Bernath and Amano reported the first observation of the low J transitions in the fundamental band, covering the P(4)-R(4) rovibrational transitions.[5] After this work various studies of hot bands were published, including transitions from bound to quasibound states as well as quasibound to quasibound transitions.[6–8] In 1989, Crofton and co-workers measured a few new transitions in the fundamental band along with several lines in the $v = 2 \leftarrow 1$ hot band as well as in the fundamental bands of the $^3HeH^+$, $^4HeD^+$, and $^3HeD^+$ isotopologues.[9] Pure rotational studies were first carried out by Liu *et al.* where the $J = 7 \leftarrow 6$ transition was measured,[10] followed by the measurement of $J = 1 \leftarrow 0$ and $J = 2 \leftarrow 1$ by Matsushima *et al.*[11] as well as some low J rotational transitions of the $^3HeH^+$, $^4HeD^+$, and $^3HeD^+$ isotopologues. Higher J rotational transitions were measured by Liu and Davies[8,12] with J as high as 25.

From a theoretical standpoint the HeH^+ ion is a relatively simple species that is isoelectronic to H_2. This makes HeH^+ an important benchmark molecule for high-level *ab initio* calculations that take into account not only non-adiabatic corrections to the Born Oppenheimer approximation, but also relativistic and quantum electrodynamic (QED) effects. Recent *ab initio* calculations by Pachucki and Kosama,[13] which have treated the non-adiabatic corrections using Non-Adiabatic Perturbation Theory as well as the relativistic (α^2) and leading QED (α^3) corrections to the Born-Oppenheimer approximation, have been able to reproduce many experimentally measured rovibrational transitions with an accuracy on the order of 0.01 cm^{-1}(~300 MHz). This sort of accuracy is only currently achievable for a select few molecular systems, namely, H_2, H_2^+, H_3^+, and HeH^+.[13–17] In order to predict transition frequencies with accuracies on the level of 0.001 cm^{-1}or better for more complicated systems, it is imperative that the theoretical treatment of the aforementioned benchmark systems be well developed. Since theory must be informed by experiment to push the boundaries of these calculations, experimentalists need to provide highly accurate and precise measurements of molecular transitions for these species.

The HeH^+ molecule has also proven to be a useful benchmark system for theoretical treatments that go beyond the Born-Oppenheimer approximation.[18] These methods rely on using a set of correlated Gaussian functions that are functions of the separations between the nuclei and electrons, thus eliminating the traditional separation of the nuclear and electronic wavefunctions of the Born-Oppenheimer approximation. Within this framework the authors also developed algorithms for calculating the complete relativistic correction for this molecule.[19,20] To date, these sorts of calculations have

a)Electronic mail: bjmccall@illinois.edu

only been performed on states with no angular momentum (i.e., "rotationless" states).

Another approach has been to develop a global empirical potential that is based on the available spectroscopic data.[21] This work used all available spectroscopic data from all isotopomers in a fit to a modified Lennard-Jones potential that is able to provide the correct behavior at large internuclear separations near the dissociation limit. This approach also allows for experimental determination of the Born-Oppenheimer breakdown functions which showed reasonable agreement with a fitted theoretical potential based on the calculations of Bishop and Cheung.[22]

II. EXPERIMENTAL

The instrument used in this work has been described in detail in Ref. 23 and therefore will be described here only briefly. For this work, we used a technique that has been previously developed in our lab called Noise Immune Cavity Enhanced Optical Heterodyne Velocity Modulation Spectroscopy (NICE-OHVMS)[23–25] which combines the high sensitivity of Noise Immune Cavity Enhanced Optical Heterodyne Molecular Spectroscopy (NICE-OHMS)[26] with the ion/neutral discrimination of velocity modulation spectroscopy.[27]

The spectrometer is based on a commercially available continuous wave optical parametric oscillator (Aculight Argos 2400 SF) that is tunable across the 3.2–3.9 μm range. The pump laser (Koheras Adjustik Y-10) is phase modulated at a frequency of ~80 MHz to produce a pair of RF sidebands that are imprinted onto the idler wave. The idler wave is then coupled into an external optical cavity (finesse of ~150) which surrounds a liquid nitrogen cooled positive column discharge cell, in which ions of interest are produced from precursor gasses (a 2 Torr mixture of H_2 and He in a 1:100 ratio) and where their absorption profiles are velocity modulated. Light transmitted through the cavity is detected by a fast photodiode detector (Boston Electronics Vigo PVM-10.6-1×1), from which the signal is demodulated at the same frequency used to generate the 80 MHz sidebands, using a pair of frequency mixers that are 90° out of phase with one another. Further demodulation of the mixer outputs at twice the velocity modulation frequency (~80 kHz) is accomplished by a pair of lock-in amplifiers, which acts to recover the velocity modulation information.

Frequency calibration of our spectra was accomplished using an optical frequency comb (Menlo Systems FC-1500 with 100 MHz repetition rate) to measure the difference in frequency of the pump and signal beams at each point. Initial measurements of the frequencies of both beams (ten measurements for each) are performed using a near-infrared wavemeter (Burleigh WA-1500) to determine the mode number of the nearest comb tooth. The accuracy of the wavemeter was enhanced by measuring nearby reference lines of CH_4.[28] These reference line frequencies are all determined to within ~5 MHz and any systematic errors introduced by the wavemeter can be corrected to ensure that the proper comb mode numbers are determined.

III. RESULTS

Figure 1 shows a typical NICE-OHVMS spectrum of the P(1) transition of HeH^+ at 85258146.86(35) MHz. The lineshapes have an odd symmetry resulting from the heterodyne detection and velocity modulation schemes. The narrow features near the center of the lines are blends of several individual Lamb dips that are spaced by half-integer multiples of the heterodyne frequency about the center of the transition. To extract the transition line centers, we fit the data from all four of the detection channels simultaneously (Figure 2) with some shared parameters between the data channels such as the line center, full-width of the blended feature, and the heterodyne detection angle. Further information regarding the fitting routines has been given by Hodges *et al.*[23]

Table I shows that our measurements exhibit good agreement with the values measured by Bernath and Amano as all measured transitions lie within or only slightly outside their 30–60 MHz claimed uncertainties. However, in this work we

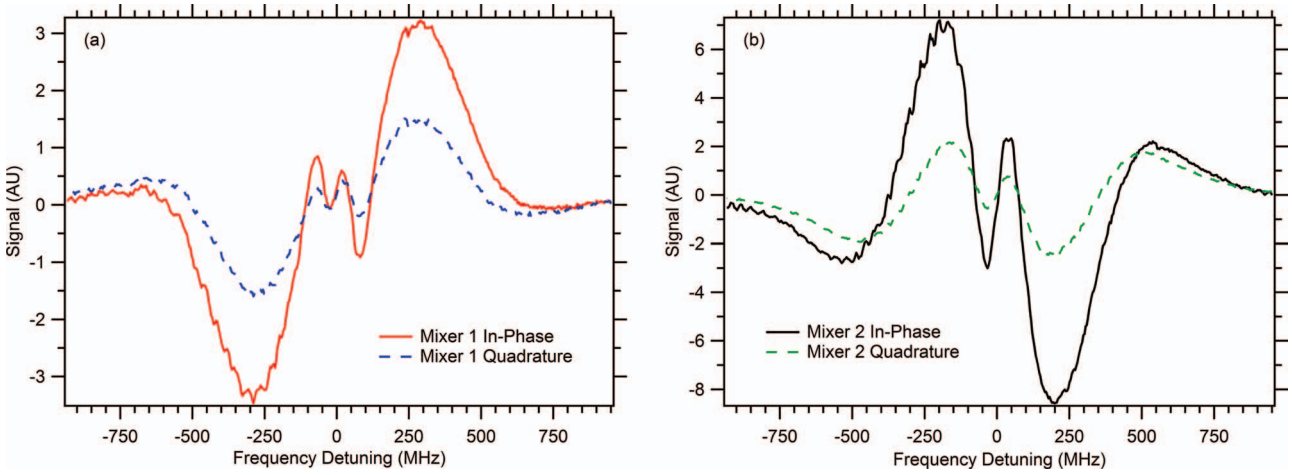

FIG. 1. Typical NICE-OHVMS scan of the P(1) fundamental band transition of HeH^+ showing the central Lamb dip feature sitting on top of the Doppler profile of the line. Signals from each of the four detection channels are shown with the in-phase (red solid trace) and quadrature (blue dashed trace) channels from mixer 1 plotted in panel (a) and the in-phase (black solid trace) and quadrature (green dashed trace) channels of mixer 2 in panel (b).

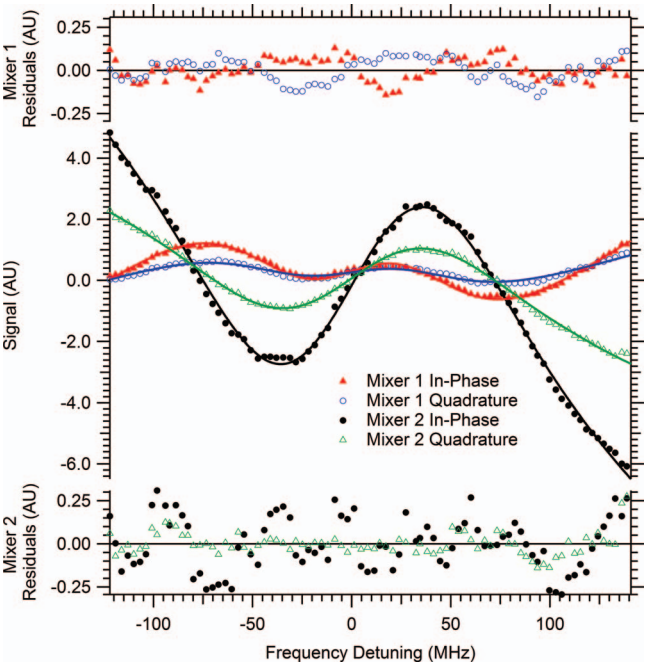

FIG. 2. Frequency comb calibrated scan of the central sub-Doppler Lamb dip feature in the P(1) rovibrational transition of HeH^+, along with a simultaneous fit of all four data acquisition channels. Colored markers represent the experimental data, while the colored solid traces show the fit of the data to the equation outlined in Hodges *et al.*[23] Fit residuals from each detection channel are plotted on the upper (channels from mixer 1) and lower (channels from mixer 2) axes. For clarity, only every third data point is shown.

have improved the precision on these measurements by two orders of magnitude. For all of the measurements we were able to obtain precisions on the order of 1 MHz for the line centers due to both our ability to saturate the transitions which allows us to fit the relatively narrow sub-Doppler features, and the frequency calibration provided by the optical frequency comb which allows us to go far beyond the typical tens of MHz measurement uncertainty provided by mid-infrared wavemeters and Doppler-broadened reference gas lines.

These new measurements together with all available data for the fundamental band[4,5,7,9] as well as pure rotational data[8,10,11] were included in a fit to a power-series expansion of the vibration-rotation term values for a $^1\Sigma$ linear molecule as shown in Eq. (1) [The measurements of P(9)-P(11) by Purder *et al.* were not included in the fit as no uncertainties were

TABLE I. All measured rovibrational transitions in the fundamental vibrational band of HeH^+ and a comparison to those values measured by Bernath and Amano.[5] All units are in MHz.

Transition	Freq.	St. Dev.	Prev. value[5]	Diff.
P(3)	80795499.88	0.99	80795566.39	− 66.51
P(2)	83096617.69	1.34	83096650.39	− 32.69
P(1)	85258146.86	0.35	85258082.06	64.80
R(0)	89115533.66	1.38	89115502.62	31.04
R(1)	90788380.66	0.40	90788398.50	− 17.84
R(2)	92275879.63	0.77	92275875.74	3.89
R(3)	93567523.38	0.92	93567519.55	3.82

TABLE II. Rovibrational parameters from a fit of experimentally measured rotation and rovibration transitions to Eq. (1). All units are in MHz.

Parameter	This work	Liu and Davies[8]
ν_0	87268330.62(54)	87268319(33)
B_0	1006063.39(15)	1006063.3(45)
D_0	486.1762(187)	486.512(96)
H_0	0.1807358(2628)	0.18428(84)
$L_0 \times 10^4$	−1.17975(1418)	−1.331(36)
$M_0 \times 10^7$	0.73228(3114)	1.022(69)
$N_0 \times 10^{10}$	−0.49376(2392)	−0.702(48)
B_1	924550.54(17)	924554.8(45)
D_1	475.1636(138)	475.606(99)
H_1	0.1660888(3241)	0.17049(84)
$L_1 \times 10^4$	−1.31950(2056)	−1.499(33)
$M_1 \times 10^7$	1.05510(4957)	1.385(60)
$N_1 \times 10^{10}$	−1.12488(4121)	−1.352(42)

reported],[29]

$$F_v = G_v + B_v J(J+1) - D_v[J(J+1)]^2 + H_v[J(J+1)]^3 + L_v[J(J+1)]^4 + M_v[J(J+1)]^5 + N_v[J(J+1)]^6. \quad (1)$$

The fit was performed using PGOPHER,[30] floating all parameters in both the ground and first excited vibrational states. In addition to our high-precision rovibrational measurements and the remaining fundamental band data, the fit includes the two pure rotational transitions (J = 1 ← 0 and J = 2 ← 1) measured by Matsushima *et al.* with very high precision (∼200 kHz), as well as the pure rotational transitions of Liu and Davies, which includes 11 transitions in both the v = 0 and v = 1 vibrational states covering a range of J″ from 10 to 20. Parameters from the fit are given in Table II along with a comparison to those values obtained by Liu and Davies.[8] Full details of the fit can be found in the supplementary material.[31] Inclusion of these high precision measurements allows for a more precise determination (by roughly an order of magnitude) of the band origin as well as the B rotational constants and the lower order centrifugal distortion terms up to H.

It is interesting to note that for all the centrifugal distortion terms there are significant differences between our values and those of Liu and Davies. However, the results of the fit showed that the weighted residuals were randomly distributed across the entire range of J″, which suggests that the differences in the fit parameters may be due to a high degree of correlation among the higher order parameters. Indeed, when the correlation matrix is examined it is clear that this is the case as the H, L, M, and N parameters all show correlations of ≥ 0.9 with each other.

Another comparison can be made to the fit produced by Matsushima *et al.*[11] In their fit they only included their J = 1 ← 0 and J = 2 ← 1 transitions along with the available rovibrational data in the fundamental band, while only including terms up to L (the values of L were fixed to the *ab initio* predictions of Bishop and Cheung[22]). By doing so they were able to obtain very precise values for the B, D, and H values, which are nearly an order of magnitude more precise

TABLE III. Experimentally determined rotation-vibration energy levels E(v,J) for $^4HeH^+$. All units are in MHz.

J	E(0,J)	E(1,J)
0	0	87268330.76(41)
1	2010183.86(20)	89115533.7(14)
2	6018916.87(28)	92798564.52(44)
3	12003064.7(11)	98294796.51(83)
4	19928164(60)	105570588.0(14)
5	29749118(30)	114581537(85)
6	41409933(172)	125273098(153)
7	54845432(194)	137580625(228)
8		151431127(245)

than the values reported in Table II. It may be the case, however, that the quality of their fit was somewhat fortuitous, due to the weighting of the highly precise values for the rotational transitions and their influence on the values of the lower order rotational parameters. We conjecture that since these lower order parameters were tightly constrained by only two transitions, their fit may have yielded well-determined parameters because there was so much more relative uncertainty in the rovibrational transition frequencies. The inclusion of our data, which also probe the J = 0, 1, and 2 levels in the ground vibrational state and carry a similar weighting in the fit as Matsushima's rotational transitions, may explain the apparent increase in the uncertainty of our parameters.

To further assess the accuracy of our measurements we performed a test by adding Gaussian noise of varying amounts (as determined by the standard deviation of this added noise) to our transition frequencies and running the fit described above using these modified frequencies. For noise with a standard deviation of 2 MHz we begin to see a noticeable degradation in the quality of the fit in terms of the residuals of our seven measured transitions. With this amount of "noise" we find that the RMS of the residuals for these seven transitions increases by roughly a factor of two. Though this test may not be 100% conclusive due to the random nature of adding in this noise, it does give us confidence that our claimed uncertainties are appropriate in size.

Using these new data along with previous infrared and pure rotational work, a set of experimentally determined rovibrational energy levels can be derived using a combination difference analysis. Evaluating the energy levels in this way is advantageous because they are not based on any model Hamiltonian. The energy levels covering J = 0–7 in the vibrational ground state and J = 0–8 in the v = 1 vibrational excited state can be computed based on the available spectroscopic data. Table III summarizes the results.

The high precision (no larger than 1.4 MHz) of the J = 3 level in the ground vibrational state and the first five rotational levels in the v = 1 vibrational state, will allow these energy levels to serve as excellent benchmark values for new *ab initio* calculations on this molecule.

IV. CONCLUSION

We have performed sub-Doppler mid-infrared spectroscopy on the HeH^+ cation. By using the technique of NICE-OHVMS in conjunction with frequency calibration provided by an optical frequency comb, we have re-measured seven fundamental band transitions of this molecule with a precision on the order of 1 MHz, and were able to achieve sub-MHz precision on most of the measured transitions. Using these new transitions with their improved uncertainties we have improved the values of the band origin as well as the B rotational constants and the lower order centrifugal distortion terms in a fit that includes all available spectroscopic data for the v = 0 and v = 1 states of the $^4HeH^+$ molecule. These new measurements also allowed for very precise determination of the low J rotation-vibration energy levels in the ground and v = 1 states, which will serve as new benchmarks for theorists to test *ab initio* calculations as higher level non-adiabatic, relativistic, and QED corrections are included. These measurements could also be used in a refinement of the empirical potential originally published by Coxon and Hajigergiou.[21]

ACKNOWLEDGMENTS

We would first like to acknowledge financial support from the National Science Foundation (CHE 12-13811). A.J.P., J.N.H., and C.R.M. are grateful to Mr. Paul A. Jenkins II for his assistance with setting up the spectrometer. J.N.H. is thankful for support from an NSF Graduate Research Fellowship (DGE 11-44245 FLLW). G.S.K. is thankful for financial support from a Gieseking scholarship. We would especially like to express gratitude to Professor Takeshi Oka for providing the glass discharge cell (Black Widow) along with the associated pumps and electronics.

[1]S. Lepp, P. C. Stancil, and A. Dalgarno, J. Phys. B **35**, R57 (2002).
[2]S. Lepp, Astrophys. Space Sci. **285**, 737 (2003).
[3]T. R. Hogness and E. G. Lunn, Phys. Rev. **26**, 44 (1925).
[4]D. E. Tolliver, G. A. Kyrala, and W. H. Wing, Phys. Rev. Lett. **43**, 1719 (1979).
[5]P. Bernath and T. Amano, Phys. Rev. Lett. **48**, 20 (1982).
[6]A. Carrington, R. A. Kennedy, T. P. Softley, P. G. Fournier, and E. G. Richard, Chem. Phys. **81**, 251 (1983).
[7]C. E. Blom, K. Möller, and R. R. Filgueira, Chem. Phys. Lett. **140**, 489 (1987).
[8]Z. Liu and P. B. Davies, J. Chem. Phys. **107**, 337 (1997).
[9]M. W. Crofton, R. S. Altman, N. N. Haese, and T. Oka, J. Chem. Phys. **91**, 5882 (1989).
[10]D.-J. Liu, W.-C. Ho, and T. Oka, J. Chem. Phys. **87**, 2442 (1987).
[11]F. Matsushima, T. Oka, and K. Takagi, Phys. Rev. Lett. **78**, 1664 (1997).
[12]Z. Liu and P. B. Davies, Phys. Rev. Lett. **79**, 2779 (1997).
[13]K. Pachucki and J. Komasa, J. Chem. Phys. **137**, 204314 (2012).
[14]J. Komasa, K. Piszczatowski, G. Łach, M. Przybytek, B. Jeziorski, and K. Pachucki, J. Chem. Theory Comput. **7**, 3105 (2011).
[15]R. E. Moss, J. Phys. B **32**, L89 (1999).
[16]L. Lodi, O. L. Polyansky, J. Tennyson, A. Alijah, and N. F. Zobov, Phys. Rev. A **89**, 032505 (2014).
[17]W.-C. Tung, M. Pavanello, and L. Adamowicz, J. Chem. Phys. **137**, 164305 (2012).
[18]M. Stanke, D. Kędziera, M. Molski, S. Bubin, M. Barysz, and L. Adamowicz, Phys. Rev. Lett. **96**, 233002 (2006).
[19]S. Bubin, M. Stanke, D. Kędziera, and L. Adamowicz, Phys. Rev. A **76**, 022512 (2007).
[20]M. Stanke, D. Kędziera, S. Bubin, and L. Adamowicz, Phys. Rev. A **77**, 022506 (2008).
[21]J. A. Coxon and P. G. Hajigeorgiou, J. Mol. Spectrosc. **193**, 306 (1999).

[22]D. M. Bishop and L. M. Cheung, J. Mol. Spectrosc. **75**, 462 (1979).
[23]J. N. Hodges, A. J. Perry, P. A. Jenkins, B. M. Siller, and B. J. McCall, J. Chem. Phys. **139**, 164201 (2013).
[24]B. M. Siller, M. W. Porambo, A. A. Mills, and B. J. McCall, Opt. Exp. **19**, 24822 (2011).
[25]K. N. Crabtree, J. N. Hodges, B. M. Siller, A. J. Perry, J. E. Kelly, P. A. Jenkins, and B. J. McCall, Chem. Phys. Lett. **551**, 1 (2012).
[26]J. Ye, L.-S. Ma, and J. L. Hall, J. Opt. Soc. Am. B **15**, 6 (1998).
[27]C. S. Gudeman, M. H. Begemann, J. Pfaff, and R. J. Saykally, Phys. Rev. Lett. **50**, 727 (1983).
[28]L. S. Rothman, I. E. Gordon, Y. Babikov, A. Barbe, D. Chris Benner, P. F. Bernath, M. Birk, L. Bizzocchi, V. Boudon, L. R. Brown, A. Campargue, K. Chance, E. A. Cohen, L. H. Coudert, V. M. Devi, B. J. Drouin, A. Fayt, J.-M. Flaud, R. R. Gamache, J. J. Harrison, J.-M. Hartmann, C. Hill, J. T. Hodges, D. Jacquemart, A. Jolly, J. Lamouroux, R. J. Le Roy, G. Li, D. A. Long, O. M. Lyulin, C. J. Mackie, S. T. Massie, S. Mikhailenko, H. S. P. Müller, O. V. Naumenko, A. V. Nikitin, J. Orphal, V. Perevalov, A. Perrin, E. R. Polovtseva, C. Richard, M. A. H. Smith, E. Starikova, K. Sung, S. Tashkun, J. Tennyson, G. C. Toon, Vl. G. Tyuterev, and G. Wagner, J. Quant. Spectrosc. Radiat. Transf. **130**, 4 (2013).
[29]J. Purder, S. Civiš, C. E. Blom, and M. C. van Hemert, J. Mol. Spectrosc. **153**, 701 (1992).
[30]C. M. Western, PGOPHER, a Program for Simulating Rotational Structure, University of Bristol, http://pgopher.chm.bris.ac.uk.
[31]See supplementary material at http://dx.doi.org/10.1063/1.4895505 for the fit details of each experimentally measured transition.

Appendix B

High-precision R-branch transition frequencies in the ν_2 fundamental band of H_3^+

Journal of Molecular Spectroscopy 317 (2015) 71–73

Contents lists available at ScienceDirect

Journal of Molecular Spectroscopy

journal homepage: www.elsevier.com/locate/jms

Note

High-precision *R*-branch transition frequencies in the ν_2 fundamental band of H_3^+

Adam J. Perry [a], James N. Hodges [a], Charles R. Markus [a], G. Stephen Kocheril [a], Benjamin J. McCall [a,b,*]

[a] Department of Chemistry, University of Illinois, Urbana, IL 61801, USA
[b] Department of Astronomy, University of Illinois, Urbana, IL 61801, USA

ARTICLE INFO

Article history:
Received 10 July 2015
In revised form 4 September 2015
Available online 11 September 2015

Keywords:
Rovibrational spectroscopy
High-precision spectroscopy
Sub-Doppler spectroscopy
Ion spectroscopy
H_3^+

ABSTRACT

The H_3^+ molecular ion has served as a long-standing benchmark for state-of-the-art *ab initio* calculations of molecular potentials and variational calculations of rovibrational energy levels. However, the accuracy of such calculations would not have been confirmed if not for the wealth of spectroscopic data that has been made available for this molecule. Recently, a new high-precision ion spectroscopy technique was demonstrated by Hodges et al., which led to the first highly accurate and precise (~MHz) H_3^+ transition frequencies. As an extension of this work, we present ten additional *R*-branch transitions measured to similar precision as a next step toward the ultimate goal of producing a comprehensive high-precision survey of this molecule, from which rovibrational energy levels can be calculated.

As the simplest polyatomic molecule, H_3^+ serves as an important benchmark system for *ab initio* calculation of molecular potential energy surfaces (PES) and spectra. The degree to which state-of-the-art calculations of the rovibrational transitions agree with experimental measurements is impressive, and is approaching the limit of the experimental uncertainty, typically on the order of 150–300 MHz (for a thorough review on previous laboratory spectroscopy of H_3^+ see Ref. [1]). Recent calculations [2] based on the highly accurate Born–Oppenheimer PES of Pavanello et al. [3], which included diagonal Born–Oppenheimer corrections (*i.e.* the adiabatic correction) and relativistic corrections, reproduce all known rovibrational energy levels for all isotopologues within 0.2 cm^{-1}. Shortly thereafter, Diniz et al. [4] developed a method for approximating the non-adiabatic effects using a "core-mass" approach whereby the nuclei are given coordinate-dependent masses as they undergo vibrational motion. Comparison to twelve high-precision (~10 MHz) transitions arising from low-lying rovibrational energy levels yields an agreement between experiment and theory of ~0.001 cm^{-1} (~30 MHz). Beyond these calculations Lodi and co-workers [5] have developed the first quantum electrodynamic correction surface for H_3^+, which demonstrated the importance of including these effects, as well as the need for a more complete model for taking into account non-adiabatic effects.

Since the accuracy of theoretical calculations is now reaching the level of the experimental uncertainty, improved spectroscopic measurements are needed in order to push the bounds of theoretical calculations. In this note we present ten new high-precision spectroscopic measurements in the ν_2 fundamental band of H_3^+. These new frequencies, combined with those measured by Hodges et al. [6], represent a step towards completing a thorough high-precision spectroscopic survey for this important fundamental species. The spectra were acquired using the technique Noise-Immune Cavity Enhanced Optical Heterodyne Velocity Modulation Spectroscopy (NICE-OHVMS), in which traditional velocity modulation spectroscopy [7] is augmented with cavity enhancement and heterodyne modulation [8]. The instrument (described in detail in [6,9]) utilizes a high-power, continuous wave, optical parametric oscillator whose idler beam is coupled into an external optical cavity which surrounds a water-cooled AC positive column discharge of H_2 gas. Inside the cell, the pressure is maintained at 300–400 mTorr and the discharge is driven at frequencies of 40–50 kHz. Light transmitted through the cavity is detected by a fast photodiode detector whose signal is demodulated first at the heterodyne frequency (~80 MHz) by a pair of electronic mixers and then again at twice the discharge frequency (80–100 kHz) by a pair of lock-in amplifiers. This detection scheme results in four channels of detection, producing signals from each heterodyne mixer that are in-phase and 90° out of phase (in quadrature) with the sinusoidal driving voltage of the discharge. Frequency calibration of the spectra is accomplished by measuring the difference in frequency between the pump and signal waves. Measurements of these beams are obtained with a near-infrared wavelength meter and optical frequency comb.

* Corresponding author at: Department of Chemistry, University of Illinois, Urbana, IL 61801, USA.

http://dx.doi.org/10.1016/j.jms.2015.09.004
0022-2852/

Due to the bi-directional nature and optical power enhancement of the external optical cavity, it is possible to perform sub-Doppler spectroscopy which enables high-precision line center measurements. Such a spectrum is illustrated in Fig. 1. Line centers are extracted via a simultaneous fit of all four detection channels to the sub-Doppler features. In the fit the line center, heterodyne detection angle, and full-width of the feature are all shared parameters between the four channels. Previous high-precision measurements were limited to transitions from lower-J levels and these new measurements have expanded the range up to $J = 6$. All newly measured transition frequencies are reported in Table 1. Uncertainties in the line centers are assigned as the standard deviation of a data set composed of at least five scans for each transition, and as a result are highly dependent on the signal-to-noise ratio of the sub-Doppler features. The precision to which these lines have been measured represents an improvement over previous measurements of two orders of magnitude for most of the transitions. It is worth noting that the works of Oka [10], and Lindsay et al. [1] appear to be highly accurate, and their claimed uncertainties may be a bit conservative.

The only new measurement that falls outside of the stated uncertainties of the previous work is that of $R(3,3)^u$, for which we record a frequency that is 15 MHz lower than that reported by Wu et al. [11]. Though this discrepancy is not completely unreasonable (1.5σ), we set out to confirm this frequency by performing a second, independent measurement of this transition. Doing so yielded the same value (to within our specified uncertainty). To eliminate any possibility of an unexpected systematic error in our frequency calibration, we immediately remeasured the $R(1,0)$ transition, which was in good agreement with Hodges et al. and Wu et al., and we still obtain the same value for its line center. These tests leave us confident in the accuracy of our $R(3,3)^u$ measurement.

Table 1
Newly measured rovibrational transitions in the ν_2 fundamental band of H_3^+ and a comparison to previous values. All units are in MHz.

Transition[a]	This work	Previous	Diff.
$R(4,3)^l$	86778433.66(76)	86778225(300)[b]	208.66
$R(3,3)^u$	87480191.43(117)	87480207(10)[c]	−15.57
$R(3,2)^u$	87640201.59(254)	87640158(300)[b]	43.59
$R(3,1)^u$	87789812.71(130)	87789754(300)[b]	58.71
$R(3,0)$	87844195.67(122)	87844077(300)[b]	118.67
$R(5,5)^l$	88620962.34(144)	88620809(300)[b]	153.34
$R(6,6)^l$	90368280.18(102)	90368359(150)[d]	−78.82
$R(4,3)^u$	90394720.09(232)	90394651(150)[d]	69.09
$R(4,2)^u$	90673895.29(179)	90673968(300)[d]	−72.71
$R(4,1)^u$	90831978.56(177)	90832078(150)[d]	−99.44

[a] Labels for these transitions refer to (J,G); for more details on H_3^+ notation see [1].
[b] Ref. [10].
[c] Ref. [11].
[d] Ref. [12].

Work is now underway to extend the frequency coverage of the spectrometer which will allow us to measure P and Q branch transitions in this band. Once this is accomplished it will be possible to begin measuring energy level spacings in the ground vibrational state with precision that has never before been achieved. Upon completion of the fundamental band measurements, a survey of transitions in the $2\nu_2^{\ell=2} \leftarrow \nu_2$ hot band along with transitions in the first overtone band ($2\nu_2^{\ell=2} \leftarrow 0$) will allow us to determine relative energy spacings among levels within the *ortho* and *para* species. Finally, a fit of the ground state energy levels to a modified Watson-type Hamiltonian will allow for absolute energy levels to be extracted. Once completed this work will equip theorists with a complete and highly precise list of experimentally determined

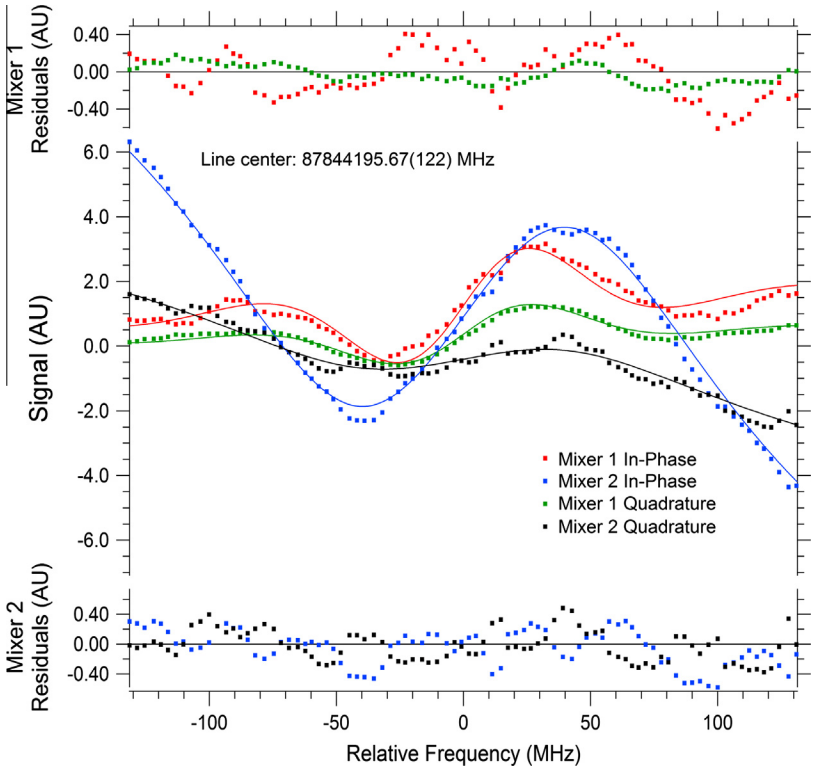

Fig. 1. A NICE-OHVMS scan of sub-Doppler feature of the $R(3,0)$ fundamental band transition of H_3^+ centered at 87844195.67(122) MHz. Signals from each of the four detection channels are shown (dots) and are fitted simultaneously (solid traces) with the line center as a shared parameter. The odd symmetry of the line shapes is a result of the applied modulation scheme.

rovibrational energy levels for this critically important molecular system.

Acknowledgments

This work was funded by the National Science Foundation (PHY 14-04330). J.N.H. is grateful for support from an NSF Graduate Research Fellowship (DGE 11-44245 FLLW). G.S.K. is thankful for financial support from a Gieseking scholarship.

References

[1] C. Lindsay, B.J. McCall, J. Mol. Spectrosc. 210 (2001) 60–83.
[2] O.L. Polyansky, A. Alijah, N.F. Zobov, I.I. Mizus, R.I. Ovsyannikov, J. Tennyson, L. Lodi, T. Szidarovszky, A.G. Császár, Philos. Trans. A Math. Phys. Eng. Sci. 370 (2012) 5014–5027.
[3] M. Pavanello, L. Adamowicz, A. Alijah, N.F. Zobov, I.I. Mizus, O.L. Polyansky, J. Tennyson, T. Szidarovszky, A.G. Császár, J. Chem. Phys. 136 (2012) 184303.
[4] L.G. Diniz, J.R. Mohallem, A. Alijah, M. Pavanello, L. Adamowicz, O.L. Polyansky, J. Tennyson, Phys. Rev. A 88 (2013) 032506.
[5] L. Lodi, O.L. Polyansky, J. Tennyson, A. Alijah, N.F. Zobov, Phys. Rev. A 89 (2014) 032505.
[6] J.N. Hodges, A.J. Perry, P.A. Jenkins II, B.M. Siller, B.J. McCall, J. Chem. Phys. 139 (2013) 164201.
[7] C. Gudeman, M. Begemann, J. Pfaff, R. Saykally, Phys. Rev. Lett. 50 (1983) 727–731.
[8] B.M. Siller, M.W. Porambo, A.A. Mills, B.J. McCall, Opt. Express 19 (2011) 24822–24827.
[9] K.N. Crabtree, J.N. Hodges, B.M. Siller, A.J. Perry, J.E. Kelly, P.A. Jenkins II, B.J. McCall, Chem. Phys. Lett. 551 (2012) 1–6.
[10] T. Oka, Philos. Trans. R. Soc. A 303 (1981) 543–549.
[11] K.-Y. Wu, Y.-H. Lien, C.-C. Liao, Y.-R. Lin, J.-T. Shy, Phys. Rev. A 88 (2013) 032507.
[12] C. Lindsay, R.M. Rade, T. Oka, J. Mol. Spectrosc. 210 (2001) 51–59.

Appendix C

Extended sub-Doppler resolution spectroscopy of the ν_3 band of methane

Journal of Quantitative Spectroscopy & Radiative Transfer 215 (2018) 9–12

Contents lists available at ScienceDirect

Journal of Quantitative Spectroscopy & Radiative Transfer

journal homepage: www.elsevier.com/locate/jqsrt

Extended sub-Doppler resolution spectroscopy of the ν_3 band of methane

Philip A. Kocheril[a], Charles R. Markus[a], Anne Marie Esposito[a], Alex W. Schrader[a], Thomas S. Dieter[b,1], Benjamin J. McCall[a,b,c,*]

[a] Department of Chemistry, University of Illinois at Urbana-Champaign, Urbana, IL 61801, USA
[b] Department of Physics, University of Illinois at Urbana-Champaign, Urbana, IL 61801, USA
[c] Department of Astronomy, University of Illinois at Urbana-Champaign, Urbana, IL 61801, USA

ARTICLE INFO

Article history:
Received 5 April 2018
Revised 29 April 2018
Accepted 30 April 2018
Available online 30 April 2018

Keywords:
Methane
Mid-infrared
Sub-Doppler

ABSTRACT

We have performed sub-Doppler resolution rovibrational spectroscopy of the ν_3 band of methane ($^{12}CH_4$) in the mid-infrared using an optical parametric oscillator in a double-pass configuration for saturated absorption. An optical frequency comb was used for absolute frequency calibration. We have measured 22 methane line centers ranging from the $P(13)$ to $R(10)$ transitions with a typical uncertainty of 0.40 MHz. These measurements improve previously known transition frequencies by at least an order of magnitude.

1. Introduction

Methane is a historically important molecule of study for scientists in many fields. Methane provided a fundamental guidepost for understanding molecular geometry and chemical bonding [1]. As the simplest stable hydrocarbon, methane has been and continues to be a key benchmark for molecular modeling and state-of-the-art *ab initio* calculations of potential energy and dipole moment surfaces [2,3]. Modern *ab initio* work is useful for predicting line strengths and supplementing incomplete experimental spectra, which can contribute to spectroscopic linelists like the HITRAN database [4]. Similarly, methane is relevant to the ExoMol project, which is focused on creating accurate astrophysical models of cool stars and extrasolar planets [5], since methane is a key constituent of planetary atmospheres [6,7] and brown dwarf atmospheres [8]. Here on Earth, methane is the third most abundant greenhouse gas and therefore a significant contributor to climate change [9], as well as being relevant to ozone depletion and formation [10].

Methane's rovibrational structure is best studied by mid-infrared spectroscopy due to its strong rovibrational transition dipole moments. However, its tetrahedral symmetry and overlap of normal mode frequencies for its four vibrational bands result in a highly complex vibrational structure. Specifically, the ν_1 and ν_3 bands consisting of C-H stretching vibrations have normal mode frequencies of roughly 3000 cm^{-1}, while the ν_2 and ν_4 bands consisting of C-H bending vibrations have normal mode frequencies of roughly 1500 cm^{-1} [11]. The vibrational bands of methane are grouped into polyads, which are named by the number of interacting bands, including fundamental, overtone, combination, and hot bands, in a given frequency region; the polyads increase in complexity with frequency, making assignment and analysis of the near-infrared and above very difficult.

The pentad region ($\nu_1, \nu_3, \nu_2+\nu_4, 2\nu_2, 2\nu_4$; 2300–3300 cm^{-1}) has been modeled with high accuracy in the past [2,3,12,13]. Agreement between theory and experiment now surpasses 0.1 cm^{-1} in the pentad region [2], and will likely soon surpass Doppler-limited precision. In order to continue to provide accurate benchmarks for *ab initio* calculations, line centers must be determined to sub-Doppler uncertainty. Moreover, methane is worth revisiting now due to the advent of more sophisticated techniques and widely tunable high-power mid-infrared light sources during the past few decades, which allow for much higher precision and accuracy in determining line centers.

Sub-Doppler spectroscopy overcomes the limitation of Doppler broadening from traditional spectroscopy. One method of performing sub-Doppler spectroscopy involves the use of a double-pass configuration, where the incident beam serves to saturate the transition, and the reflected beam probes the change in population. When a transition is saturated, a narrow dip in the absorption of the reflected beam is observed. This feature, known as a Lamb dip, is centered at the transition frequency, since it occurs when

* Corresponding author.
E-mail address: bjmccall@illinois.edu (B.J. McCall).
[1] Current address: Cymer, Inc., 17075 Thornmint Court, San Diego, CA 92127, USA.

https://doi.org/10.1016/j.jqsrt.2018.04.033
0022-4073/

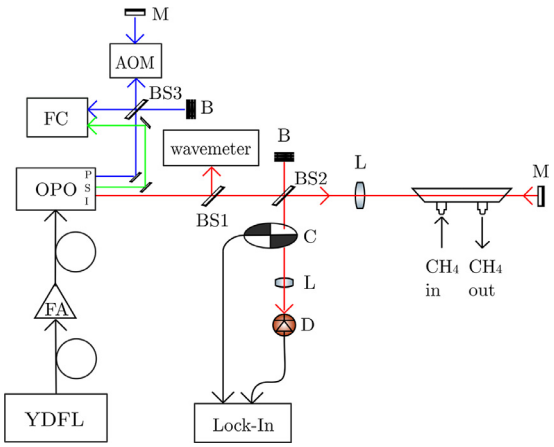

Fig. 1. Experimental layout. YDFL: ytterbium-doped fiber laser, FA: fiber amplifier, OPO: optical parametric oscillator, BS1: 99/1 beamsplitter, BS2: 50/50 beamsplitter, B: beam block, L: lens, M: back-reflecting mirror, C: beam chopper, D: detector, BS3: 70/30 beamsplitter, AOM: acousto-optic modulator, and FC: frequency comb.

the counter-propagating beams interact with the same molecules, thereby overcoming Doppler broadening. Lamb dip widths are also roughly two orders of magnitude narrower than a traditional Doppler-broadened profile, since Lamb dips are limited only by the homogeneous line width. When combined with the highly stable frequency calibration provided by an optical frequency comb, sub-Doppler spectroscopy allows for precise and accurate determination of transition frequencies.

The ν_3 band of methane has been studied quite extensively in Doppler-limited surveys using Fourier transform infrared (FTIR) spectroscopy [13–15] with uncertainties ranging from 3 to 300 MHz and dual-comb spectroscopy [16] where sub-MHz uncertainties were achieved. More recently, several groups have turned to saturation using difference frequency generation sources to perform sub-Doppler spectroscopy with high precision [17,18]. By stabilizing the frequency of the source to saturated absorption lines [19], transitions were recorded with uncertainties of 4–40 kHz. One large-scale sub-Doppler survey performed with cavity enhancement [20,21] covered a total of 204 lines with a typical uncertainty of 3 kHz for allowed transitions and 12 kHz for forbidden transitions, which were observed with wavelength modulation. However, many fairly strong transitions in the pentad region are still known to relatively high uncertainty, which we aim to ameliorate. Here, as an extension of the sub-Doppler work on the ν_3 band of methane [19–21], we report 22 methane transitions in the pentad region with uncertainties improved by at least an order of magnitude [4,13,14,22].

2. Experimental

A diagram of the instrument is shown in Fig. 1. 1064 nm light from an ytterbium-doped fiber laser (Koheras Adjustik Y10) is sent to an erbium-doped fiber amplifier (IPG Photonics YAR-10K-1064-LP-SF), which amplifies the light to 8 W. The amplified light is sent to an optical parametric oscillator (OPO; Aculight Argos 2400 SF) to generate idler (400 mW, 3.2–3.9 µm) and signal beams via parametric down-conversion. The idler beam is sent through a 40 cm glass flow cell filled with 75–470 mTorr of $^{12}CH_4$, and is reflected back through the cell. The reflected beam is picked off by a 50/50 Si beamsplitter, modulated by a beam chopper, and focused on a fast mid-infrared photodiode detector (Boston Electronics Vigo, PVM-10.6). The detector output is sent to a lock-in amplifier referenced by the frequency of the chopper. The scans shown here were recorded with a 0.1 MHz step size and a 300 ms time constant.

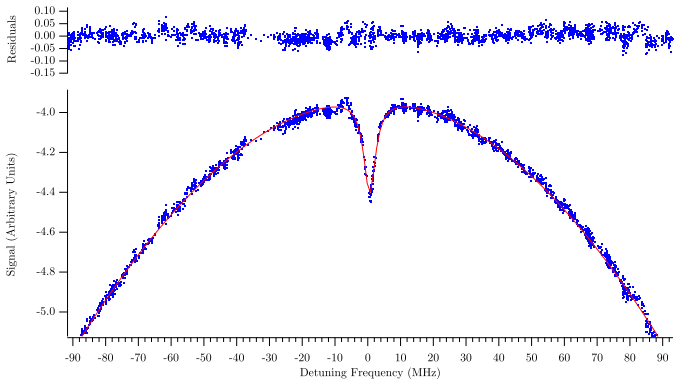

Fig. 2. A representative scan of the F_2 component of the $Q(3)$ transition, centered at 90,488,114 MHz. The dots are the data points, and the curve is the fit. The dots plotted above are the residuals of the fit. The width of the Lamb dip is 4.18 MHz (FWHM).

Frequency calibration of the idler is derived from the difference of the pump and signal frequencies ($\nu_{idler} = \nu_{pump} - \nu_{signal}$), which are calibrated with an optical frequency comb (Menlo Systems FC-1500; 100 MHz repetition rate). An infrared wavemeter (Bristol 621:IR-A) is used for crude frequency calibration and to help determine the number of comb modes between the pump and signal frequencies. The signal beam is locked at an offset of 20 MHz to a single comb tooth via a phase-locked loop, with corrections sent to a piezoelectric transducer (PZT) on the signal cavity within the OPO.

The pump beat is kept within the 25–35 MHz internal bandpass of a frequency counter with a feed-forward mechanism using a freespace acousto-optic modulator (AOM; Brimrose IPF-200-80-1600) in a double-pass configuration using a 70/30 beamsplitter. The idler is stepped by incrementing the voltage sent to the seed laser's PZT by an amount which corresponds to a 0.1 MHz shift in frequency. The AOM then applies a correction to the pump to re-center it within the bandpass of the frequency counter, which is calculated by the acquisition software. The frequency counter reads the beat note frequency, and if it is not in the center of the bandpass, additional AOM corrections are made. Once the beat is centered, a data point is acquired, and the voltage is then stepped again to collect another data point. When the AOM reaches the edge of its diffraction efficiency, the frequency is either increased or decreased accordingly by 50 MHz to create a 100 MHz shift to the next comb tooth. Each point was collected after a 1.5 s delay to allow the frequency counters to update.

3. Results and discussion

A representative scan is shown in Fig. 2, which is the F_2 component of the $Q(3)$ transition of the ν_3 band. Transitions typically had Doppler widths of approximately 400 MHz (full width at half maximum, FWHM) and Lamb dip widths of approximately 4.5 MHz (FWHM). This is attributed to a combination of pressure broadening, power broadening, transit-time broadening, and broadening from the spectral linewidth of the laser. As an example, in the case of the F_2 component of the $Q(3)$ transition, the self-broadening coefficient for the $J'' = 3$ state is estimated to be 0.079 cm^{-1}/atm [23] (half width at half maximum, HWHM), or 6.23 MHz/Torr (FWHM). Pressures of 75–470 mTorr translate to widths of 0.4-2.4 MHz. The Einstein A coefficient for this transition is estimated to be 24.7 Hz [4], giving a transition dipole moment of ~0.054 D. The incident beam had a power of about 200 mW with a beam waist of about 0.32 mm, translating to power broadening of about 1 MHz. Transit-time broadening was estimated to be 0.9 MHz. Broadening from the spectral linewidth of the radia-

Table 1
A comparison between the new measurements and previous measurements of transitions in the ν_3 band of $^{12}CH_4$. Uncertainties are represented by σ, and the difference (new–previous) is represented by δ.

Trans.	Comp.	Meas. Freq. (MHz)	σ (MHz)	Prev. Freq. (MHz)	Prev. σ (MHz)	δ (MHz)
$P(4)$	A_1	89 308 512.47	0.24	89 308 512.256 8[a]	0.002 0	0.21
$P(3)$	A_2	89 601 828.50	0.32	89 601 828.651 4[a]	0.002 5	−0.15
$Q(8)$	$F_2^{(1)}$	90 411 883.95	0.23	90 411 883.753 6[b]	0.003 5	0.20
$Q(8)$	$E^{(2)}$	90 426 451.01	0.14	90 426 450.987 8[b]	0.002 5	0.02
$Q(8)$	$F_2^{(2)}$	90 428 470.18	0.21	90 428 470.084 7[b]	0.003 0	0.09
$Q(3)$	F_1	90 484 623.26	0.16	90 484 623.067 9[a]	0.002 0	0.19
$Q(3)$	F_2	90 488 114.50	0.14	90 488 114.363 3[a]	0.002 0	0.14
$Q(3)$	A_2	90 493 215.45	0.14	90 493 215.526 8[a]	0.002 1	−0.07
$Q(2)$	E	90 495 092.46	0.22	90 495 092.106 1[a]	0.002 3	0.35
$Q(2)$	F_2	90 496 856.61	0.24	90 496 856.544 3[a]	0.002 0	0.07
$Q(1)$	F_1	90 502 080.65	0.33	90 502 080.707 9[a]	0.002 1	−0.05
$R(0)$	A_1	90 799 708.521	0.086	90 799 708.460 6[b]	0.003 5	0.06
$R(5)$	$F_1^{(2)}$	92 232 637.74	0.33	92 232 637.852 8[b]	0.003 5	−0.11
$R(5)$	F_2	92 236 455.46	0.13	92 236 455.591 8[b]	0.003 4	−0.13

[a] Okubo et al. [20].
[b] Abe et al. [21].

Table 2
Measured transition frequencies of the ν_3 band of $^{12}CH_4$. Uncertainties are represented by σ, and the difference (new–previous) is represented by δ.

Trans.	Comp.	Meas. Freq. (MHz)	σ (MHz)	Prev. Freq. (MHz)	Prev. σ (MHz)	δ (MHz)
$P(13)$	A_2	86 492 798.43	0.20	86 492 824[a]	18	−25.3
$P(13)$	A_1	86 512 941.30	0.30	86 512 934[a]	18	7.1
$Q(13)$	$E^{(1)}$	90 264 009.38	0.63	90 264 003[a]	18	6.6
$Q(13)$	$F_1^{(3)}$	90 292 115.52	0.57	90 292 103[a]	18	12.5
$Q(13)$	$E^{(2)}$	90 315 521.4	1.3	90 315 545[a]	30–300[b]	−23.6
$R(9)$	A_2	93 333 228.93	0.46	93 333 232[a]	18	−3.1
$R(9)$	$F_2^{(2)}$	93 333 782.03	0.15	93 333 780[a]	18	2.3
$R(9)$	$F_1^{(3)}$	93 334 428.42	0.74	93 334 421[a]	18	7.6
$R(9)$	A_1	93 336 791.20	0.14	93 336 792[a]	18	−1.3
$R(9)$	$F_1^{(2)}$	93 337 911.61	0.18	93 337 906[a]	18	5.9
$R(9)$	E	93 338 231.72	0.31	93 338 231[a]	18	1.0
$R(9)$	$F_2^{(1)}$	93 346 602.15	0.40	93 346 597[a]	18	5.1
$R(9)$	$F_1^{(1)}$	93 346 738.59	0.60	93 346 735[a]	18	3.3
$R(10)$	$F_2^{(3)}$	93 602 932.75	0.54	93 602 925[c]	3–30[d]	7.7
$R(10)$	$E^{(2)}$	93 603 751.27	0.46	93 603 759[e]	3	−7.6
$R(10)$	$F_1^{(2)}$	93 604 085.42	0.15	93 604 085[a]	18	0.2
$R(10)$	A_1	93 605 158.06	0.25	93 605 147[a]	18	11.4
$R(10)$	$F_1^{(1)}$	93 608 383.63	0.37	93 608 375[f]	17	9.0
$R(10)$	$F_2^{(2)}$	93 608 521.59	0.44	93 608 516[f]	17	6.0
$R(10)$	A_2	93 618 091.33	0.12	93 618 065[a]	18	26.2
$R(10)$	$F_2^{(1)}$	93 618 121.80	0.19	93 618 105[a]	18	16.6
$R(10)$	$E^{(1)}$	93 618 132.90	0.34	93 618 131[e]	3	1.7

[a] Daumont et al. [14].
[b] Uncertainty index 3 from the HITRAN2016 database [4].
[c] Gordon et al. [4].
[d] Uncertainty index 4 from the HITRAN2016 database [4].
[e] Albert et al. [13].
[f] Tyuterev et al. [22].

tion from the laser was estimated to be 0.5 MHz by observing the widths of the beats generated by the pump and signal beams with the modes of the frequency comb.

In order to verify the efficacy of the spectrometer and the accuracy of the calibration, we measured 14 transitions which had already been measured to kHz-level uncertainty. Table 1 shows the comparison of the 14 measured lines between our values and the literature values [20,21]. Lines were measured at least five times, using the arithmetic mean of the values as the center and the sample standard deviation of the set of transition frequencies as the uncertainty. In each case, our measured value agrees with the literature value within twice our standard deviation, with the majority within one standard deviation, lending reliability to the method.

Table 2 lists the 22 measured transition frequencies with their uncertainties in MHz, the previously measured frequencies as listed in the HITRAN2016 database [4,13,14,22], and the differences between the two. Lines were measured at least seven times on at least two separate days. The data have an average uncertainty of 0.40 MHz, ranging from 0.12 MHz to 1.3 MHz, with higher uncertainties generally accompanying weaker transitions. All newly measured frequencies agree with past measurements within 2σ with the exception of the $E^{(2)}$ component of the $R(10)$ transition as reported by Albert et al. [13], which was a Doppler-broadened experiment. Other transitions from this work have been remeasured in a sub-Doppler survey by Abe et al. [21], where disagreements were well outside of the reported Doppler-broadened uncertainty of $\sim$3 MHz for transitions within the pentad region.

Scans were fit by modeling the Lamb dip as a Lorentzian lineshape and the Doppler profile as a Gaussian lineshape. In the instances of multiple overlapping Doppler profiles, fitting functions were adjusted accordingly to the number of transitions which were measured. For example, the A_2, $F_2^{(1)}$, and $E^{(1)}$ components of the

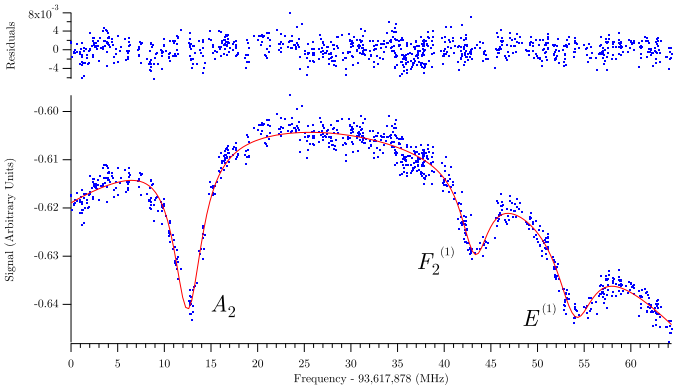

Fig. 3. A scan of the A_2, $F_2^{(1)}$, and $E^{(1)}$ components of the $R(10)$ transition, relative to 93,617,878 MHz. The dots are the data, the curve is the fit, and the dots plotted above show the residuals.

$R(10)$ transition shown in Fig. 3 were fit simultaneously as a sum of three Lorentzian profiles with three accompanying Gaussian profiles.

4. Conclusion

We have measured 22 transitions in the pentad region of methane. All transitions were measured to MHz-level uncertainty by taking advantage of the narrow sub-Doppler features resulting from saturated absorption. These values improve the precision of known transition frequencies by at least an order of magnitude. This work can be used for more precise modeling of methane as a benchmark for new *ab initio* calculations.

Funding

P.A.K. is grateful for funding from the University of Illinois at Urbana-Champaign Campus Honors Program Summer Research Grant, and for financial support from a Peter C. & Gretchen Miller Markunas Scholarship and a Matthews Scholarship. C.R.M. is grateful for support from a National Aeronautics and Space Administration (NASA) Earth and Space Science Fellowship (NESSF NNX16AO86H). This work was also funded by a grant from the National Science Foundation (NSF PHY 14-04330).

Conflicts of interest

None.

References

[1] Pauling L. The nature of the chemical bond. Application of results obtained from the quantum mechanics and from a theory of paramagnetic susceptibility to the structure of molecules. J Am Chem Soc 1931;53(4):1367–400. doi:10.1021/ja01355a027.

[2] Nikitin AV, Rey M, Tyuterev VG. Accurate line intensities of methane from first-principles calculations. J Quant Spectrosc Radiat Transf 2017;200:90–9. doi:10.1016/j.jqsrt.2017.05.023.

[3] Nikitin AV, Rey M, Tyuterev VG. First fully *ab initio* potential energy surface of methane with a spectroscopic accuracy. J Chem Phys 2016;145:114309. doi:10.1063/1.4961973.

[4] Gordon IE, Rothman LS, Hill C, Kochanov RV, Tan Y, Bernath PF, et al. The HITRAN2016 molecular spectroscopic database. J Quant Spectrosc Radiat Transf 2017;203:3–69. doi:10.1016/j.jqsrt.2017.06.038.

[5] Tennyson J, Yurchenko SN, Al-Refaie AF, Barton EJ, Chubb KL, Coles PA, et al. The ExoMol database: molecular line lists for exoplanet and other hot atmospheres. J Mol Spectrosc 2016;327:73–94. doi:10.1016/j.jms.2016.05.002.

[6] Owen T, Cess RD. Methane absorption in the visible spectra of the outer planets and Titan. Astrophys J 1975;197:L37–40. doi:10.1086/181771.

[7] Swain MR, Vasisht G, Tinetti G. The presence of methane in the atmosphere of an extrasolar planet. Nature 2008;452:329–31. doi:10.1038/nature06823.

[8] Oppenheimer BR, Kulkarni SR, Matthews K, van Kerkwijk MH. The spectrum of the brown dwarf Gliese 229B. Astrophys J 1998;502(2):932–43. doi:10.1086/305928.

[9] Khalil MAK. Non-CO_2 greenhouse gases in the atmosphere. Annu Rev Energy Environ 1999;24(1):645–61. doi:10.1146/annurev.energy.24.1.645.

[10] Boucher O, Friedlingstein P, Collins B, Shine KP. The indirect global warming potential and global temperature change potential due to methane oxidation. Environ Res Lett 2009;4(4):044007. doi:10.1088/1748-9326/4/4/044007.

[11] Gray DL, Robiette AG. The anharmonic force field and equilibrium structure of methane. Mol Phys 1979;37(6):1901–20. doi:10.1080/00268977900101401.

[12] Hilico JC, Champion JP, Toumi S, Tyuterev VG, Tashkun SA. New analysis of the pentad system of methane and prediction of the (pentad-pentad) spectrum. J Mol Spectrosc 1994;168(2):455–76. doi:10.1006/jmsp.1994.1293.

[13] Albert S, Bauerecker S, Boudon V, Brown LR, Champion J-P, Loëte M, et al. Global analysis of the high resolution infrared spectrum of methane $^{12}CH_4$ in the region from 0 to 4800 cm^{-1}. Chem Phys 2009;356(1–3):131–46. doi:10.1016/j.chemphys.2008.10.019.

[14] Daumont L, Nikitin AV, Thomas X, Régalia L, Von der Heyden P, Tyuterev VG, et al. New assignments in the 2 µm transparency window of the $^{12}CH_4$ octad band system. J Quant Spectrosc Radiat Transf 2013;116:101–9. doi:10.1016/j.jqsrt.2012.08.025.

[15] Féjard L, Champion JP, Jouvard JM, Brown LR, Pine AS. The intensities of methane in the 3–5 µm region revisited. J Mol Spectrosc 2000;201:83–94. doi:10.1006/jmsp.2000.8065.

[16] Baumann E, Giorgetta FR, Swann WC, Zolot AM, Coddington I, Newbury NR. Spectroscopy of the methane ν_3 band with an accurate midinfrared coherent dual-comb spectrometer. Phys Rev A 2011;84(6):062513. doi:10.1103/PhysRevA.84.062513.

[17] Maddaloni P, Gagliardi G, Malara P, De Natale P. A 3.5-mW continuous-wave difference-frequency source around 3 µm for sub-Doppler molecular spectroscopy. Appl Phys B 2005;80(2):141–5. doi:10.1007/s00340-004-1714-0.

[18] Anzai K, Gao X, Sasada H, Yoshida N. Narrow lamb dip of 3.4 µm band transition of methane with difference frequency generation and enhancement cavity. Jpn J Appl Phys 2006;45(4A):2771–5. doi:10.1143/JJAP.45.2771.

[19] Takahata K, Kobayashi T, Sasada H, Nakajima Y, Inaba H, Hong F-L. Absolute frequency measurement of sub-Doppler molecular lines using a 3.4-µm difference-frequency-generation spectrometer and a fiber-based frequency comb. Phys Rev A 2009;80:032518. doi:10.1103/PhysRevA.80.032518.

[20] Okubo S, Nakayama H, Iwakuni K, Inaba H, Sasada H. Absolute frequency list of the ν_3-band transitions of methane at a relative uncertainty level of 10^{-11}. Opt Express 2011;19(24):23878–88. doi:10.1364/OE.19.023878.

[21] Abe M, Iwakuni K, Okubo S, Sasada H. Accurate transition frequency list of the ν_3 band of methane from sub-Doppler resolution comb-referenced spectroscopy. J Opt Soc Am B 2013;30(4):1027–35. doi:10.1364/JOSAB.30.001027.

[22] Tyuterev V, Tashkun S, Rey M, Kochanov R, Nikitin A, Delahaye T. Accurate spectroscopic models for methane polyads derived from a potential energy surface using high-order contact transformations. J Phys Chem A 2013;117(50):13779–805. doi:10.1021/jp408116j.

[23] Brown LR, Sung K, Benner DC, Devi VM, Boudon V, Gabard T, et al. Methane line parameters in the HITRAN2012 database. J Quant Spectrosc Radiat Transf 2013;130:201–19. doi:10.1016/j.jqsrt.2013.06.020.

References

[1] T. P. Snow and V. M. Bierbaum, *Annual review of analytical chemistry (Palo Alto, Calif.)*, 1, 229–259 (2008).

[2] M. Larsson, W. D. Geppert, and G. Nyman, *Reports on Progress in Physics*, 75, 066901 (2012).

[3] V. G. Anicich and J. Huntress, W. T., *The Astrophysical Journal Supplement Series*, 62, 553 (1986).

[4] B. Eliasson and U. Kogelschatz, *IEEE Transactions on Plasma Science*, 19, 1063–1077 (1991).

[5] J. Tennyson, O. L. Polyansky, N. F. Zobov, *et al.*, *Journal of Physics B: Atomic, Molecular and Optical Physics*, 50, 232001 (2017).

[6] W. B. Cairncross, D. N. Gresh, M. Grau, *et al.*, *Physical Review Letters*, 119, 153001 (2017).

[7] T. Dunham, *Publications of the Astronmical Society of the Pacific*, 49, 26–28 (1937).

[8] A. Mckellar, *Publications of the Astronmical Society of the Pacific*, 52, 187–192 (1940).

[9] W. S. Adams, *The Astrophysical Journal*, 93, 11 (1941).

[10] A. E. Douglas and G. Herzberg, *The Astrophysical Journal*, page 381 (1941).

[11] S. Weinreb, A. H. Barrett, M. L. Meeks, *et al.*, *Nature*, 200, 829–831 (1963).

[12] B. A. Mcguire, *The Astrophysical Journal Supplement Series*, 239, 17 (2018).

[13] D. M. Rank, C. H. Townes, and W. J. WELCH, *Science*, 174, 1083–1101 (1971).

[14] W. D. Watson, *The Astrophysical Journal*, 183, L17 (1973).

[15] E. Herbst, W. Klemperer, W. K. Eric Herbst, *et al.*, *The Astrophysical Journal*, 185, 505–533 (1973).

[16] D. O. Schissler and D. P. Stevenson, *Journal of Chemical Physics*, 24, 926–926 (1956).

[17] B. J. McCall, T. R. Geballe, K. H. Hinkle, *et al.*, *The Astrophysical Journal*, 522, 338 (1999).

[18] D. Hollenbach, M. J. Kaufman, D. Neufeld, *et al.*, *The Astrophysical Journal*, 754, 105 (2012).

[19] N. Indriolo, B. D. Fields, and B. J. Mccall, *The Astrophysical Journal*, pages 257–267 (2009).

[20] N. Indriolo, D. A. Neufeld, M. Gerin, *et al.*, *The Astrophysical Journal*, 758, 83 (2012).

[21] B. Tercero, J. Cernicharo, J. R. Pardo, *et al.*, *Astronomy & Astrophysics*, 517, 96 (2010).

[22] E. Herbst and E. F. van Dishoeck, *Annual Review of Astronomy & Astrophysics*, 47, 427–480 (2009).

[23] M. Born and R. Oppenheimer, *Annalen der Physik*, 389, 457–484 (1927).

[24] A. G. Császár, C. Fábri, T. Szidarovszky, *et al.*, *Physical Chemistry Chemical Physics*, 14, 1085–1106 (2012).

[25] J. Tennyson, *Journal of Chemical Physics*, 145, 120901 (2016).

[26] E. F. Valeev and C. D. Sherrill, *Journal of Chemical Physics*, 118, 3921 (2003).

[27] G. A. Worth and L. S. Cederbaum, *Annual Review of Physical Chemistry*, 55, 127–158 (2004).

[28] J. Bloino, A. Baiardi, and M. Biczysko, *International Journal of Quantum Chemistry*, pages 1543–1574 (2016).

[29] L. G. Diniz, J. R. Mohallem, A. Alijah, *et al.*, *Physical Review A*, 88, 032506 (2013).

[30] W. Caswell and G. Lepage, *Physics Letters B*, 167, 437–442 (1986).

[31] M. Stanke, D. Kędziera, S. Bubin, *et al.*, *Physical Review A*, 77, 022506 (2008).

[32] J. Komasa, K. Piszczatowski, G. Łach, *et al.*, *Journal of Chemical Theory and Computation*, 7, 3105–3115 (2011).

[33] V. I. Korobov, *Physical Review A*, 77, 022509 (2008).

[34] E. J. Salumbides, D. Bailly, A. Khramov, *et al.*, *Physical Review Letters*, 101, 223001 (2008).

[35] M. Pavanello, L. Adamowicz, A. Alijah, *et al.*, *Journal of Chemical Physics*, 136, 184303 (2012).

[36] T. Furtenbacher and A. G. Császár, *Journal of Quantitative Spectroscopy and Radiative Transfer*, 113, 929–935 (2012).

[37] C. S. Gudeman, M. H. Begemann, J. Pfaff, *et al.*, *Journal of Chemical Physics*, 78, 5837 (1983).

[38] B. M. Siller, A. A. Mills, and B. J. Mccall, *Optics letters*, 35, 1266–1268 (2010).

[39] K. N. Crabtree, J. N. Hodges, B. M. Siller, *et al.*, *Chemical Physics Letters*, 551, 1–6 (2012).

[40] R. W. P. Drever, J. L. Hall, F. V. Kowalski, *et al.*, *Applied Physics B*, 31, 97–105 (1983).

[41] J. Ye, L.-S. Ma, and J. L. Hall, *Journal of the Optical Society of America B*, 15, 6 (1998).

[42] J. N. Hodges, A. J. Perry, P. A. Jenkins II, *et al.*, *Journal of Chemical physics*, 139, 164201 (2013).

[43] A. J. Perry, J. N. Hodges, C. R. Markus, *et al.*, *Journal of Molecular Spectroscopy*, 317, 71–73 (2015).

[44] A. J. Perry, J. N. Hodges, C. R. Markus, *et al.*, *Journal of Chemical Physics*, 101101, 101101 (2014).

[45] C. R. Markus, J. N. Hodges, A. J. Perry, *et al.*, *The Astrophysical Journal*, 817, 138 (2016).

[46] J. L. Hall, *Reviews of Modern Physics*, 78, 1279–1295 (2006).

[47] O. Asvany, S. Brünken, L. Kluge, *et al.*, *Applied Physics B*, 114, 203–211 (2014).

[48] L. Lodi, O. L. Polyansky, J. Tennyson, *et al.*, *Physical Review A*, 89, 032505 (2014).

[49] H.-C. Chen, C.-Y. Hsiao, J.-L. Peng, *et al.*, *Physical Review Letters*, 109, 263002 (2012).

[50] O. Asvany, J. J. Krieg, and S. Schlemmer, *Review of Scientific Instruments*, 83, 093110 (2012).

[51] C. Langrock, E. Diamanti, R. V. Roussev, *et al.*, *Optics Letters*, 30, 1725 (2005).

[52] M. J. Khan, J. C. Chen, and S. Kaushik, *Optics Letters*, 32, 3248–3250 (2007).

[53] K. Karstad, A. Stefanov, M. Wegmuller, *et al.*, *Optics and Lasers in Engineering*, 43, 537–544 (2005).

[54] P. Ehlers, A. C. Johansson, I. Silander, *et al.*, *Journal of the Optical Society of America B*, 31, 2938 (2014).

[55] E. A. Whittaker, M. Gehrtz, and G. C. Bjorklund, *Journal of the Optical Society of America B*, 2, 1320 (1985).

[56] C. R. Webster, *Journal of the Optical Society of America B*, 2, 1464 (1985).

[57] O. Axner, W. Ma, and A. Foltynowicz, *Journal of the Optical Society of America B*, 25, 1166–1177 (2008).

[58] R. W. Boyd and G. L. Fischer, Nonlinear Optical Materials (2001).

[59] A. V. Smith, SNLO Nonlinear optics code, http:/www.as-photonics.com/SNLO (2010).

[60] P. Werle, R. Mücke, and F. Slemr, *Applied Physics B Photophysics and Laser Chemistry*, 57, 131–139 (1993).

[61] R. G. DeVoe and R. G. Brewer, *Physical Review A*, 30, 2827–2829 (1984).

[62] E. F. van Dishoeck and J. H. Black, *The Astrophysical Journal Supplement Series*, 62, 109 (1986).

[63] N. Indriolo, D. A. Neufeld, M. Gerin, *et al.*, *The Astrophysical Journal*, 800, 40 (2015).

[64] A. Wootten, B. E. Turner, J. G. Mangum, *et al.*, *The Astrophysical Journal*, 380, L79 (1991).

[65] V. Ossenkopf, H. S. P. Müller, D. C. Lis, *et al.*, *Astronomy & Astrophysics*, 518, L111 (2010).

[66] F. Wyrowski, K. M. Menten, R. Güsten, *et al.*, *Astronomy & Astrophysics*, 518, A26 (2010).

[67] F. V. D. Tak, Z. Nagy, and V. Ossenkopf, *Astronomy & Astrophysics*, 95, 1–10 (2013).

[68] I. Aleman, T. Ueta, D. Ladjal, *et al.*, *Astronomy & Astrophysics*, 566, A79 (2014).

[69] M. Etxaluze, J. Cernicharo, J. R. Goicoechea, *et al.*, *Astronomy & Astrophysics*, 78, 1–10 (2014).

[70] E. González-Alfonso, J. Fischer, S. Bruderer, *et al.*, *Astronomy & Astrophysics*, 550, A25 (2013).

[71] J. P. Bekooy, P. Verhoeve, W. L. Meerts, *et al.*, *Journal of Chemical Physics*, 82, 3868 (1985).

[72] D.-J. Liu, W.-C. Ho, and T. Oka, *Journal of Chemical Physics*, 87, 2442 (1987).

[73] M. H. W. Gruebele, R. P. Müller, and R. J. Saykally, *Journal of Chemical Physics*, 84, 2489 (1986).

[74] S. Brünken, H. S. Müller, F. Lewen, *et al.*, *Journal of Chemical Physics*, 123 (2005).

[75] H. S. P. Müller, F. Schlöder, J. Stutzki, *et al.*, *Journal of Molecular Structure*, 742, 215–227 (2005).

[76] B. D. Rehfuss, M.-F. Jagod, L.-W. Xu, *et al.*, Infrared spectroscopy of highly excited vibrational levels of the hydroxyl ion, OH+ (1992).

[77] S. Heyminck, U. U. Graf, R. Güsten, *et al.*, *Astronomy & Astrophysics*, 542, L1 (2012).

[78] B. M. Siller, M. W. Porambo, A. A. Mills, *et al.*, *Optics express*, 19, 24822–7 (2011).

[79] L. S. Rothman, I. E. Gordon, Y. Babikov, *et al.*, *Journal of Quantitative Spectroscopy and Radiative Transfer*, 130, 4–50 (2013).

[80] H. M. Pickett, *Journal of Molecular Spectroscopy*, 148, 371–377 (1991).

[81] H. S. P. Müller, J. R. Goicoechea, J. Cernicharo, *et al.*, *Astronomy & Astrophysics*, 569, L5 (2014).

[82] J. L. Linsky, B. T. Draine, H. W. Moos, *et al.*, *The Astrophysical Journal*, 647, 1106–1124 (2006).

[83] H. Roberts, E. Herbst, and T. J. Millar, *Astronomy & Astrophysics*, 424, 905–917 (2004).

[84] C. Vastel, T. G. Phillips, and H. Yoshida, *The Astrophysical Journal*, 606, L127–L130 (2004).

[85] J. Harju, O. Sipilä, S. Brünken, *et al.*, *The Astrophysical Journal*, 840, 63– (2017).

[86] P. Jusko, A. Stoffels, S. Thorwirth, *et al.*, in *J. Mol. Spectrosc.* [141], pages 59 – 66.

[87] S. Yu, J. C. Pearson, T. Amano, *et al.*, *Journal of Molecular Spectroscopy*, 331, 6–8 (2017).

[88] O. L. Polyansky and A. R. W. McKellar, *Journal of Chemical Physics*, 92, 4039 (1990).

[89] D. Jennings, C. Demuynck, M. Banek, and K. Evenson, personal communications, cited by Polyansky & Mckellar (2001).

[90] P. Jusko, C. Konietzko, S. Schlemmer, *et al.*, *Journal of Molecular Spectroscopy*, 319, 55–58 (2016).

[91] K. G. Lubic and T. Amano, *Canadian Journal of Physics*, 62, 1886–1888 (1984).

[92] S. C. Foster, A. R. W. McKellar, and J. K. G. Watson, *Journal of Chemical Physics*, 85, 664 (1986).

[93] H. M. Pickett, J. C. Pearson, and C. E. Miller, *Journal of Molecular Spectroscopy*, 233, 174–179 (2005).

[94] A. Foltynowicz, I. Silander, and O. Axner, *Journal of the Optical Society of America B*, 28, 2797 (2011).

[95] B. J. McCall, *Spectroscopy of H_3^+ Laboratory and Astrophysical Plasmas*, Ph.D. thesis, University of Chicago (2001).

[96] P. A. Kocheril, C. R. Markus, A. M. Esposito, *et al.*, *Journal of Quantitative Spectroscopy and Radiative Transfer*, 215, 9–12 (2018).

[97] S. Brünken, H. S. P. Müller, C. Endres, *et al.*, *Phys. Chem. Chem. Phys.*, 9, 2103–2112 (2007).

[98] S. Brünken, H. S. P. Müller, F. Lewen, *et al.*, *Journal of Chemical Physics*, 123 (2005).

[99] T. Hirao and T. Amano, *The Astronomical Journal*, 597, L85 (2003).

[100] C. R. Markus, P. A. Kocheril, and B. J. McCall, *Journal of Molecular Spectroscopy*, 355, 8–13 (2019).

[101] N. Indriolo, T. R. Geballe, T. Oka, *et al.*, *The Astrophysical Journal*, 671, 1736–1747 (2007).

[102] P. Drossart, J.-P. Maillard, J. Caldwell, *et al.*, *Nature*, 340, 539–541 (1989).

[103] Y.-c. Guan, Y.-h. Chang, Y.-c. Liao, *et al.*, *Journal of Chemical Physics*, 148, 124310 (2018).

[104] J. T. Hougen, *Journal of Chemical Physics*, 37, 1433–1441 (1962).

[105] C. Lindsay and B. J. McCall, *Journal of Molecular Spectroscopy*, 210, 60–83 (2001).

[106] C. R. Markus, A. J. Perry, J. N. Hodges, *et al.*, *Optics Express*, 25, 3709 (2017).

[107] A. J. Perry, C. R. Markus, J. N. Hodges, *et al.*, in *The 71st International Symposium on Molecular Spectroscopy, Urbana, IL* (2016).

[108] C. R. Markus, P. A. Kocheril, A. M. Esposito, *et al.*, in *The 73rd International Symposium on Molecular Spectroscopy, Urbana, IL* (2018).

[109] A. R. W. McKellar and J. Watson, *Journal of Molecular Spectroscopy*, 191, 215–217 (1998).

[110] W. A. Majewski, M. D. Marshall, A. R. W. McKellar, *et al.*, *Journal of Molecular Spectroscopy*, 122, 341–355 (1987).

[111] M. G. Bawendi, B. D. Rehfuss, and T. Oka, *Journal of Chemical Physics*, 93, 6200 (1990).

[112] J. K. G. Watson, S. C. Foster, A. R. W. McKellar, *et al.*, *Canadian Journal of Physics*, 62, 1875–1885 (1984).

[113] D. Uy, C. M. Gabrys, M. F. Jagod, *et al.*, *Journal of Chemical Physics*, 100, 6267–6274 (1994).

[114] W. H. Flygare, *Accounts of Chemical Research*, 1, 121–127 (1968).

[115] B. M. Dinelli, S. Miller, and J. Tennyson, *Journal of Molecular Spectroscopy*, 153, 718–725 (1992).

[116] L.-W. Xu, C. Gabrys, and T. Oka, *Journal of Chemical Physics*, 93, 6210 (1990).

[117] F.-S. Pan and T. Oka, *The Astrophysical Journal*, 305, 518 (1986).

[118] J. H. Black, *Faraday Discussions*, 109, 257–266 (1998).

[119] I. I. Mizus, A. Alijah, N. F. Zobov, *et al.*, *Monthly Notices of the Royal Astronomical Society*, 468, 1717–1725 (2017).

[120] R. E. Moss, *Molecular Physics*, 89, 195–210 (1996).

[121] E. Mátyus, T. Szidarovszky, and A. G. Császár, *Journal of Chemical Physics*, 141 (2014).

[122] P. D. Godfrey, R. D. Brown, B. J. Robinson, *et al.*, *The Astrophysical Letters*, 13, 119–121 (1973).

[123] J. E. Dickens, W. M. Irvine, C. H. DeVries, *et al.*, *The Astrophysical Journal*, 479, 307–312 (1997).

[124] E. G. Bøgelund, B. A. McGuire, M. R. Hogerheijde, *et al.*, *Astronomy & Astrophysics*, 624, A82 (2019).

[125] C. J. Salter, T. Ghosh, B. Catinella, *et al.*, *The Astronomical Journal*, 136, 389–399 (2008).

[126] T. Suzuki, M. Ohishi, T. Hirota, *et al.*, *The Astrophysical Journal*, 825, 1–14 (2016).

[127] N. F. W. Ligterink, H. Calcutt, A. Coutens, *et al.*, *Astronomy & Astrophysics*, 619, A28 (2018).

[128] P. Theule, F. Borget, F. Mispelaer, *et al.*, *Astronomy & Astrophysics*, 534, A64 (2011).

[129] G. de Oliveira, J. M. L. Martin, I. K. C. Silwal, *et al.*, *Journal of Computational Chemistry*, 22, 1297–1305 (2001).

[130] V. Vuitton, R. V. Yelle, and V. Anicich, *The Astrophysical Journal*, 647, L175–L178 (2006).

[131] R. V. Yelle, V. Vuitton, P. Lavvas, *et al.*, *Faraday Discussions*, 147, 31–49 (2010).

[132] D. Skouteris, N. Balucani, N. Faginas-Lago, *et al.*, *Astronomy & Astrophysics*, 584, A76 (2015).

[133] J. P. Wagner, S. M. Giles, and M. A. Duncan, *Chemical Physics Letters*, 726, 53 – 56 (2019).

[134] R. Thackston and R. C. Fortenberry, *Icarus*, 299, 187 – 193 (2018).

[135] O. Asvany, F. Bielau, D. Moratschke, *et al.*, *Review of Scientific Instruments*, 81, 076102 (2010).

[136] O. Asvany, S. Brünken, L. Kluge, *et al.*, *Applied Physics B*, 114, 203–211 (2014).

[137] P. Jusko, O. Asvany, A.-C. Wallerstein, *et al.*, *Physical Review Letters*, 112, 253005 (2014).

[138] S. Chakrabarty, M. Holz, E. K. Campbell, *et al.*, *Journal of Physical Chemistry Letters*, 4, 4051–4054 (2013).

[139] O. Asvany, K. M. T. Yamada, S. Brünken, *et al.*, *Science*, 347, 1346–1349 (2015).

[140] P. Jusko, C. Konietzko, S. Schlemmer, *et al.*, *Journal of Molecular Spectroscopy*, 319, 55–58 (2016).

[141] P. Jusko, A. Stoffels, S. Thorwirth, *et al.*, *J. Mol. Spectrosc.*, 332, 59 – 66 (2017).

[142] H. Kohguchi, P. Jusko, K. M. T. Yamada, *et al.*, *Journal of Chemical Physics*, 148, 144303 (2018).

[143] J. L. Doménech, P. Jusko, S. Schlemmer, *et al.*, *The Astrophysical Journal*, 857, 61 (2018).

[144] S. Brünken, L. Kluge, A. Stoffels, *et al.*, *Journal of Molecular Spectroscopy*, 332, 67–78 (2017).

[145] S. Brünken, L. Kluge, A. Stoffels, *et al.*, *The Astrophysical Journal Letters*, 783, L4 (2014).

[146] A. Stoffels, L. Kluge, S. Schlemmer, *et al.*, *Astronomy & Astrophysics*, 593, A56 (2016).

[147] J. L. Doménech, S. Schlemmer, and O. Asvany, *The Astrophysical Journal*, 849, 60 (2017).

[148] J. L. Doménech, S. Schlemmer, and O. Asvany, *The Astrophysical Journal*, 866, 158 (2018).

[149] T. Salomon, M. Töpfer, P. Schreier, *et al.*, *Physical Chemistry Chemical Physics*, 21, 3440–3445 (2019).

[150] S. Thorwirth, P. Schreier, T. Salomon, *et al.*, *The Astrophysical Journal*, 882, L6 (2019).

[151] K. Raghavachari, G. W. Trucks, J. A. Pople, *et al.*, *Chemical Physics Letters*, 157, 479–483 (1989).

[152] K. A. Peterson and T. H. Dunning, *Journal of Chemical Physics*, 117, 10548–10560 (2002).

[153] R. A. Kendall, T. H. Dunning, and R. J. Harrison, *Journal of Chemical Physics*, 96, 6796–6806 (1992).

[154] S. Coriani, D. Marcheson, J. Gauss, *et al.*, *Journal of Chemical Physics*, 123, 184107 (2005).

[155] S. Thorwirth and M. E. Harding, *Journal of Chemical Physics*, 130, 214303 (2009).

[156] S. Thorwirth, M. E. Harding, J. B. Dudek, *et al.*, *Journal of Molecular Spectroscopy*, 350, 10–17 (2018).

[157] CFOUR, a quantum chemical program package written by J. F. Stanton, J. Gauss, M. E. Harding, P. G. Szalay with contributions from A. A. Auer, R. J. Bartlett, U. Benedikt, C. Berger, D. E. Bernholdt, Y. J. Bomble, L. Cheng, O. Christiansen, M. Heckert, O. Heun, C. Huber, T.-C. Jagau, D. Jonsson, J. Jusélius, K. Klein, W. J. Lauderdale, D. A. Matthews, T. Metzroth, L. A. Mück, D. P. O'Neill, D. R. Price, E. Prochnow, C. Puzzarini, K. Ruud, F. Schiffmann, W. Schwalbach, S. Stopkowicz, A. Tajti, J. Vázquez, F. Wang, J. D. Watts and the integral packages MOLECULE (J. Almlöf and P. R. Taylor), PROPS (P. R. Taylor), ABACUS (T. Helgaker, H. J. Aa. Jensen, P. Jørgensen, and J. Olsen), and ECP routines by A. V. Mitin and C. van Wüllen. For the current version, see http://www.cfour.de.

[158] M. E. Harding, T. Metzroth, J. Gauss, *et al.*, *Journal of Chemical Theory and Computation*, 4, 64–74 (2008).

[159] J. D. Watts, J. Gauss, and R. J. Bartlett, *Chemical Physics Letters*, 200, 1–7 (1992).

[160] J. Gauss and J. F. Stanton, *Chemical Physics Letters*, 276, 70–77 (1997).

[161] J. F. Stanton and J. Gauss, *International Reviews in Physical Chemistry*, 19, 61–95 (2000).

[162] J. F. Stanton, C. L. Lopreore, and J. Gauss, *Journal of Chemical Physics*, 108, 7190–7196 (1998).

[163] C. Puzzarini, J. F. Stanton, and J. Gauss, *International Reviews in Physical Chemistry*, 29, 273–367 (2010).

[164] O. Asvany and S. Schlemmer, *International Journaly of Mass Spectrometry*, 279, 147–155 (2009).

[165] C. M. Western, *Journal of Quantitative Spectroscopy and Radiative Transfer*, 186, 221 – 242 (2017).

[166] W. Gordy and R. L. Cook, *Microwave Molecular Spectra*, Wiley, New York, 3 edition (1984).

[167] D. Oepts, A. van der Meer, and P. van Amersfoort, *Infrared Physics & Technology*, 36, 297–308 (1995).

[168] P. Jusko, S. Brünken, O. Asvany, *et al.*, *Faraday Discussions*, 217, 172–202 (2019).